**TRW**
SYSTEMS GROUP

---

ANALYSIS OF FOLDING STRAINS ON
COMPOSITE BLADDER STRUCTURES

---

Contract NAS 7-682                    1 April 1970

CASE FILE
COPY

Prepared for
NASA WESTERN OPERATIONS OFFICE
Pasadena, California

VOLUME I - TECHNICAL

TRW SYSTEMS GROUP
One Space Park
Redondo Beach, California

FINAL REPORT

Contract No. NAS 7-682

ANALYSIS OF FOLDING STRAINS ON COMPOSITE BLADDER STRUCTURES
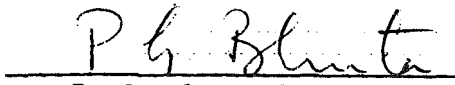
1 April 1970

Prepared for:

NATIONAL AERONAUTICS AND SPACE ADMINISTRATION

Pasadena, California

Prepared by:

L. D. Hofmeister
Project Manager

Approved by:

P. G. Bhuta, Manager
Applied Mechanics Laboratory

TRW SYSTEMS GROUP
One Space Park
Redondo Beach, California

FOREWORD

This is the final report on Contract NAS 7-682, and it covers the work performed from July 1, 1968 to March 31, 1970. The research reported herein was supported by the NASA Pasadena Office. Mr. R. S. Weiner of the Jet Propulsion Laboratory, Pasadena, California, is the Technical Manager of the program.

This study was conducted by the Advanced Technology Department, Applied Mechanics Laboratory of TRW Systems Group. The TRW Project Manager was Dr. G. A. Greenbaum for the period of July 1, 1968 to January 31, 1970, with Dr. L. D. Hofmeister assuming this role from February 1, 1970 to March 31, 1970. Contributions to this program were also made by the following personnel: Dr. G. C. K. Yeh, Dr. D. A. Evensen, Mr. P. J. Hendricks, Mr. P. J. O'Neill and Mr. J. R. Taylor.

The author wishes to acknowledge the helpful suggestions of Mr. R. S. Weiner and Mr. R. Simpson of the Jet Propulsion Laboratory.

ABSTRACT

A detailed study was conducted in order to develop rational methods
to predict structural fatigue life of laminated expulsion bladders. The
technical approach was to first compute plastic strains in typical single
and double folds of bladder materials, and then relate these strains to
experimental fatigue data in order to predict cyclic operating life of
the bladder. A computer program, based upon the "finite element" method
of continuum mechanics, was written for calculating the folding strains.
The single fold was simulated by a plane strain model, whereas the
double fold required an axisymmetric model. The program includes many
features which should facilitate its use by a bladder design engineer,
and output includes the prediction of fatigue life as well as a detailed
printout of strains and stresses in the bladder model. The theory on
which the computer program is based differs from others which also attack
highly nonlinear static structural response in that the present theory
allows a check on solution accuracy. This theory represents a significant
contribution to the state-of-the-art in solid mechanics.

CONTENTS

Illustrations

**TRW**
SYSTEMS GROUP

Illustrations (Continued)

Tables

# I. INTRODUCTION AND BACKGROUND

The supply of liquid propellants to the rocket engine is one problem that arises in spacecraft design. The propellants must be supplied in controlled amounts, and they must be free from gas or vapor bubbles, since bubbles can lead to rough burning or failure of the engine. One method of supplying vapor-free propellants in a zero-gravity environment is to use some form of a positive expulsion device. Although various expulsion devices have been proposed, the most successful approach to date has been to employ a flexible bladder in each propellant tank. By supplying gas pressure to the exterior of the bladder, the liquid propellant is forced out of its container and delivered to the engine.

The expulsion bladders must function properly for a successful firing of the engine. However, when the propellant is expelled, the bladder develops folds, creases, and wrinkles that can crack or tear the material and thereby result in a mechanical failure of the bladder. In most cases, a bladder does not fail the first time it is employed, but, the bladder is subjected to several expulsion cycles (during ground operations and check-out of the spacecraft), and it is then required to perform in flight. Thus a major problem in the design of bladders is to avoid low cycle fatigue failure of the bladder material.

One solution to this fatigue problem is to make the bladder out of a material such as rubber, which can withstand the high strains that occur during folding when the propellant is expelled. Rubber-like bladders give rise to other problems, however, since they tend to have a high permeability (gases and liquids diffuse through them), and they often react chemically with the propellants.

The problems of fatigue failures, permeability, and chemical compatibility have led to the application of composite materials for bladders. For example, a composite, laminated bladder may have outer layers made of teflon or mylar (to avoid reaction with propellants) and an inner layer of metal foil (which provides a diffusion barrier). Elastomer layers may also be used, to provide the composite with greater flexibility. Naturally, the question which then arises is how to select the materials and the

thicknesses of the various laminates to obtain the best overall bladder performance and maximum life expectancy.

In response to the problem of composite bladder design, the objective of this study is to conduct an analytical program for improving the performance, efficiency, and operating life (i.e., recycling capability) of these propellant expulsion devices. Experience indicates that the majority of bladder failures are associated with regions of high strain that occur either when the bladder folds and wrinkles as the propellant is expelled or during vibration when sloshing occurs. Typical folds and creases that a bladder undergoes are illustrated in Figure 1-1; the various folds can be roughly classified as: a) simple folds, or b) double folds. These folds can occur in various combinations, which result in three-corner folds, creases, wrinkles, and points. A particularly severe fold which frequently occurs is the traveling crease, or a rolling double fold. Such traveling folds motivated the design of the J.P.L. crease tester.

To achieve the program objective (e.g., to improve bladder performance and fatigue life), the present study will be devoted to: a) obtaining the low-cycle fatigue life of bladders fabricated from composite materials; and b) obtaining a better understanding of the principal parameters that effect bladder life expectancy. To determine the fatigue life of composite bladders, an analysis of the strain in simple and double folds for composite bladders will be conducted. From those strains, the fatigue life of the bladder will be predicted.

Since material properties, thicknesses, and fabrication techniques introduce statistical variations into the fatigue problem, it is recognized that the approach just outlined may exhibit a large variance about some estimated mean fatigue life. However, it is our strong conviction that such an approach will correctly portray the ordering of the life expectancies of the various composites; that is, the analysis will indicate which arrangements of laminate materials and thicknesses result in maximum fatigue life. Hence, it is felt that agreement between the calculated performance and the experimental fatigue life of actual bladders will definitely be obtained. Thus, the analytical model will provide the Propulsion Engineer with a rational means of designing bladders.

1-2
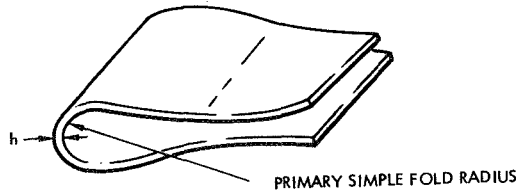
a. Simple Fold



b. Double Fold
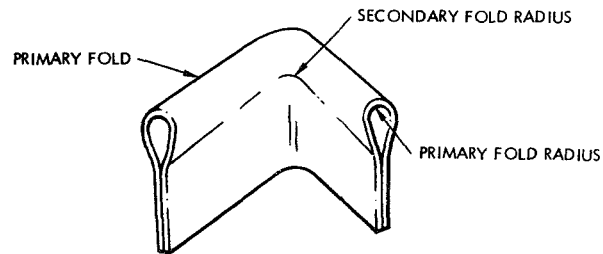


Figure 1-1. Simple and Double Folds

I.1 Project Plan

During the first month of this project, a project plan was formulated which defined various tasks and sub-tasks. This plan is shown in Table 1-1. Since the project plan was closely followed during this contract, this final report will be organized according to the tasks given in Table 1-1.

TABLE 1-1.  Project Plan

Tasks

1.0  Literature Survey and Review

Collect data on material properties and fatigue
life

2.0  Analysis of Simple Folds

2.1  Formulate and program an "n-layered" model

2.2  Formulate and program a two-dimensional
finite element model

2.3  Conduct experiments on simple folds

2.4  Compare theory and experiment;
Refine the analysis

2.5  Investigate the influence of traveling
and rolling

2.6  Estimate fatigue life of simple folds

3.0  Analysis of Double Folds

3.1  Formulate and program an axisymmetric
finite element model

3.2  Conduct experiments on double folds

3.3  Compare theory and experiment;
refine the analysis

3.4  Investigate the influence of traveling
and rolling

3.5  Estimate fatigue life of double folds

4.0  Computer Program

Prepare and document a computer program based
upon the finite element model(s).

5.0  Final Report

## II.  TASK 1.0:  LITERATURE SURVEY AND REVIEW

In this section, the following three questions are answered:  1)
What type of bladder folding fatigue test makes sense?; 2) How can single
and double fold fatigue tests be related to uniaxial test data?;  3) What
fatigue results are available for bladder materials?  Answers to these
questions presented here are based upon study of the collected literature
to date.  It is possible that further investigation of additional references
could modify these points of view.

### II.1  Fatigue Test Modes

### II.1.1  Repeated Straining and Reversed Straining

Since the operation life of a bladder depends on the low-cycle
fatigue property of the material and low-cycle fatigue behavior is governed
by the plastic strain range of each cycle, it is only necessary to consider
whether it is desirable to conduct bladder folding fatigue tests as "repeated
straining" tests or "reversed straining" tests.

As an example of the <u>repeated</u> straining test, Evans (Ref. 1) applied
repeated constant increments of longitudinal tensile strains (with plastic
strains ranging from zero to $\varepsilon_p$) to copper and mild steel wires and obtained
the results (Ref.2)

$$N = \varepsilon_f / \varepsilon_p \qquad (2.1)$$

where      $N$ = number of cycles to failure

$\varepsilon_f$ = fracture strain

$\varepsilon_p$ = plastic strain

As an example of the <u>reversed</u> straining test, Coffin and Tavernelli
(Ref. 3) applied cyclic strains between maximum tensile strain of $+\varepsilon_p/2$
and maximum compressive strain of $-\varepsilon_p/2$ to their metal specimens (with
total plastic strain range of $\varepsilon_p$ in each cycle) and obtained the results

$$\varepsilon_p \sqrt{N} = \text{constant} = C \tag{2.2a}$$

$$C = \varepsilon_f / 2 \tag{2.2b}$$

From study of experimental data, treated as a problem of cumulative fatigue damage, Martin (Ref. 4), found that

$$C = \varepsilon_f / \sqrt{2} \tag{2.3}$$

gave a better fit. Substituting Eq. (2.3) into Eq. (2.2a) gives

$$N = \frac{1}{2} \left( \frac{\varepsilon_f}{\varepsilon_p} \right)^2 \tag{2.4}$$

for reversed straining tests.

The results from Eqs. (2.1) and (2.4) agree only if $\varepsilon_f / \varepsilon_p = 2$, which means the applied plastic strain range $\varepsilon_p$ is as high as half of the fracture strain $\varepsilon_f$. For other reasonable strain ranges (which are much lower than $\varepsilon_f$) more cycles of life are obtained with the reversed straining test than the repeated straining test. For example, if $\varepsilon_f / \varepsilon_p = 10$, Eq. (2.1) gives N = 10 cycles for reversed straining, while according to Eq. (2.4), N = 50 cycles for reversed straining.

It is explained in Ref. 5 that during the compressive straining part of the cycle in reversed straining tests some re-welding of the micro-cracks occurs. The current state of understanding of low-cycle fatigue of metals is that microcracks often exist inside the test specimen. Even if they do not exist initially, they begin to form after only a very small number of cycles of straining at sites of microscopic inhomogeneity (crystal boundaries, dislocations, or inclusions). Further straining causes these microcracks to grow. In repeated straining, they grow without any chance of re-welding. In reversed straining, some re-welding is possible (although re-welding does not restore the material). Hence, reversed straining yields more life cycles than repeated straining does at the same level of strain range $\varepsilon_p$ per cycle. (For this comparison the

maximum tensile strain in reversed straining test $+\varepsilon_p/2$ is half of that in repeated straining test, $+ \varepsilon_p$).

II.1.2 <u>Effects of Mean Strains</u>

Perhaps a better explanation from the point of view of (macroscopic) continuum mechanics is the observation presented in Ref. 6 (p. 171) that in reversed straining the mean strain is zero, whereas in repeated straining the mean strain $\delta$ is a tensile strain. In repeated straining tests, the material can be regarded as 1) first being given a mean strain of $\delta$ and then 2) being subjected to a cyclic plastic-strain range of $\varepsilon_p$ with zero mean strain (as in the case of reversed straining). Since the effect of the mean strain or "prestrain" is to reduce the life cycles, we get less cycles to failure in repeated straining than in reversed straining at the same level of strain range $\varepsilon_p$.

For example, one of the approximate formulas for life cycles, including the effect of the mean strain $\delta$ is (Ref. 6, p. 174)

$$N = \left(\frac{D-\delta}{\varepsilon_p}\right)^2 \tag{2.5}$$

where                     $D$ = tensile ductility

$$= \log \frac{A_o}{A_f} = -\log (1-R.A.) \tag{2.6}$$

in which R.A. is the conventional "reduction in area" and $A_o$ and $A_f$ are the initial and final areas of the fracture cross section in the tensile test. In fact D is the "fracture strain" $\varepsilon_f$ used in Eqs. (2.1) and (2.4). As long as $\delta$ is positive (tensile strain), its effect is to reduce the life cycle N. The effect is more substantial in the range where the ratio $D/\varepsilon_p$ is small (hence life cycle N is small) than in the range of high values of $D/\varepsilon_p$ and N.

II.1.3 <u>Preferable Fatigue Test Mode</u>

In folding and unfolding of simple and double folds in a bladder in real life applications, a situation between reversed straining and repeated straining prevails. In some locations the maximum tensile strains will be reversed to compressive strains which rarely reach the same

magnitude as the maximum tensile strains (or vice versa). In other
locations the lowest strains will remain to be tensile (or compressive).
Since repeated straining yields smaller life cycles than reversed strain-
ing, it is more conservative (hence preferable) to conduct bladder folding
fatigue test as the repeated straining type. On the other hand, if tests
are to be conducted to obtain uniaxial fatigue data it is preferable to
use the reversed straining type since this type of loading gives nearly
straight line relations between $\varepsilon_p$ and N on log-log coordinates and test
results can be readily compared with available data which are mostly of
reversed straining type. Should the tests be conducted as the reversed
straining type, the resulting life cycles N must be divided by a factor
of safety (greater than one) to account for shorter life in case of repeat-
ed straining.

## II.2   Use of Uniaxial Test Data to Interpret Results from Multiaxial
### Fatigue Tests

### II.2.1   A General Procedure of Life Prediction Considering Both Plastic
### and Elastic Strains

Whether the stress applied to a test specimen is uniaxial or multi-
axial, the resulting total strain (containing both elastic and plastic
components) will be triaxial. Thus, simple and double fold fatigue tests
will provide a continuous record of the principal strains $\varepsilon_1$, $\varepsilon_2$ and $\varepsilon_3$.
In order to predict fatigue life of the specimen with the three components
of total strains specified throughout a cycle by available uniaxial fatigue
test data, Manson (Ref. 6, p. 169) hypothesized a general procedure which
consists of the following steps:

### II.2.1.1   Plot Uniaxial Relation between Plastic-Strain Range and Cycle
### Life

If a plot is made on logarithmic coordinates of the plastic-strain
range $\varepsilon_p$ versus the number of cycles to failure N in a uniaxial reversed
straining test, the result is very nearly a straight line given by the
equation

$$\varepsilon_p = MN^z \tag{2.7}$$

where M and z are material constants. These constants can be either determined by direct measurements from uniaxial fatigue tests (Ref. 6, p.143) or computed by approximate formulas (Ref. 6, pp. 159-161) in terms of various combinations of endurance limit $\sigma_{end}$ (from uniaxial fatigue tests), tensile ductibility D, ultimate tensile strength $\sigma_u$ or/and fracture stress $\sigma_f$ (all from uniaxial static tests).

II.2.1.2  Plot Uniaxial Relation between Elastic-Strain Range and Cyclic Life

If the stress range at the half-life (the "asymptotic stress range", as defined in Ref. 6, p. 128) is divided by the elastic modulus E, the quotient can be regarded as the elastic-strain range $\varepsilon_{e\ell}$ associated with the cyclic life N. A plot of this strain versus cyclic life on log-log coordinates also results in a reasonably straight line given by

$$\varepsilon_{e\ell} = \frac{G}{E} N^{\gamma} \quad \text{(valid for } N < 10^6\text{)} \tag{2.8}$$

where G and $\gamma$ are material constants. Again these constants can be either determined by direct measurements from uniaxial fatigue tests (Ref. 6, p. 143) or computed by approximate formulas (Ref. 6, pp. 159-161) in terms of various combinations of $\sigma_{end}$, $\sigma_u$ and $\sigma_f$.

II.2.1.3  Plot Triaxial Relation between Total Equivalent Strain Range and Cyclic Life

It is shown in Ref. 6 that through the hypothesis of an "equivalent total strain range" $\Delta\varepsilon$ given by

$$\Delta\varepsilon = \frac{\sqrt{2}}{3} \sqrt{[\Delta(\varepsilon_1 - \varepsilon_2)]^2 + [\Delta(\varepsilon_2 - \varepsilon_3)]^2 + [\Delta(\varepsilon_3 - \varepsilon_1)]^2} \tag{2.9}$$

the equation

$$\Delta\varepsilon = \varepsilon_p + \frac{2}{3}(1+\mu)\varepsilon_{e\ell}$$

$$= MN^z + \frac{2}{3}(1+\mu)\frac{G}{E}N^{\gamma} \tag{2.10}$$

relates the triaxial strain ranges to cyclic life prediction based on uniaxial data given by the material constants M, z, G and $\gamma$. Here $\mu$ is

the Poisson's ratio of the material.

Equation (2.10) can be plotted as a strain range $\Delta\varepsilon$ versus cyclic life N curve on log-log coordinates and can be used for cyclic life prediction for the material.

### II.2.1.4 Compute Total Equivalent Strain Range for Given Triaxial Problem

For any problem in which the three principal total strain components (plastic and elastic strains) are specified either from measurement or computation, form the strain differences $\varepsilon_1 - \varepsilon_2$, $\varepsilon_2 - \varepsilon_3$, $\varepsilon_3 - \varepsilon_1$ for the entire load cycle and note the ranges traversed by these strain differences. Substitute these strain difference ranges $\Delta(\varepsilon_1 - \varepsilon_2)$, $\Delta(\varepsilon_2 - \varepsilon_3)$, $\Delta(\varepsilon_3 - \varepsilon_1)$ into Eq. (2.9) to obtain an equivalent total strain range $\Delta\varepsilon$ of the given problem.

### II.2.1.5 Find Cyclic Life From the Curve Eq. (2.10)

Read off the value of N from the curve constructed in step II.2.1.3 (according to Eq. (2.10)) corresponding to the value of $\Delta\varepsilon$ obtained in step II.2.1.4. This is the life prediction for the given problem.

It is clear then, that the procedure described above allows comparison of the cyclic life from simple and double fold fatigue tests with that predicted by uniaxial fatigue or/and static test data. It also allows prediction of cyclic life for any problem where the triaxial total strains are specified for the entire load cycle.

### II.2.2 Simplified Procedure of Life Prediction Neglecting Elastic Strains

A typical $\Delta\varepsilon$ vs. N curve (according to Eq. (2.10)) shows that in the low life range, the elastic component is almost negligible as compared with the plastic component. In this range the total strain $\Delta\varepsilon$ almost coincides completely with the $\varepsilon_p$ vs. N straight line for the plastic component (according to Eq. (2.7)). At the higher cyclic lives, however, the plastic strain rapidly becomes negligible, while the elastic strain retains a relatively high value because of the lower slope of the $\frac{2}{3}(1+\mu)\varepsilon_{e\ell}$ vs. N straight line with $\varepsilon_{e\ell}$ given by Eq. (2.8). Thus, the $\Delta\varepsilon$ curve approaches tangency to the elastic line. The crossover point between the two curves is, for most materials, in the vicinity of $10^4$ cycles. Thus, if life ranges of less than 1,000 cycles are involved, it

is usually permissible to neglect consideration of the elastic component.
On the other hand, if the problem involves lives in the vicinity of 100,000
cycles, the strain of major interest is the elastic-strain range (or,
equivalently, the stress range). Basically it is probably still localized
plastic flow that induces fatigue, even at the very high lives, but
measurement of the plastic flow is difficult and the stress range apparently
becomes an adequate measure of this localized plastic flow.

For bladder folding applications, the situation is well within the
low life (and high strain) range. The elastic strains may be neglected
(as compared with the plastic strains) for most practical purposes. Then
the procedure of life prediction presented in II.2.1 can be simplified
as follows:

II.2.2.1  Plot Uniaxial Relation Between Plastic Strain Range and Cycle Life

This step is same as in Step II.2.1.1. For the straight line

$$\Delta\epsilon = \epsilon_p = MN^z \tag{2.7}$$

the material constants M and z can be either determined by direct measure-
ments or by one of the following three sets of approximate formulas
(Ref. 6, pp. 159-161).

II.2.2.1.1  Relation Involving Ductibility D

According to Tavernelli and Coffin (Ref. 7)

$$\left.\begin{array}{l} M = D/2 \\[12pt] z = -1/2 \end{array}\right\} \tag{2.11}$$

These values of M and z give consistently conservative values for life
cycle N. According to Martin (Ref. 4), a better fit to experimental data
can be obtained by taking

$$\left.\begin{array}{l} M = D/\sqrt{2} \\[12pt] z = -1/2 \end{array}\right\} \tag{2.12}$$

II.2.2.1.2  Relation Involving Ductibility D, Ultimate Tensile Strength $\sigma_u$ and Fracture Stress $\sigma_f$

$$M = 0.827D\left[1-82\left(\frac{\sigma_u}{E}\right)\left(\frac{\sigma_f}{\sigma_u}\right)^{0.179}\right]^{-1/3}$$

$$z = -0.52 - \frac{1}{4}\log D + \frac{1}{3}\log\left[1-82\left(\frac{\sigma_u}{E}\right)\left(\frac{\sigma_f}{\sigma_u}\right)^{0.179}\right] \qquad (2.13)$$

These values of M and z give better fit to experimental data than Eqs.(2.11) but may be too unconservative.  Manson (Ref. 6, p. 164) suggested division of M by approximately 1.5 to make Eq. (2.13) render predominantly conservative life predictions.

II.2 2.1.3  Relation Involving Ductibility D, Fracture Stress $\sigma_f$ and Endurance Limit $\sigma_{end}$

$$M = 0.827D\left[1-166\left(\frac{\sigma_{end}}{E}\right)\left(\frac{\sigma_f}{\sigma_{end}}\right)^{0.394}\right]^{-1/3}$$

$$z = -0.52 - \frac{1}{4}\log D + \frac{1}{3}\log\left[1-166\left(\frac{\sigma_{end}}{E}\right)\left(\frac{\sigma_f}{\sigma_{end}}\right)^{0.394}\right] \qquad (2.14)$$

The prediction based upon these values of M and z yields slightly improved correlations with experimental data than II.2.2.1.2 at the higher cyclic lives.  This is to be expected since use is essentially made of the long-life data in establishing the endurance limit at $10^7$ cycles.  For application to low-cycle fatigue of bladder folding this refinement is not necessary.

Eqs. (2.11), (2.12) and (2.13) show that it is possible to approximately derive uniaxial fatigue data from uniaxial static test data (D, $\sigma_u$, $\sigma_f$) only.

II.2.2.2  Compute Equivalent Plastic Strain Range for Given Triaxial Problem

This step is same as Step II.2.1.4 except that the total strain range $\Delta\varepsilon$ is assumed to be equal to the plastic strain range $\varepsilon_p$.  The equivalent plastic strain range $\Delta\varepsilon = \varepsilon_p$ is given by Eq. (2.9).

## II.2.2.3  Find Cyclic Life from the Straight Line Eq. (2.7)

Read off the value of N from the straight line constructed in step
II.2.2.1 (according to Eq. (2.7)) corresponding to the value of $\Delta\varepsilon$ obtained
in Step II.2.2.2.  This is the desired life prediction for the given
problem.

## II.2.3  Limitations of Procedure for Multiaxial Strains

When Eq. (2.9) is applied to determine an equivalent total strain
range, the implicit assumption is made that deformation plasticity is
valid.  It is essentially assumed that the principal stresses vary in
direct proportion to each other.  It is also implied that the strain
ranges $\Delta(\varepsilon_1 - \varepsilon_2)$, $\Delta(\varepsilon_2 - \varepsilon_3)$ and $\Delta(\varepsilon_3 - \varepsilon_1)$ are either in phase with each
other or 180° out of phase, for only in this circumstance do the extreme
values occur concurrently.  On the other hand, it is fortuitous that no
consideration need be given to the algebraic sign of these ranges since
they appear in Eq. (2.9) only as squared terms.

However, in the more general case, the strains and strain differences
will be obtained from computations of incremental plasticity.  Loadings may
vary so that there is no direct proportionality among the principal stresses,
and the strains and strain differences may turn out to bear a phase relation
other than 0° or 180°.  Thus, the procedure described in II.2.1 may be
invalid for the more general case.  In fact, the assumption that uniaxial
fatigue data are directly applicable to triaxial fatigue behavior may not
be valid.  For example, multiaxiality of stress may reduce the effective
ductility,   thus invalidating predictions based on uniaxial fatigue tests
or axial tensile tests.  The phase angle is another important variable
regarding which little experimental information is available.  When such
information does become available, the procedure may readily be modified.
Until then, however, it is reasonable to assume that conservatism introduced
by safety factors and other engineering compensations will suffice to over-
come any unconservatism introduced by use of the procedure II.2.1 for
treatment of triaxial strains.

When both elasticity and plasticity are involved, the relationship
between stress and strain can become very complicated, even under relative
simple loading conditions.  It is reasonable to assume that no simple

hypothesis for behavior which is suitable for practical applications can be completely rigorous in its description of the performance. The procedures described here are the results of most up-to-date researches in an effort to seek approximate relations which are sufficiently realistic to lead to reasonable approximations of actual behavior.

## II.3  Available Fatigue Results for Bladder Materials

Most fatigue data in the literature pertain to high-cycle (low-strain) behavior in the form of stress amplitude vs. life cycle curves and endurance limits (i.e. the asymptomatic stress amplitude). These data are not useful for the purpose of analyzing bladder folding behavior which requires strain amplitude vs. life cycle relations from low-cycle (high-strain) fatigue tests. The study of low-cycle fatigue has its origin in an attempt to study the effect of cyclic thermal stress. The desired fatigue data can be found from a relatively small number of recent references in connection with such thermal stress problems. In the following, the available data will be listed under several types of information. Only the materials specified in the "Statement of Work" in the contract are considered herein.

### II.3.1  Data from Uniaxial Tests

Most uniaxial fatigue test data for metals and plastics can be represented by the straight line Eq. (2.7) (if plotted on log-log coordinates) in terms of two material constants M and z. In this section, for each material and temperature the $\varepsilon_p$ vs. N data for two points on this straight line will be listed so that the complete range of data can be easily reconstructed by plotting the straight line or by determining the constants M and z based on these two points.

In case of elastomers the fatigue data are given in the form of extension ratio vs. cycle life curves which are not straight lines. Then data for more than two points on each curve will be listed.

### II.3.1.1  Data for Metals

Table 2-1 lists some available data for AISI type 300 series stainless steel, annealed type 1100 aluminum, gold and titanium alloy under various temperatures ranging from -320°F (78°K) to + 200°F (367°K). For comparison and references, data for several materials and temperature

ranges other than those stated above are also included. All data in Table 2-1 (except pure gold) appear to be obtained from reversed straining on bar specimens. Some of the data in Table 2-1 are obtained by using Eq. (2.4) with the values of $\varepsilon_f$ given by static tests cited in the references.

II.3.1.2  Data for Plastics

Table 2-2 lists some available data for Teflon TFE, Teflon FEP and Mylar under various temperatures. Ref. 5 contains some static test results (true stress vs. true strain relations) for Teflon felt sheets at room temperature and at 200°F. Since "failure" is defined as the appearance of a surface crack on the sheet, it loses its meaning for Teflon felt sheets because they are already quite porous before any imposed deformation. For this reason they are never used alone as a bladder material, but merely serve as a separation between sheets of other materials. In this capacity, the only concern is that they maintain their overall material continuity as a sheet. The fracture strain of the unimpregnated Teflon felt is much larger than that of all the other materials considered. Therefore, when used in laminations with other materials, unimpregnated Teflon felt will never break before other materials do. However, this is not true for impregnated Teflon felts.

II.3.1.3  Data for Elastomers

Table 2-3 lists some available data for Parker EPR, RMD EPR and RMD Nitroso rubbers at room temperature. For elastomers the fatigue life N is a function of the extension ratio $\lambda$ defined as (Ref. 15) (in uniaxial tests).

$$\lambda = \frac{\text{deformed axial length}}{\text{original axial length}} \tag{2.15}$$

The $\lambda$ vs. N curves are in general not straight lines on log-log coordinates. Hence, more than two data points are listed under each material.

II.3.2  Data from Folding Tests

In Ref. 27, a series of rolling of double fold test results are reported for TFE and FEP Teflon sheets and Teflon TFE/FEP laminates (of equal thicknesses). These tests have been performed in various propellants and simulated propellants (or air) at temperatures ranging from 35°F to

75°F.  The results are summarized in Table 2 4.

II.3.3  <u>Data from which Cycle Life can be Computed</u>

Some of the data in Table 2-1 have been obtained by using Eq. (2.4) with the values of fracture strain $\varepsilon_f$ (or tensile ductibility D) given by static tests.  Similarly, the approximate cycle life N may be computed for a given strain range $\varepsilon_p$ if the various combinations of test results on ductibility D, ultimate tensile strength $\sigma_u$, fracture stress $\sigma_f$ and endurance limit $\sigma_{end}$ as given in Eqs. (2.11) through (2.14) are available. Some of these data are collected in Table 2-5.

Table 2-1  Uniaxial Fatigue Test Data for Metals

| Material | Test Mode | Temperature | Specimen Shape | Plastic Strain Range $\varepsilon_p$ | Number of Cycles to Failure  N | References |
|---|---|---|---|---|---|---|
| Aluminum 1100 | reversed straining | 300°K | bar | 0.28 | 10 | 8 |
| | | | | 0.008 | $10^4$ | 8 |
| 347 Stainless Steel | static test and Eq. (2.4) | 300°K | bar | 0.30 | 10 | 9 |
| | | | | 0.009 | $10^4$ | 9 |
| | | 120°K | | 0.27 | 10 | 9 |
| | | | | 0.0075 | $10^4$ | 9 |
| | | 5°K | | 0.17 | 10 | 9 |
| | | | | 0.005 | $10^4$ | 9 |
| 6Al-4V Titanium | reversed straining | 300°K | bar | 0.30 | 10 | 10 |
| | | | | 0.0014 | $10^4$ | 10 |
| Iodide Titanium | static test and Eq. (2.4) | 300°K | bar | 0.40 | 10 | 9 |
| | | | | 0.012 | $10^4$ | 9 |
| | | 120°K | | 0.50 | 10 | 9 |
| | | | | 0.016 | $10^4$ | 9 |
| | | 5°K | | 0.21 | 10 | 9 |
| | | | | 0.0064 | $10^4$ | 9 |
| 347 Stainless steel | reversed straining | 300°K | bar | 0.20 | 10 | 8 |
| | | | | 0.007 | $10^4$ | 8 |
| Pure Titanium | static test and Eq. (2.4) | 300°K | bar | 0.16 | 10 | 11 |
| | | | | 0.006 | $10^4$ | 11 |
| | | 195°K | | 0.21 | 10 | 11 |
| | | | | 0.0075 | $10^4$ | 11 |
| | | 78°K | | 0.27 | 10 | 11 |
| | | | | 0.009 | $10^4$ | 11 |
| | | 5°K | | 0.18 | 10 | 11 |

Table 2-1  Uniaxial Fatigue Test Data for Metals (Cont'd.)

| Material | Test Mode | Temperature | Specimen Shape | Plastic Strain Range $\varepsilon_p$ | Number of Cycles to Failure N | References |
|---|---|---|---|---|---|---|
| | | | | 0.006 | $10^4$ | 11 |
| Pure Gold | static test and estimate | 300°K | wire | 0.51 | 10 | 5 |
| | | | | 0.017 | $10^4$ | 5 |
| | | 78°K | | 0.42 | 10 | 5 |
| | | | | 0.014 | $10^4$ | 5 |
| 6061-T6 Aluminum | static test and Eq. (2.4) | 300°K | bar | 0.09 | 10 | 12 |
| | | | | 0.003 | $10^4$ | 12 |
| | | 78°K | | 0.15 | 10 | 12 |
| | | | | 0.004 | $10^4$ | 12 |
| | | 20°K | | 0.17 | 10 | 12 |
| | | | | 0.005 | $10^4$ | 12 |
| Annealed 4130 Steel | reversed straining | 300°K | bar | 0.28 | 10 | 6 |
| | | | | 0.003 | $10^4$ | 6 |
| Titanium | reversed straining | 300°K | bar | 0.25 | 4 | 13 |
| | | | | 0.021 | 1500 | 13 |
| Annealed 304 Steel | reversed straining | 300°K | bar | 0.12 | 25 | 13 |
| | | | | 0.016 | 60 | 13 |
| Annealed 310 Steel | reversed straining | 300°K | bar | 0.24 | 14 | 13 |
| | | | | 0.03 | 330 | 13 |
| Annealed 350 Steel | reversed straining | 300°K | bar | 0.09 | 7 | 13 |
| | | | | 0.018 | 230 | 13 |
| 2014 T-6 Aluminum | reversed straining | 300°K | bar | 0.20 | 4 | 13 |
| | | | | 0.02 | 400 | 13 |
| 5456 H311 Aluminum | reversed straining | 300°K | bar | 0.13 | 7 | 13 |
| | | | | 0.03 | 200 | 13 |

Table 2-2  Uniaxial Fatigue Test Data for Plastics

| Material | Test Mode | Temperature | Specimen Shape | Plastic Strain Range $\varepsilon_p$ | Number of Cycles to Failure $N$ | References |
|---|---|---|---|---|---|---|
| Teflon TFE | reversed straining | room | bar | 0.78 | 10 | 5 |
| | | | | 0.30 | $10^3$ | 5 |
| | | 200°F | | 0.72 | 10 | 5 |
| | | | | 0.10 | $10^3$ | 5 |
| Teflon FEP | reversed straining | room | bar | 0.81 | 10 | 5 |
| | | | | 0.55 | $10^3$ | 5 |
| | | 200°F | | 0.90 | 10 | 5 |
| | | | | 0.75 | $10^3$ | 5 |
| Mylar | static test and estimate | room | sheet | 0.63 | 10 | 5 |
| | | | | 0.20 | $10^3$ | 5 |
| | | 200°F | | 0.37 | 10 | 5 |
| | | | | 0.05 | $10^3$ | 5 |
| Teflon TFE | repeated stressing | 300°K | not given | 0.05 | 1500 | 14 |
| | | | | 0.042 | 13000 | 14 |
| Teflon FEP | repeated stressing | 300°K | not given | 0.0075 | 900 | 14 |
| | | | | 0.0055 | 1500 | 14 |

Table 2-3 Uniaxial Fatigue Test Data for Elastomers

| Material | Specimen Shape | Test Mode | Temperature | Extension Ratio $\lambda$ | Number of Cycles to Failure N | References |
|---|---|---|---|---|---|---|
| Parker EPR No. 505-8 | tensile strip | repeated stretching | room | 2.88 | 10 | 5,16-26 |
| | | | | 2.19 | $10^2$ | 5,16-26 |
| | | | | 1.77 | $10^3$ | 5,16-26 |
| | | | | 1.51 | $10^4$ | 5,16-26 |
| | | | | 1.35 | $10^5$ | 5,16-26 |
| | | | | 1.24 | $10^6$ | 5,16-26 |
| | | | | 1.15 | $10^7$ | 5,16-26 |
| RMDEPR No. 132 | tensile strip | repeated stretching | room | 2.89 | 3000 | 5,16-26 |
| | | | | 2.44 | $10^4$ | 5,16-26 |
| | | | | 1.88 | $10^5$ | 5,16-26 |
| | | | | 1.56 | $10^6$ | 5,16-26 |
| | | | | 1.37 | $10^7$ | 5,16-26 |
| | | | | 1.25 | $10^8$ | 5,16-26 |
| RMD Nitroso Rubber | tensile strip | repeated stretching | room | 2.62 | $10^3$ | 5,16-26 |
| | | | | 1.94 | $10^4$ | 5,16-26 |
| | | | | 1.55 | $10^5$ | 5,16-26 |
| | | | | 1.34 | $10^6$ | 5,16-26 |
| | | | | 1.21 | $10^7$ | 5,16-26 |

Table 2-4  Rolling of Double Fold Test Results for Teflon (Ref. 27)
(+ indicates no failure)

| Specimen | Thickness (mils) | Environment | Temperature (°F) | Range of Number of Cycles to Failure (N) | Number of Tests |
|---|---|---|---|---|---|
| TFE sheets | 6 | air | 75 | 3300-5100 | 5 |
| | 3 | air | 75 | 2800-7600 | 3 |
| | 14 | air | 75 | 20,200 | 1 |
| | 6 | Methylene Chloride | 75 | 8000 + | 1 |
| FEP sheets | 3 | air | 75 | 70-90 | 2 |
| TFE/FEP Laminates | 6 | air | 75 | 900-6000 + | 22 |
| | | air | 35 | 3200-6000 + | 2 |
| | | 50% Hydrazine-50% UDMH | 75 | 400-850 | 4 |
| | | | 35 | 75-250 | 4 |
| | | UDMH (unsymmetrical Dimethyl Hydrazine) | 75 | 5000 + | 2 |
| | | | 35 | 50-5000 + | 5 |
| | | MMH | 75 | 5000+ -25500 | 4 |
| | | | 35 | 150 | 2 |
| | | Nitrogen Tetroxide $N_2O_4$ | 50 | 2600 | 1 |
| | | | 60 | 5000 | 1 |
| | | | 35 | 100-5000+ | 8 |
| | | Methylene Chloride | 51 | 6000 + -32750 + | 3 |
| | | | 35 | 300- 5000+ | 2 |
| TFE/FEP Laminates | 6 | Freon TF | 75 | 11000 + | 2 |
| | | | 56 | 32,750 + | 1 |
| | | | 35 | 6000 + | 2 |
| | | 50% Isopropanol - 50% water | 75 | 1000-6000 + | 4 |
| | | | 35 | 100-300 | 4 |
| | 3 | air | 75 | 1800 | 2 |

Table 2-4  (Cont'd.)

| Specimen | Thickness (mils) | Environment | Temperature (°F) | Range of Number of Cycles to Failure (N) | Number of Tests |
|---|---|---|---|---|---|
| | | | 35 | 1700-4100 | 2 |
| | | Freon TF | 75 | 6000 + | 2 |
| | | | 35 | 6000 + | 1 |
| | 12 | air | 75 | 5400 + - 11500 | 2 |
| | | 50% Hydro-zine - 50% UDMH | 35 | 50-250 | 3 |
| | | UDMH | 75 | 5000 + | 1 |
| | | MMH | 75 | 5000 + | 1 |
| | | $N_2O_4$ | 55 | 5000 + - 18000+ | 2 |
| | | Methylene Chloride | 51 | 5000 + | 1 |
| | | | 35 | 5000 + | 1 |

Table 2-5  Test Data from which Cycle Life can be Computed

| Material | Temperature | Environment | Ductibility $D$ | Ultimate Tensile Strength $\sigma_u$ (psi) | Fracture Stress $\sigma_f$ (psi) | Endurance Limit $\sigma_{end}$ (psi) | Modulus of Elasticity $E$ (psi) | References |
|---|---|---|---|---|---|---|---|---|
| Teflon TFE | 212°F | air | | 770 | | | | 14 |
| | 73°F | air | | 1850 | | | | 14 |
| | -69°F | air | | 4650 | | | | 14 |
| Teflon FEP | 212°F | air | | 850 | | | | 14 |
| | 73°F | air | | 2100 | | | | 14 |
| | -62°F | air | | 4550 | | | | 14 |
| Teflon TFE | room | air | | | | 1400 | | 14 |
| Teflon FEP | room | air | | | | 970 | | 14 |
| Teflon FEP (with Type 181 Glass Cloth Reinforcement) | 300°K | air (repeated stressing) | | 24,530 | | 12,000 | | 28 |
| | 78°K | | | 65,740 | | 25,000 | | 28 |
| | room | air | | 24,500 | 20,000 | | $2.5 \times 10^6$ | 29 |
| | 20°K | air | | 80,000 | 67,000 | | $3.5 \times 10^6$ | 29 |
| Teflon TFE bar | room | air | 1.02 | | 6,600 | | | 5 |

Table 2-5  Test Data from which Cycle Life can be Computed  (Cont'd.)

| Material | Temperature | Environment | Ductibility D | Ultimate Tensile Strength $\sigma_u$ (psi) | Fracture Stress $\sigma_f$ (psi) | Endurance Limit $\sigma_{end}$ (psi) | Modulus of Elasticity E (psi) | References |
|---|---|---|---|---|---|---|---|---|
| Teflon TFE sheet | 200°F | air | 1.00 | 3,400 | | | | 5 |
| | room | air | 1.28 | | 11,400 | | | 5 |
| Mylar sheet | 200°F | air | 1.03 | | 6,000 | | | 5 |
| | room | air | 0.95 | | 52,000 | | | 5 |
| Teflon FEP bar | 200°F | air | 0.77 | | 31,000 | | | 5 |
| | room | air | 1.52 | | 20,000 | | | 5 |
| Teflon FEP sheet | 200°F | air | 1.48 | | 8,000 | | | 5 |
| | room | air | 1.47 | | 15,000 | | | 5 |
| Teflon Felt (impregnated) | 200°F | air | 0.92 | | 3,700 | | | 5 |
| | room | air | 1.01 | | 190 | | | 5 |
| Teflon Felt (unimpreg-nated) | 200°F | air | 0.23 | | 225 | | | 5 |
| | room | air | 3.20 | | 260 | | | 5 |
| Teflon TFE (biaxial tension) | 200°F | air | 1.42 | | 40 | | | 5 |
| | 73°F | air | 1.13 | 3130 | 1,800 | | | 27 |

Table 2-5  Test Data from which Cycle Life can be Computed (Cont'd.)

| Material | Temperature | Environment | Ductibility D | Ultimate Tensile Strength $\sigma_u$ (psi) | Fracture Stress $\sigma_f$ (psi) | Endurance Limit $\sigma_{end}$ (psi) | Modulus Of Elasticity E (psi) | References |
|---|---|---|---|---|---|---|---|---|
| | 76°F | Freon TF | 0.79 | 2120 | 1200 | | | 27 |
| | 76°F | Methylene Chloride | 0.41 | 2750 | 2240 | | | 27 |
| | 35°F | Methylene Chloride | 0.41 | 4000 | 3050 | | | 27 |
| Teflon TFE (biaxial tension) | 73°F | air | 0.19 | 2680 | 2500 | | | 27 |
| | 35°F | air | 0.25 | 4050 | 3040 | | | 27 |
| | 110°F | air | 0.30 | 2510 | 2050 | | | 27 |
| | 35°F | Freon TF | 0.25 | 2580 | 1900 | | | 27 |
| Teflon TFE/ FEP Laminates (biaxial tension) | 73°F | air | 0.62 | 3400 | 1830 | | | 27 |
| | 35°F | air | 0.44 | 4220 | 3030 | | | 27 |
| | 110°F | air | 0.81 | 2720 | 900 | | | 27 |
| | 76°F | Freon TF | 0.84 | 1600 | 810 | | | 27 |
| | 76°F | Methylene Chloride | 0.34 | 3400 | 2150 | | | 27 |

II.4 <u>Bibliography on Bladder Folding Strains</u>

1. Aerojet-General Corp., Sacramento, Calif.
   INVESTIGATION OF THE COMPATIBILITY OF GOLD BRAZE ALLOYS WITH AEROZINE
   50, Rept. No. AGC 3332, 8 Nov. 67, NASA CR-65806.

2. Alfred, T.
   MECHANICAL BEHAVIOR OF HIGH POLYMERS, New York, Interscience, 1948,
   581, p.

3. American Society for Metals
   FRACTURING OF METALS, Cleveland, ASM, 1948.

4. Andrews, E. H.
   FRACTURE IN POLYMERS, Edinburgh, Oliver & Boyd, 1968.

5. ASTM, Committee E-9 on Fatigue
   A GUIDE FOR FATIGUE TESTING AND THE STATISTICAL ANALYSIS OF FATIGUE
   DATA, Philadelphia, ASTM, 1963.

6. ASTM, Committee E9 on Fatigue
   MANUAL ON FATIGUE TESTING, Philadelphia, P., 1949, 82 p.

7. ASTM SYMPOSIUM ON BASIC MECHANISMS OF FATIGUE, (Boston, 23 Jun 58),
   Philadelphia, ASTM 1959.

8. ASTM SYMPOSIUM ON FATIGUE CRACK PROPAGATION, (Atlantic City, 26 Jun-
   1 July 1966) Philadelphia, ASTM, 1967, 542 p.

9. Averbach, B. L.
   FRACTURE, PROCEEDINGS OF AN INTERNATIONAL CONFERENCE ON THE ATOMIC
   MECHANISMS OF FRACTURE, (Swampscott, Mass., 12-16 Apr 59) New York,
   Wiley, 1959, 646 p.

10. Avery, D. H. and W. A. Backofen
    "Nucleation and Growth of Fatigue Cracks," In FRACTURE OF SOLIDS, by
    D. C. Drucker and J. J. Gilman, New York, Interscience Publishers, 1963.

11. Battelle Memorial, Columbus, Ohio
    STATE-OF-THE-ART SURVEY OF METALLIC BELLOWS AND DIAPHRAGMS FOR
    AEROSPACE APPLICATIONS, by L. E. Hulbert, et al., Nov 65, AFRPL-TR-65-125.

12. Battelle Memorial Inst., Columbus,Ohio
    A SUMMARY OF THE THEORY OF FRACTURE ON METALS, by J. W. Spretnak, Rpt.
    No. DMIC 157, 7 Aug 61.

13. Battelle Memorial, Columbus, Ohio
    A SUMMARY REPORT ON THE DEVELOPMENT OF ANALYTICAL TECHNIQUES FOR BELLOWS
    AND DIAPHRAGM DESIGN, by L. E. Hulbert, Aug 66, AFRPL-TR-66-181.

14.  Beebe, W. M.
     AN EXPERIMENTAL INVESTIGATION OF DYNAMIC CRACK PROPAGATION IN PLASTIC
     AND METALS, Phd. Thesis, Calif. Inst. of Tech., Pasadena, 1966.

15.  Beeach Aircraft Corp. Boulder, Colo.
     DEVELOPMENT OF POSITIVE EXPULSION SYSTEMS FOR CRYOGENIC FLUIDS, (final
     rept., phases 2 and 3) by J. E. Bell, et al., Rept. No. BEECH-ER-
     13511, May 62, SSD-TDR-62-14, DDC AD 276 984.

16.  Bell Aerosystems Co., Buffalo, N. Y.
     ANALYSIS OF METALLIC EXPULSION BELLOWS DESIGN, Rept. No. BAC-7230-
     933014, Feb 68.

17.  Bell Aerosystems Co., Buffalo, N. Y.
     STUDY OF ZERO-GRAVITY POSITIVE EXPULSION TECHNIQUES DESIGN OF WELDED
     BELLOWS, Rept. No. R8230-933013, Nov 66.

18.  Boeing Co., Seattle, Wash.
     ESTIMATION FOR A FAMILY OF LIFE DISTRIBUTIONS WITH APPLICATIONS
     TO FATIGUE, Math. Note 561, by S. C. Saunders, et al., May 68.

19.  Boeing Co., Seattle, Wash.
     LIQUID HYDROGEN POSITIVE EXPULSION BLADDERS, By K. E. Wiedekamp,
     May 68, NASA CR-72432.

20.  Boeing Co., Seattle, Wash.
     A NEW FAMILY OF LIFE DISTRIBUTIONS, by Z. W. Birnbaum, Math Note
     576, Oct 68, DI-82-0762.

21.  Boeing Co., Seattle, Wash.
     PLANE-STRAIN CYCLIC FLAW GROWTH IN 2014-T62 ALUMINUM AND GA1-4V(ELI)
     TITANIUM, by L. R. Hall, Rept. No. D2-114465-1, Nov 68, NASA CR-72396.

22.  Boeing Co., Seattle, Wash.
     POLYMERIC POSITIVE EXPULSION BLADDERS FOR LIQUID OXYGEN SYSTEMS,
     by J. T. Hoggatt, Jun 68, NASA CR-72418.

23.  Buch, A.
     FATIGUE RESISTANCE OF MATERIALS AND METAL STRUCTURAL PARTS; PROCEEDINGS
     OF AN INTERNATIONAL CONFERENCE HELD IN WARSAW, New York, MacMillan,
     1964, 313 p.

24.  Bunn, C. W. and E. R. Howells
     STRUCTURES OF MOLECULES AND CRYSTALS OF FLUOROCARBONS, Nature,
     v. 174, No. 4429, 18 Sep 54, p 549-551.

25.  California Institute of Technology, Pasadena, Firestone Flight
     Sciences Lab.
     REVIEW OF SOME RUSSIAN PAPERS PERTINENT TO THE FRACTURE OF SOLIDS,
     by M. P. Wnuk, Rept. No. GAL-CIT-120, GAL-CIT-SM-67-9, Sep 67.

26. Coffin, L. F.
    A STUDY OF THE EFFECTS OF CYCLIC THERMAL STRESSES ON A DUCTILE
    METAL, Trans. ASME, v. 76, 1954, p. 931-950.

27. Connecticut Hard Rubber Co., New Haven
    DEVELOPMENT OF RUBBERLIKE MATERIALS FOR APPLICATIONS INVOLVING CONTACT
    WITH LIQUID ROCKET PROPELLANTS, by J. H. Baldridge, Dec 57, WADC-TR-
    651, DDC AD 142 205.

28. CRACK PROPAGATION SYMPOSIUM PROCEEDINGS, (Cranfield, 1961) Bucking-
    hamshire, College of Aeronautics, 1962, 2 vols.

29. Cristescu, N.
    DYNAMIC PLASTICITY, Amsterdam, North-Holland Pub. Co., 1967, 617 p.

30. Defense Documentation Center, Alexandria, Va.
    THEORIES OF CRACK PROPAGATION METALS - A REPORT BIBLIOGRAPHY, 1959-
    May 62, ARB 10535, DDC AD 446 825.

31. Durelli, A. J., et al.
    INTRODUCTION TO THE THEORETICAL AND EXPERIMENTAL ANALYSIS OF STRESS
    AND STRAIN, New York, McGraw, 1958, 498 p.

32. FATIGUE - AN INTERDISCIPLINARY APPROACH, 10th SAGAMORE ARMY MATERIALS
    RESEARCH CONFERENCE, (Raquette Lab., N. Y., 1963).

33. Ford, H.
    ADVANCED MECHANICS OF MATERIALS, New York, Wiley, 1963, 672 p.

34. Forrest, P. G.
    FATIGUE OF METALS, Oxford, Pergamon, 1962, 425 p.

35. FRACTURE OF SOLIDS, PROCEEDINGS OF AN INTERNATIONAL CONFERENCE,
    (Maple Valley, Wash., 21-24 Aug 62), New York, Interscience, 1963,
    708 p.

36. General Dynamics/Convair, San Diego, Calif.
    FRACTURE DATA FOR MATERIALS AT CRYOGENIC TEMPERATURES, by W. E.
    Witzell, Rept. No. GDC-ZZL-67-017, Nov 67, AFML-TR-67-257.

37. Gent, A. N., et al.
    CUT GROWTH AND FATIGUE OF RUBBERS. I. THE RELATIONSHIP BETWEEN CUT
    GROWTH AND FATIGUE, J. Appl. Polymer Sci., v. 8, No. 1, Jan 64,
    p. 455-466.

38. Gent, A. N.
    SOME CHEMICAL EFFECTS IN FATIGUE CRACKING OF VULCANIZED RUBBERS,
    J. Appl. Polymer Sci., v. 6, No. 22, Jul-Aug 62, p. 497-502.

39. Goodier, J. N. and P. G. Hodge
    ELASTICITY AND PLASTICITY, New York, Wiley, 1958, 152 p.

40. Greensmith, H. W.
    RUPTURE OF RUBBER X. THE CHANGE IN STORED ENERGY ON MAKING A SMALL
    CUT IN A TEST PIECE HELD IN SIMPLE EXTENSION, J. Appl. Polymer Sci.,
    v. 7, No. 3, May 63, p. 993-1002.

41. Heywood, R. B.
    DESIGNING AGAINST FATIGUE OF METALS, New York, Reinhold, 1962

42. Hill, R.
    THE MATHEMATICAL THEORY OF PLASTICITY, Corrected edition, Oxford,
    Oxford Univ. Press, 1956.

43. Hoffman, D. and G. Sachs
    INTRODUCTION TO THE THEORY OF PLASTICITY FOR ENGINEERS, New York,
    McGraw, 1953, 276 p.

44. Hughes Aircraft Co., Culver City, Calif.
    AN EVALUATION OF COMPOSITE TEFLON-ALUMINUM FOIL BLADDERS FOR THE
    SURVEYOR VERNIER PROPULSION SYSTEM, by M. R. Bottorff, 2 Mar 67,
    NASA N67-28018.

45. INTERNATIONAL CONFERENCE ON FRACTURE, PROCEEDINGS, (Tokyo, 1965)
    Japanese Soc. for Strength and Fracture of Materials, 1965.

46. INTERNATIONAL CONF. ON THE FATIGUE OF METALS, Sep 56, London,
    Institution of Mechanical Engineers, 1957, 961 p.

47. INTERNATIONAL UNION OF THEORETICAL AND APPLIED MECHANICS - COLLOQUIM
    ON FATIGUE, (Stockholm, 25-27 May 55), Berlin, Spring, 1956.

48. International Union of Theoretical and Applied Mechanics
    NON-HOMOGENEITY IN ELASTICITY AND PLASTICITY: A SYMPOSIUM, (Warsaw,
    2-9 Sep 58), New York, Pergamon, 1959, 528 p.

49. Jet Propulsion Lab., Pasadena, Calif.
    EVALUATION OF THE COMPATIBILITY OF POLYVINYLIDENE FLOURIDE (KYNAR)
    WITH STORABLE LIQUID PROPELLANTS (NIGROGEN TETROXIDE AND HYDRAZINE),
    no date, NASA CR 50999, N63-21363.

50. Johnson, W. and P. B. Mellor
    PLASTICITY FOR MECHANICAL ENGINEERS, Princeton, N. J., Van Nostrand,
    1962, 412 p.

51. Kennedy, A. J.
    PROCESSES OF CREEP AND FATIGUE IN METALS, New York, Wiley, 1963.

52. Kikukawa, M., et al.
    PUSH-PULL FATIGUE STRENGTH OF MILD STEEL AT VERY HIGH FREQUENCIES OF
    STRESS UP TO 100 KC/S, Trans. ASME, J. Basic Eng., v. 87, Ser. D,
    No. 4, Dec 65, p. 857-864.

53. King, I. R. and C. A. Gregory
    METHOD FOR DETECTING PIN-HOLES IN TEFLON SHEETS, Rev. Sci. Inst.,
    v. 32, No. 1, Jun 61, p. 89.

54. Lake, G. J. and P. B. Lindley
    CUT GROWTH AND FATIGUE OF RUBBERS. II. Experiments on a Noncrystalliz-
    ing Rubber, J. Appl. Polymer Sci., v. 8, No. 2, Mar 64, p. 707-721.

55. Lake, G. J. and P. B. Lindley
    FATIGUE OF RUBBER AT LOW STRAINS, J. Appl. Polymer Sci., v. 10, No.2,
    Feb 66, p. 343-351.

56. Lake, G. J. and P. B. Lindley
    ROLE OF OZONE IN DYNAMIC CUT GROWTH OF RUBBER, J. Appl. Polymer Sci.,
    v. 9, No. 6, Jun 65, p. 2031-2045.

57. Lubahn, J. D.
    THE ROLE OF ANELASTICITY IN CREEP, TENSION AND RELAXATION BEHAVIOR,
    Trans. ASM, v. 45, 1953, p. 787-838.

58. McDonnell Douglas Corp., Newport Beach, Calif.
    PRESSURIZATION SYSTEMS DESIGN GUIDE, VOLUEM 3: PRESSURANT GAS
    SOLUBILITY IN LIQUID PORPELLANTS, Rept. No. DAC-60510-Fl, Jul 68.

59. McMahon, W., et al.
    PHYSICAL PROPERTIES, EVALUATION OF COMPOUNDS AND MATERIALS, PART 2.
    DEGRADATION STUDIES OF POLYETHYLENE TEREPHATHALATE (Mylar), J. Chem.
    Eng. Data, v. 4, No. 1, Jan 59, p. 57-85.

60. Mandel, J.
    V. C. Seminaire de Plasticite, Technical Notes, Paris, Air Ministry,
    1962, 179 p.

61. Manson, S. S.
    FATIGUE: A COMPLEX SUBJECT - SOME SIMPLE APPROXIMATIONS, Exper. Mech.,
    v. 5, No. 7, Jul 65, p. 193-226.

62. Manson, S. S.
    THERMAL STRESS AND LOW-CYCLE FATIGUE, New York, McGraw, 1966, 404 p.

63. Martin, D. E.
    AN ENERGY CRITERION FOR LOW-CYCLE FATIGUE, Trans. ASME J. Basic Eng.,
    v. 83, Ser D, No. 4, Dec 61, p. 565-571.

64. Massachusetts Inst. Technology, Cambridge, Aeroelastic and Structures
Research Lab.
ON THE VARIATIONAL PRINCIPLES OF ELASTICY AND PLASTICITY, by K.
Washizu, Rept. No. ASRL-TR-25-18, Mar 55.

65. Mendelson, A.
PLASTICITY; THEORY AND APPLICATION, New York Mac Millan, 1968, 353 p.

66. Nadai, A.
THEORY OF FLOW AND FRACTURE OF SOLIDS, 2nd ed., New York, McGraw,
1950.

67. National Astronautics and Space Administration, Washington, D. C.
APPLICATION OF ULTRASONICS TO DETECTION OF FATIGUE CRACKS, by S. J.
Klima, 1965, NASA TMX 52109.

68. North American Aviation, Los Angeles
BASIC FRACTURE MECHANISM AND ELECTRON FRACTOGRAPHY OF FATIGUE FRACTURES,
by C. C. S. Yen, Rept. No. NA 64-1337, 31 Dec 64.

69. Olszak, W., et al.
RECENT TRENDS IN THE DEVELOPMENT OF THE THEORY OF PLASTICITY, New
York, Mac Millan, 1964, 195 p.

70. Porter, R. N. and H. B. Stanford
PROPELLANT EXPULSION IN UNMANNED SPACECRAFT, SAE-ASME paper 868B,
Apr 64.

71. Prager, W.
AN INTRODUCTION TO PLASTICITY, Reading Mass., Addison-Wesley, 1959,
148 p.

72. Prager, W.
THEORY OF PERFECTLY PLASTIC SOLIDS, New York, Wiley, 1951, 264 p.

73. Rocketdyne, Canoga Park
IMPROVEMENT OF EFFICIENCY AND LIFE OF EXPULSION BLADDERS, by H. N.
Chu, Rept. No. R 7391, 29 Feb 68.

74. Rosen, B., ed.
FRACTURE PROCESSES IN POLYMERIC SOLIDS, PHENOMENA AND THEORY, New
York, Interscience, 1964, 835 p.

75. Sinclair, G. M. and T. J. Dolan
EFFECT OF STRESS AMPLITUDE ON STATISTICAL VARIABILITY IN FATIGUE LIFE
OF 75S-T6 ALUMINUM ALLOY, Trans. ASME, v. 75, Jul 53, p. 867-872.

76. Southwell, R. V.
    AN INTRODUCTION TO THE THEORY OF ELASTICITY FOR ENGINEERS AND PHYSICISTS,
    2nd ed., New York, Oxford Univ. Press, 1941, 509 p.

77. Strong, A. G.
    THE OXYGEN FLUORIDES, Chem. Rev., v. 63, No. 6, Dec 63, p. 607-624.

78. Swift & Co., Oak Brook, Ill.
    ADVANCED BLADDER TEHCNOLOGY, GAS IMPERMEABLE PROTEIN FILMS AND LAMINATES,
    no date, no rept. no.

79. Swindeman, R. W. and D. A. Douglas
    THE FAILURE OF STRUCTURAL METALS SUBJECTED TO STRAIN-CYCLING CONDITIONS,
    Trans. ASME J. Basic Eng., v. 81, Ser D, no. 2, Jun 59, p. 203-212.

80. SYMPOSIUM ON FRACTURE TOUGHNESS TESTING AND ITS APPLICATIONS, (Chicago,
    21-26 Jun 64), Philadelphia, ASTM, 1965, 409 p.

81. SYMPOSIUM ON FUNDAMENTAL PHENOMENA IN THE MATERIAL SCIENCES, 1963,
    FRACTURE OF METALS, POLYMERS AND GLASSES, New York, Plenum Press, 1964.

82. SYMPOSIUM ON INTERNAL STRESSES AND FATIGUE IN METALS, ed. aby G. M.
    Rassweiler and W. L. Crabe, (Detroit, Mich., 1958) New York, Elsevier,
    1959.

83. Tavernelli, J. F. adn L. F. Coffin
    A COMPLICATION AND INTERPRETATION OF CYCLIC STRAIN FATIGUE TESTS ON
    METALS, Trans. ASM, v. 51, 1959, p. 438-453

84. Tavernelli, J. F. and L. F. Coffin
    EXPERIMENTAL SUPPORT FOR GENERALIZED EQUATION PREDICTING LOW CYCLE
    FATIGUE, Trans. ASME, J. Basic Eng., v. 84, Ser D, No. 4, Dec 62, p.
    533-541.

85. Thomas, T. Y.
    PLASTIC FLOW AND FRACTURE IN SOLIDS, New York, Academic Press, 1961,
    267 p.

86. Thiolol Chemical Corp., Denville, N. J.
    NITROSO RUBBER EXPULSION BLADDERS FOR NITROGEN TETROXIDE APPLICATION,
    by N. B. Levine, Rept. No. RMD 5094F, Jun 68, AFML TR 68-158.

87. Thomasen, E., et al.
    MECHANICS OF PLASTIC DEFORMATION IN METAL PROCESSING, New York,
    MacMillan, 1965.

88. TRW Inc., Cleveland, Ohio
    ALL METAL VOLATILE LIQUID POSITIVE EXPULSION SYSTEM, By. S. F. Geffoni,
    Rept. no. ER 5980, 15 Jun 64.

89. Varga, O. H.
    STRESS-STRAIN BEHAVIOR OF ELASTIC MATERIALS:  SELECTED PROBLEMS OF
    LARGE DEFORMATIONS, New York, Interscience, 1966, 190 p.

90. Wayne State Univ., Detroit, Mich.
    STATISTICAL TECHNIQUES IN LIFE TESTING, by B. Epstein, 2 Apr 59,
    PB 171 580.

91. Weibull, W.
    FATIGUE TESTING AND ANALYSIS OF RESULTS, New York, Pergamon Press, 1961.

92. Wilkon, M. A.
    DISLOCATIONS AND MECHANICAL PROPERTIES, Univ. of Texas.

93. Yokobori, T.
    THE STRENGTH, FRACTURE AND FATIGUE OF MATERIALS, Groninger, P. Noordhoff,
    1965.

94. Zener, C.
    ELASTICITY AND ANELASTICITY OF METALS, Chicago, U. of Chicago Press,
    1948, 170 p.

III.0  TASK 2.0:  ANALYSIS OF SINGLE FOLDS

The stationary simple fold (or single fold) is shown in Figure 1-1a.
Folds of this type are observed throughout the expulsion cycle.  The strains
associated with the simple fold consist primarily of extension of the out-
side fibers and compression of the inside fibers of the material.  Depending
upon the material and the radii of curvature involved, various approxima-
tions can be made to facilitate the analysis of simple folds.

For example, when the bladder consists of laminated metal and plastic,
a good first approximation is that plane sections through the thickness of
the laminate remain plane after the load has been applied.  This approxima-
tion reduces the analysis to a one-dimensional problem, and only a wedge-
shaped slice of the cross-section need be considered (See Figure 3-1).  For
materials such as elastomers, however, a simple experiment shows that the
"plane sections remain plane" assumption is not valid for very small primary
radii of curvature.  In this case, considerable shearing deformations take
place in the immediate neighborhood of the simple fold.

Thus, the analysis of a stationary simple fold can be divided into
two tasks, one involving no shear (plane sections remain plane), Task 2.1,
and the other including shear deformations, Task 2.2.  Note that the second
analysis (including shear) is two-dimensional in character, since it involves
variations in both the radial and circumferential directions.  Naturally,
this two-dimensional analysis is considerably more complicated than the
"one-dimensional plane sections" approach.

Because of its inherent simplicity, one would prefer to employ the
"plane sections" approximation.  In order to have confidence in this simpli-
fied analysis, however, one must investigate the problem including shear
deformations and determine when the simple analysis is adequate.  From a
physical standpoint, it is apparent that shear deformations will be negligible
as long as derivatives in the circumferential direction (i.e., around the
fold) are sufficiently small.  Thus, it is anticipated that the simplified
analysis will apply when the primary radius is greater than the thickness,
and the two-dimensional analysis will be required when the primary radius
becomes very small.  The method of solution for the two cases is outlined
in the sections which follow.

## III.1   Task 2.1:   Formulate an "N-Layered" Model

In this task, a simplified analytical model is developed to predict strains produced in a single fold of a composite bladder.  The analysis is based on the approach of Hill (Ref. 30) and it makes the following assumptions:   (1) shear strains are neglected; (2) elastic strains are negligible; (3) the Tresca Yield Law is valid; and (4) the materials are perfectly plastic.  Once plastic folding strains are thus computed, they can be used for fatigue life prediction.

## III.2   Elastic Bending of a Laminated Sheet

Consider the elastic bending of a wide laminated sheet where there is negligible strain in the width direction (state of plane strain). Polar coordinates (r, θ) are used as shown in Figure 3-1.
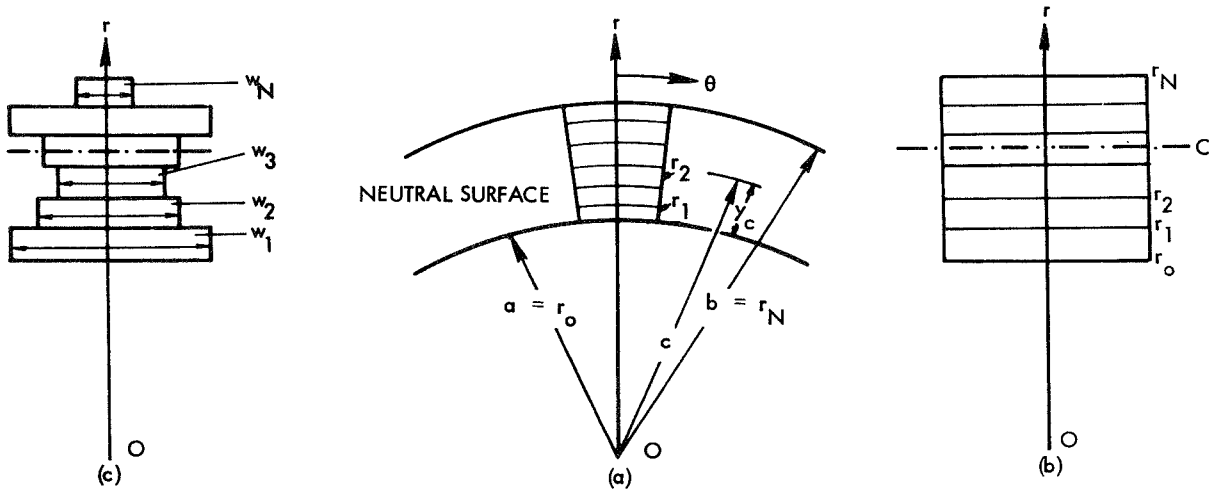


Figure 3-1.   Elastic Bending of a Laminated Sheet

Under pure bending, the strain in the nth layer of the laminated sheet is

$$\varepsilon_{\theta(n)}(r) = \frac{r - c}{c} \qquad (r_{n-1} \leq r \leq r_n) \qquad (3.1)$$

where  c  is the radius of curvature of the neutral surface. If the
material obeys Hooke's law, the stress in the nth layer is given by (see,
for example, Reference 31, Page 5)

$$\sigma_{\theta(n)}\,(r) \;=\; \frac{E_n \varepsilon_{\theta(n)}\,(r)}{1 - \nu_n^2} \tag{3.2}$$

where  $E_n$  and  $\nu_n$  are the modulus of elasticity and Poisson's ratio,
respectively, of the material in the nth layer.  Substituting Equation (3.1)
into Equation (3.2) we have

$$\sigma_{\theta(n)}\,(r) \;=\; \frac{E_n}{1 - \nu_n^2}\left(\frac{r}{c} - 1\right) \qquad (r_{n-1} \leq r \leq r_n) \tag{3.3}$$

To determine the value of  c,  let us consider the bending of an
elemental strip cut from the plate by two planes perpendicular to the
**width**  of the plate and a unit distance (say 1 inch) apart.  We have then
the problem of pure bending of a laminated beam with a cross section as
shown in Figure 3-1(b).  Since materials differ from layer to layer, the
effective cross-sectional area of the beam is as shown in Figure 3-1(c)
where the thickness of each layer is maintained and the width differs from
layer to layer such that for the nth layer the width is

$$w_n \;=\; w_1 \frac{E_n}{E_1} \qquad (w_1 \;=\; 1 \text{ inch}) \tag{3.4}$$

(See, for example, Reference 32, Page 229.)  The neutral surface  $r = c$
must pass through the centroid of this cross-sectional area.  If  $t_n$  is
the thickness of the  nth  layer such that

$$t_n \;=\; r_n - r_{n-1} \tag{3.5}$$

we should have

$$c - r_o = \frac{\sum\limits_{n=1}^{N} w_n t_n \left( y_n - \frac{t_n}{2} \right)}{\sum\limits_{n=1}^{N} w_n t_n} \qquad (3.6)$$

with

$$y_n = \sum_{q=1}^{n} t_q = r_n - r_o \qquad (3.7)$$

Substituting Equation (3.4) into Equation (3.6) we have

$$c = r_o + y_c \qquad (3.8)$$

with

$$y_c = \frac{\sum\limits_{n=1}^{N} E_n t_n \left( y_n - \frac{t_n}{2} \right)}{\sum\limits_{n=1}^{N} E_n t_n} \qquad (3.9)$$

Substituting Equations (3.7) and (3.8) into Equation (3.3) we have

$$\sigma_{\theta(n)}(r_n) = \frac{E_n}{1 - \nu_n^2} \left( \frac{r_o + y_n}{r_o + y_c} - 1 \right) \qquad (3.10)$$

or

$$r_o = \frac{E_n (y_n - y_c)}{(1 - \nu_n^2)\, \sigma_{\theta(n)}(r_n)} - y_c \qquad (3.11)$$

Thus for each value of $\sigma_{\theta(n)}(r_n) = Y_n$, (i.e., if the stress at the outer boundary of the nth layer is the yield stress of the material in the nth layer), we have

$$r_{o(n)}(n) = \frac{E_n}{(1 - \nu_n^2)\, Y_n} \left| y_n - y_c \right| - y_c \tag{3.12}$$

Similarly, if the yield stress occurs at the inner boundary of the layer $\sigma_{\theta(n)}(r_{n-1}) = Y_n$, we have

$$r_{o(n)}(n - 1) = \frac{E_n}{(1 - \nu_n^2)\, Y_n} \left| y_{n-1} - y_c \right| - y_c \tag{3.13}$$

If all the values of $r_{o(n)}(n)$ and $r_{o(n)}(n-1)$ are computed for $n = 1, 2, \ldots N$ the maximum of these values give the value of $a_o = r_o(\text{max})$ when some point in the laminated sheet just starts to become plastic. For any value of $a_o$ which is less than $r_o(\text{max})$, the elastic formulation presented in this section does not hold. Hence, this value of $a_o$ will be used as the initial value of the inner radius of curvature "a" for forward computation of the plastic strains in the laminated sheet. The initial value for the outer radius of curvature "b" is then

$$b_o = a_o + y_N \tag{3.14}$$

and for the radius of the intermediate layers

$$r_n = a_o + y_n \qquad (n = 1, 2, \ldots N) \tag{3.15}$$

Since the circumferential strains are given by Equation (3.1), the original length of the flat unbent laminated sheet $L_o$ is stretched or compressed by the amount

$$\left. \begin{aligned} \Delta L(r_n) &= L_o \varepsilon_{\theta(n)}(r_n) = L_o \frac{r_n - c}{c} \\[2ex] \Delta L(r_{n-1}) &= L_o \varepsilon_{\theta(n)}(r_{n-1}) = L_o \frac{r_{n-1} - c}{c} \end{aligned} \right\} (n = 1, 2, \ldots N) \tag{3.16}$$

at the extreme fibers of the nth layer.

The elastic strains caused by the stretching and compressing of fibers will be considered negligible as compared with the plastic bending strains in the subsequent computation. The sole purpose of this section was to estimate systematically the finite initial radii of curvature for various layers at the start of plastic bending.

### III.3 Forward Numerical Computation of Plastic Bending Strains in a Laminated Sheet

When the initial values of $r_n$ (n = 0, 1, ... N) are systematically determined as in Section III.2, we can proceed to the "forward" computation of plastic bending strains in a laminated sheet. Since maximum strains occur at either of the extreme fibers of each layer, we shall confine our consideration to the strains at these extreme fibers.

If thinning of the layer thickness and movements of the individual fibers are taken into account, the "forward" numerical computation of strains in these extreme fibers of all the layers can be accomplished in the following steps:

a. Location of Neutral Surface as $\alpha = \alpha_o$

1. Compute the initial bending angle $\alpha$ (per unit original length) by the incompressibility condition Reference 30, page 290, Equation (12).

$$\alpha_o = \frac{2}{a_o + b_o} = \frac{2}{r_o(\alpha_o) + r_N(\alpha_o)} \qquad (3.17)$$

2. Assume that the neutral surface $r = c(\alpha_o)$ lies in the qth layer $r_{q_o-1}(\alpha_o) \le r \le r_{q_o}(\alpha_o)$ $(q_o \le N)$. Note that the neutral surface in plastic bending does not necessarily lie in the same layer where the neutral surface in elastic bending lies.

3. Compute the constants $C_n(\alpha_o)$ $(n = q_o, q_o + 1, ... N)$ by

$$C_N(\alpha_o) = -p_o(\alpha_o) - 2k_N \log r_N(\alpha_o)$$

$$C_n(\alpha_o) = C_{n+1}(\alpha_o) - 2(k_n - k_{n+1}) \log r_n(\alpha_o) \tag{3.18}$$

$$(n = q_o, q_o + 1, \ldots N-1)$$

4. Compute the constants $D_n(\alpha_o)$ $(n = 1, 2, \ldots q)$ by

$$D_1(\alpha_o) = -p_i(\alpha_o) + 2k_1 \log r_o(\alpha_o)$$

$$D_n(\alpha_o) = D_{n-1}(\alpha_o) + 2(k_n - k_{n-1}) \log r_{n-1}(\alpha_o) \tag{3.19}$$

$$(n = 2, 3, \ldots q_o)$$

5. Compute $c(\alpha_o)$ from

$$c(\alpha_o) = \text{Exp.} \left[ \frac{D_{q_o}(\alpha_o) - C_{q_o}(\alpha_o)}{4k_{q_o}} \right] \tag{3.20}$$

provided

$$r_{q_o-1}(\alpha_o) < c(\alpha_o) < r_{q_o}(\alpha_o) \tag{3.21}$$

6. If $c(\alpha_o)$ does not satisfy Equation (3.20), assume another layer for location of $c(\alpha_o)$ (i.e., change the value of $q_o$) and repeat steps (2) through (5) until a value of $c(\alpha_o)$ between $r_{q_o-1}(\alpha_o)$ and $r_{q_o}(\alpha_o)$ is obtained.

7. If Equation (3.20) cannot be satisfied for any layer in the sheet, the pressures $p_o(\alpha_o)$ and $p_i(\alpha_o)$ are too high for the analysis to be valid. Proceed to cases with lower values of $p_o(\alpha_o)$ and $p_i(\alpha_o)$.

b. Strain Increments as $\alpha_o$ is Increased by $\Delta\alpha_o$

1. As the angle of bending $\alpha_o$ is increased by a small amount $\Delta\alpha_o$, the decrements of various radii of curvature $r_n(\alpha_o)$ $(n = 0,1,2, \ldots N)$ are

$$\Delta r_n(\alpha_o) = \left[r_n(\alpha_o) + \frac{c^2(\alpha_o)}{r_n(\alpha_o)}\right] \frac{\Delta\alpha_o}{2\alpha_o} \qquad (3.22)$$

Hence, the new radii of curvature $r_n(\alpha_1)$ are

$$r_n(\alpha_1) = r_n(\alpha_o) - \Delta r_n(\alpha_o) \qquad (3.23)$$

2. The instantaneous ("logarithmic") strain increments at the extreme fibers of the various layers are

$$\Delta\varepsilon_\theta\left[\alpha_o, r_n(\alpha_o)\right] = -\Delta\varepsilon_r\left[\alpha_o, r_n(\alpha_o)\right] = \left[1 - \frac{c^2(\alpha_o)}{r_n^2(\alpha_o)}\right] \frac{\Delta\alpha_o}{2\alpha_o} \qquad (3.24)$$

This expression gives tensile circumferential strain increments $\Delta\varepsilon_\theta$ for fibers outside the neutral surface $(r_n > c)$ and compressive circumferential strain increments $\Delta\varepsilon_\theta$ for fibers inside the neutral surface $(r_n < c)$.

3. The new angle of bending $\alpha_1$ can be computed from the incompressibility condition

$$\frac{1}{2}\left[r_N^2(\alpha_o) - r_o^2(\alpha_o)\right] L_o\alpha_o = \frac{1}{2}\left[r_N^2(\alpha_1) - r_o^2(\alpha_1)\right] L_o\alpha_1 \qquad (3.25)$$

or

$$\alpha_1 = \frac{r_N^2(\alpha_o) - r_o^2(\alpha_o)}{r_N^2(\alpha_1) - r_o^2(\alpha_1)} \alpha_o \qquad (3.26)$$

In Equation (3.25), $L_o$ is the original length of the flat laminated sheet.

4. When the angle of bending is $\alpha_o$, the length of the extreme fibers of the nth layer is

$$L_n(\alpha_o) = L_o \alpha_o r_n(\alpha_o) \qquad (n = 0, 1, \ldots N) \qquad (3.27)$$

When the angle of bending is increased to $\alpha_1$, the length of this fiber becomes

$$L_n(\alpha_1) = L_o \alpha_1 r_n(\alpha_1) \qquad (n = 0, 1, \ldots N) \qquad (3.28)$$

Hence, the change of fiber length during plastic bending from $\alpha_o$ to $\alpha_1$ is

$$\Delta L_n(\alpha_o) = L_n(\alpha_1) - L_n(\alpha_o) = L_o \left[ \alpha_1 r_n(\alpha_1) - \alpha_o r_n(\alpha_o) \right] \qquad (3.29)$$

5. If the tension (per unit width applied to the ends of the sheet) necessary to balance the pressures $p_o(\alpha_o)$ and $p_i(\alpha_o)$ during bending is kept constant, the new pressures at the angle of bending $\alpha_1$ are according to Equation (15) on Page 292 of Reference 30.

$$\left.\begin{array}{l} p_o(\alpha_1) = p_o(\alpha_o) \dfrac{r_N(\alpha_o)}{r_N(\alpha_1)} \\[3ex] p_i(\alpha_1) = p_i(\alpha_o) \dfrac{r_o(\alpha_o)}{r_o(\alpha_1)} \end{array}\right\} \qquad (3.30)$$

6. Neglecting the elastic strains, Equation (3.16), we have the cumulated instantaneous "logarithmic" or "natural" strain at $r = r_n$ as $\alpha = \alpha_1$ according to Equation (3.24)

$$\varepsilon_\theta \left[ \alpha_1, r_n(\alpha_1) \right] = -\varepsilon_r \left[ \alpha_1, r_n(\alpha_1) \right] = \Delta\varepsilon_\theta \left[ \alpha_o, r_n(\alpha_o) \right] = \left[ 1 - \frac{c^2(\alpha_o)}{r_n^2(\alpha_o)} \right] \frac{\Delta\alpha_o}{2\alpha_o}$$

$$(3.31)$$

The "conventional" or "engineering" circumferential strain due to plastic bending is from Equation (3.28). (See Reference 30, Page 9)

$$e_\theta \left[ \alpha_1, r_n(\alpha_1) \right] = \frac{L_n(\alpha_1) - L_o}{L_o} = \alpha_1 r_n(\alpha_1) - 1 \tag{3.32}$$

which corresponds to the "logarithmic" circumferential strain of

$$\bar{\varepsilon}_\theta \left[ \alpha, r_n(\alpha_1) \right] = \log \left\{ 1 + e_\theta \left[ \alpha_1, r_n(\alpha_1) \right] \right\} = \log \left[ \alpha_1 r_n(\alpha_1) \right] \tag{3.33}$$

For infinitesimally small bending angle increments, the values of the logarithmic strains computed in Equations (3.31) and (3.33) should agree. Hence, comparison of these values can serve as a guide to the choice of step size $\Delta\alpha/2\alpha$ for the computation.

    c.   Location of Neutral Surface as $\alpha = \alpha_1$

When $r_n(\alpha_1)$ $(n = 0, 1, \ldots N)$, $p_o(\alpha_1)$ and $p_i(\alpha_1)$ are obtained in (b), the steps in (a) can be repeated with $\alpha_o$ replaced by $\alpha_1$ to compute the constants $C_n(\alpha_1)$ and $D_n(\alpha_1)$ and the location of the neutral surface

$$c(\alpha_1) = \text{Exp.} \left[ \frac{D_{q_1}(\alpha_1) - C_{q_1}(\alpha_1)}{4k_{q_1}} \right] \tag{3.34}$$

which is in tne $q_1$th layer of the laminated sheet

$$r_{q_1 - 1}(\alpha_1) < c(\alpha_1) < r_{q_1}(\alpha_1) \tag{3.35}$$

    d.   Strain Increments as $\alpha_s$ is Increased by $\Delta\alpha_s$

The steps (b) and (c) can be repeated for successive increments of the bending angle $\alpha$. During the increment of $\alpha_s$ by a small amount $\Delta\alpha_s$, we have the following expressions for the radii of curvature,

strains, elongations, pressures, and the location of the neutral
surface:

1.  The radii of curvature

$$r_n(\alpha_{s+1}) \;=\; r_n(\alpha_s) - \left[ r_n(\alpha_s) + \frac{c^2(\alpha_s)}{r_n(\alpha_s)} \right] \frac{\Delta\alpha_s}{2\alpha_s} \tag{3.36}$$

2.  The instantaneous "logarithmic" strain increments

$$\Delta\varepsilon_\theta \left[ \alpha_s, r_n(\alpha_s) \right] \;=\; -\Delta\varepsilon_r \left[ \alpha_s, r_n(\alpha_s) \right] \;=\; \left[ 1 - \frac{c^2(\alpha_s)}{r_n^2(\alpha_s)} \right] \frac{\Delta\alpha_s}{2\alpha_s} \tag{3.37}$$

3.  The new angle of bending

$$\alpha_{s+1} \;=\; \frac{r_N^2(\alpha_s) - r_o^2(\alpha_s)}{r_N^2(\alpha_{s+1}) - r_o^2(\alpha_{s+1})} \; \alpha_s \tag{3.38}$$

4.  Fiber lengths

$$L_n(\alpha_{s+1}) \;=\; L_o \alpha_{s+1} r_n(\alpha_{s+1}) \tag{3.39}$$

5.  Outer and inner pressures

$$\left. \begin{aligned} p_o(\alpha_{s+1}) &\;=\; p_o(\alpha_s) \frac{r_N(\alpha_s)}{r_N(\alpha_{s+1})} \\[2em] p_i(\alpha_{s+1}) &\;=\; p_i(\alpha_s) \frac{r_o(\alpha_s)}{r_o(\alpha_{s+1})} \end{aligned} \right\} \tag{3.40}$$

6.  The cumulated instantaneous logarithmic strain at $r = r_n$
as $\alpha = \alpha_{s+1}$ is

$$\varepsilon_\theta \left[ \alpha_{s+1}, r_n(\alpha_{s+1}) \right] = -\varepsilon_r \left[ \alpha_{s+1}, r_n(\alpha_{s+1}) \right] = \sum_{g=0}^{s} \Delta\varepsilon_\theta \left[ \alpha_g, r_n(\alpha_g) \right]$$

$$= \sum_{g=0}^{s} \left[ 1 - \frac{c^2(\alpha_g)}{r_n^2(\alpha_g)} \right] \frac{\Delta\alpha_g}{2\alpha_g} \qquad (3.41)$$

The conventional circumferential strain due to plastic bending is

$$e_\theta \left[ \alpha_{s+1}, r_n(\alpha_{s+1}) \right] = \alpha_{s+1} r_n(\alpha_{s+1}) - 1 \qquad (3.42)$$

which corresponds to the logarithmic circumferential strain

$$\bar{\varepsilon}_\theta \left[ \alpha_{s+1}, r_n(\alpha_{s+1}) \right] = \log \left[ \alpha_{s+1} r_n(\alpha_{s+1}) \right] \qquad (3.43)$$

7. Location of the neutral surface at $\alpha = \alpha_s$ is

$$c(\alpha_s) = \text{Exp.} \frac{\left[ D_{q_s}(\alpha_s) - C_{q_s}(\alpha_s) \right]}{4k_s} \qquad (3.44)$$

where $C_{q_s}(\alpha_s)$ and $D_{q_s}(\alpha_s)$ are computed according to Equations (3.18) and (3.19) with $\alpha_o$ replaced by $\alpha_s$.

e. Total Plastic Bending Strains as $\alpha = \alpha_S$

After S number of small increments of the bending angle $\alpha$, the radii of curvature for various layers (n = 0, 1, 2, ... N) are

$$r_n(\alpha_S) = r_n(\alpha_{S-1}) - \left[ r_n(\alpha_{S-1}) + \frac{c^2(\alpha_{S-1})}{r_n(\alpha_{S-1})} \right] \frac{\Delta\alpha_{S-1}}{2\alpha_{S-1}} \qquad (3.45)$$

The outer and inner pressures are

$$p_o(\alpha_S) = p_o(\alpha_{S-1}) \frac{r_N(\alpha_{S-1})}{r_N(\alpha_S)}$$

$$p_i(\alpha_S) = p_i(\alpha_{S-1}) \frac{r_o(\alpha_{S-1})}{r_o(\alpha_S)}$$

$$\left.\vphantom{\begin{array}{c}1\\1\\1\\1\\1\end{array}}\right\} \quad (3.46)$$

The cumulated instantaneous logarithmic strain at $r = r_n(\alpha_s)$ is

$$\varepsilon_\theta \left[\alpha_S, r_n(\alpha_S)\right] = -\varepsilon_r \left[\alpha_S, r_n(\alpha_S)\right] = \sum_{g=0}^{S-1} \left[1 - \frac{c^2(\alpha_g)}{r_n^2(\alpha_g)}\right] \frac{\Delta\alpha_g}{2\alpha_g} \quad (3.47)$$

The conventional circumferential strain at $r = r_n(\alpha_s)$ is

$$e_\theta \left[\alpha_S, r_n(\alpha_S)\right] = \alpha_S r_n(\alpha_S) - 1 \quad (3.48)$$

which corresponds to the logarithmic strain

$$\varepsilon_\theta \left[\alpha_S, r_n(\alpha_S)\right] = \log \left[\alpha_S r_n(\alpha_S)\right] \quad (3.49)$$

Since the initial thickness of the laminated sheet (before plastic bending strains set in) is

$$t(\alpha_o) = r_N(\alpha_o) - r_o(\alpha_o) \quad (3.50)$$

and the thickness as $\alpha = \alpha_S$ is

$$t(\alpha_S) = r_N(\alpha_S) - r_o(\alpha_S) \quad (3.51)$$

the total thinning of the laminated sheet as $\alpha$ is increased from $\alpha_o$ to $\alpha_S$ is

$$\Delta t = r_N(\alpha_o) - r_N(\alpha_S) - \left[ r_o(\alpha_o) - r_o(\alpha_S) \right] \qquad (3.52)$$

## III.4 Conclusions

The numerical solution for the plastic bending strains in a single fold multilayered bladder by the "forward" computational procedure has been formulated. This procedure requires computation of the elastic strains before plastic strains set in but has the advantage of specifying the initial thicknesses of the layers. Table 3-1 shows some typical numerical results generated using the computer program developed for this analysis.

Table 3-1 - Typical Numerical Results

| Layer | Material | K(PSI) | Folded Thickness (In.) [Total] | Unfolded Thickness (In.) [Total] | Cumulated Log Strain |
|-------|----------|--------|--------------------------------|----------------------------------|----------------------|
| Case 4F (Folded Inner Radius = 0.0127 in.) Forward Calculation | | | | | |
| Inner Surface | | | | | -.6709 |
| 1 | TFE | 800 | .0074 | .005 | |
| | | | | | -.2008 |
| 2 | 1100-0 | 3000 | .0098 | .010 | |
| | | | | | .1998 |
| 3 | TFE | 800 | .0039 | .005 | |
| Outer Surface | | | | | .3217 |
| | | | [.0211] | [.020] | |

### III.5   Task 2.2:   Finite Element Model

When shear deformations are included, it is necessary to consider derivatives in both the radial and circumferential directions, r and $\theta$. To perform this analysis, a two-dimensional "finite element" approach has been developed.  The analysis closely parallels a previous study performed by TRW Systems which calculates elastic-plastic stresses and strains for two-dimensional regions.  However, in the present formulation, large strains and displacements are considered, in addition to elasto-plastic behavior.

A review of the literature revealed that there was no finite element computer code available which solved large plastic strain problems accurately.  Therefore, to satisfy this task, TRW Systems developed a code which could handle such problems, since large plastic strains do indeed develop in single (and double) folds.  This method is based upon an incremental variational principle which is used in a piece-wise linear solution procedure.  An equilibrium check and corrective cycling method are included in the formulation  which prevents the computer solution from straying from the "true" solution.  The present formulation constitutes a major contribution to the state-of-the-art in nonlinear solid mechanics, and will be presented in detail in the following sections. Also included is a literature survey of existing alternate finite element solution procedures.

III.5.1  Introduction and Literature Search

Classical mechanics, despite its increasing sophistication, is
capable of solving only highly idealized structural analysis problems.
This situation is especially obvious for problems involving physical
or material nonlinearities. For this reason, an alternate approach to
such problems, using the finite element method, has become increasingly
popular.  In the finite element approach, the structure or continuum
is modeled by a network of discrete simple structural components, called
finite elements. These elements are joined together at common nodal
points, and the gross behavior of the collection of such nodal points
simulates the behavior of the structure. The field variables, such as
internal displacements, are approximated within each element by inter-
polation on nodal point values. An energy principle is used to generate
the field equations for each element. These equations are assembled,
using compatability of common node point values, to form the field
equations for the entire structure. Structures of various types (plates,
shells, solids, etc.), and of rather arbitrary geometries, can be modeled
using this procedure by careful  selection of the finite element charac-
teristics. Nonlinear structural response can also be studied using the
finite element procedure. In the following sections a literature review
is presented in which finite element approaches to continuum problems
involving geometric nonlinearities, material nonlinearities, and combined
geometric and material nonlinearities are surveyed. Following this
review, a new solution procedure for general nonlinear static structural
response problems is given, which was used for all work reported herein.

Many authors have applied the finite element method to geometrically
nonlinear problems (Refs. 33 - 39). From this work, basically three classes
of finite element formulations can be defined; Class I - Incremental
methods without equilibrium checks; Class II - Direct solutions of the
governing  nonlinear equations; and Class III - Incremental methods with
equilibrium checks.

Historically, Class I was the first finite element approach to

solving geometrically nonlinear problems (Refs. 33, 40, 41). In this method, the load is applied to the structure in small increments, and the incremental displacements due to each load step are determined. Incremental stresses and strains are computed at each step and used in the following load step. Although this method is computationally very fast, it has the disadvantage that equilibrium at any particular load level is not necessarily satisfied. No attempt is made to determine if equilibrium requirements are indeed met, and the same problem must be repeatedly solved using successively smaller load steps to assess the solution accuracy.

The direct solution method (Class II) involves applying the total load to the structure and computing the total response by using mathematical iterative techniques. This approach may be subdivided into two distinct categories; (a) direct minimization of the potential energy; and (b) direct solution of the nonlinear algebraic equilibrium equations.

References 37 and 42 employ mathematical programming methods to numerically minimize the potential energy functional. An advantage of this method is that minimum computer storage is required since no system stiffness matrices are assembled; rather, the potential energy for the system is obtained simply as the scalar sum of the energies of the individual elements. However, if second order gradient methods are used to perform the energy search, in order to speed convergence, this advantage disappears. Additionally, only stable equilibrium configurations can be determined, making the interpretation of the results awkward in some cases (Ref. 43).

In the second category mentioned under Class II, mathematical iterative methods are applied to the governing nonlinear equilibrium equations. Oden (Ref. 38) has applied this scheme successfully to nonlinear elasticity problems. Newton-Raphson interation was used to solve the equilibrium equations.

A major disadvantage of both Class II methods is that they are not applicable to path dependent problems, such as plastic deformation. A summary of the Class I and II methods is given in Ref. 34.

The third class of solution techniques involves determining the

incremental solutions due to a series of load steps and applying equilibrium checks and (if necessary) corrections, to the solution. Unlike Class I, this method insures that the solution satisfies equilibrium throughout the loading history (Refs. 44, 35, & 36). This procedure was introduced by Wissmann (Ref. 44). There are numerous computational schemes that are associated with this class. For example, in order to minimize computer time, Ref. 35 corrects for equilibrium at only every four steps. Ref. 36 iterates at every load step to satisfy equilibrium, but does not necessarily use the "exact" incremental stiffness matrix. Ref. 44 uses a "progressive iteration with back-substitution" method for each load step. The present approach uses the class III method with two different computational refinements. The first is to interate at each load level, using the "exact" stiffness matrix, until equilibrium is satisfied. The second technique is similar to the Class I approach but attempts to correct for equilibrium at each load step by using the unbalance force from one step as a pseudo load in the next step. This method is computationally equivalent to Class I but has the advantage that the solution is continuously monitored and improved.

Other types of nonlinear problems which have been solved using the finite element procedure deal with material nonlinearities, in particular elasto-plastic behavior. Two general methods have been developed for the elasto-plastic analysis of structures. These are, (a) the initial strain method, and (b) the tangent modulus method.

The initial strain method (Refs. 45 & 46) treats the plastic strains at each incremental load step as initial strains for the next load step. In this method, plasticity effects are taken into account as pseudo loads, and the elastic stiffness matrix is used throughout the entire loading process. The advantage of this method is that for small displacements problems, the governing stiffness matrix need be built and "inverted" only once.

The tangent modulus method (Refs. 39, 47, 48, 49, and 50), on the other hand, is based upon the incremental stress-plastic strain laws of

plasticity. In this method, plasticity effects are accounted for in
the stiffness matrix, which is updated at each load step. It should
be noted that when solving large deflection problems by the incremental
methods (Classes I and III), a new stiffness matrix is required at each
load step. Thus, the large deflection incremental methods combine well
with the tangent modulus method, since it also requires a new stiffness
matrix at each load step. As pointed out in Ref. 51, the tangent modulus
method offers the additional advantage of using larger load increments
than when using the initial strain method.

Only a few references have been found in which both geometric non-
linearities and plasticity are treated within the framework of finite
element theory (Ref. 39, 50, and 52). Refs. 39 and 50 use a Class I
method with the tangent modulus approach, while Ref. 52 uses a Class I
method with the initial strain approach.

The present approach develops the governing incremental finite
element equations for large strain, elasto-plastic problems. The
formulation presented is similar to that given by Felippa (Ref. 39) but
uses a different variational principle. The derivation of Ref. 39 is
based on on incremental variational principle that assumes the stresses
at the reference state are in equilibrium with the applied loads. This
leads to an incremental finite element formulation which does not check
to determine if equilibrium is satisfied (i.e., Class I method). The
present method does not assume a priori that the reference state is in
equilibrium. Consequently, the variational principle used herein leads
to a Class III formulation, and equilibrium is checked and controlled
throughout the loading history.

III.5.2   Incremental Variational Principle

In this section, the general formulation of the piece-wise linear
incremental solution of structures problems, involving both material and
geometric nonlinearities, will be presented. This formulation is based
on an incremental variational principle as given by Washizu (Ref. 53).
In the incremental variational principle, the body is considered at an

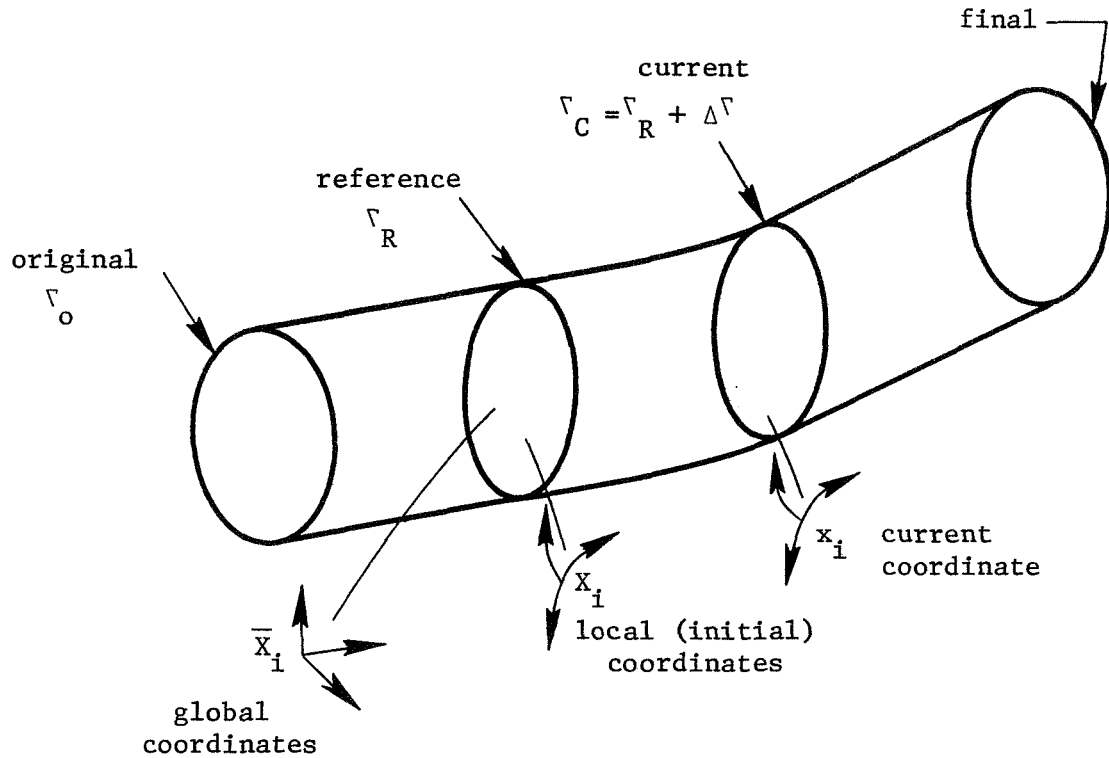an arbitrary reference state $\Gamma_R$ of the load path (See Figure 3-2).



Figure 3-2 - Incremental Procedure

It is assumed that all state variables are known at the reference state $\Gamma_R$. The reference state $\Gamma_R$ may be regarded as the initial stressed state for determining the stresses, strains and displacements of the current state $\Gamma_C$. The current state is assumed to be incrementally close to the reference state (i.e., $\Gamma_C \doteq \Gamma_R + \Delta^\Gamma$). The local initial coordinate system $X_i$ for an element in the body is taken as a Lagrangian frame for the current state $\Gamma_C$. This coordinate system is assumed to be inscribed on the body, and when the body deforms in going from $\Gamma_R$ to $\Gamma_C$ these coordinates also become deformed (convected). The global reference system $\overline{X}_i$ is used to assemble all the elements of the discretized body. For some problems it is convenient to let the local coordinate system $X_i$ and the global coordinate systems $\overline{X}_i$ coincide.

Let $\Delta u_i$ (i = 1,2,3) (measured along the $X_i$ coordinate direction)

be the incremental deflections of a point in the body in going from $\Gamma_R$ to $\Gamma_C$, then

$$x_i = X_i + \Delta u_i \qquad (3.53)$$

describes the relationship between the convected local coordinates (current coordinates) and the initial coordinates.

Consider a structure at the beginning of a particular loading increment N. At this time, the initial coordinates $X_i$ and current coordinates $x_i$ are identical. Assume that stresses $\sigma_{ij}^{(o)}$, surface tractions $T_i^{(o)}$ and body forces $F_i^{(o)}$ are acting on the structure at this time, i.e., prior to the addition of the increment of load for step N. These stresses and loads are with respect to the initial coordinate axis and are referred to a unit of area <u>before</u> the addition of the load increment. The stresses are therefore "true" stresses. For future reference, the area and volume of an element before the load increment is applied will be referred to as the "undeformed" area and volume, respectively. The area and volume <u>after</u> the load increment is applied will be referred to as the "deformed" area and volume, respectively. Next, impose on the structure the incremental surface traction $\Delta T_i$ and body force $\Delta F_i$. These give rise to additional stresses $\Delta\sigma_{ij}$, incremental displacements $\Delta u_i$, and distort the coordinates $x_i$. Thus the <u>total</u> stresses, surface tractions, and body forces at the end of load increment N (at State $\Gamma_C$) are given by

$$\sigma_{ij} = \sigma_{ij}^{(o)} + \Delta\sigma_{ij} \qquad (3.54a)$$

$$T_i = T_i^{(o)} + \Delta T_i \qquad (3.54b)$$

$$F_i = F_i^{(o)} + \Delta F_i \qquad (3.54c)$$

The stress tensor $\sigma_{ij}$ is the Kirchoff stress, which is referred to a

unit of area <u>before</u> the addition of the incremental loads for step N ("undeformed" area), but are with respect to the current (convected) axes $x_i$ (Ref. 54). Likewise, $T_i$ and $F_i$ are referred to "undeformed" area and convected axes.

From Ref. 53, the principle of virtual work is

$$\int_v \sigma_{ij} \, \delta E_{ij} \, dV = \int_s T_i \, \delta u_i \, dS + \int_v F_i \, \delta u_i \, dV \quad (3.55a)$$

For the initial stress problem, Eq. (3.55a) becomes, for incremental load step N,

$$\int_v (\sigma_{ij}^{(o)} + \Delta\sigma_{ij}) \, \delta(\Delta E_{ij}) \, dV$$

$$= \int_s (T_i^{(o)} + \Delta T_i) \, \delta(\Delta u_i) \, dS$$

$$+ \int_v (F_i^{(o)} + \Delta F_i) \, \delta(\Delta u_i) \, dV \quad (3.55b)$$

where $\Delta E_{ij}$ is the incremental Green's strain tensor, and all integrals are referred to the "undeformed" volume of the element. The strain tensor can be written as

$$\Delta E_{ij} = \frac{1}{2}(\Delta u_{i,j} + \Delta u_{j,i} + \Delta u_{k,i} \, \Delta u_{k,j}) \quad (3.56)$$

Substituting Eq. (3.56) in (3.55b) gives

$$\int_v (\sigma_{ij}^{(o)} + \Delta\sigma_{ij})(\delta_{ki} + \Delta u_{k,i}) \delta\Delta u_{k,j} \, dV$$

$$(3.57)$$

$$= \int_s (T_i^{(o)} + \Delta T_i) \delta\Delta u_i \, dS + \int_v (F_i^{(o)} + \Delta F_i) \delta\Delta u_i \, dV$$

where $\delta_{ki}$ is the Kronecker Delta function.

Rearranging Eq. (3.57) leads to

$$\int_V (\sigma_{ij}^{(o)} \Delta u_{k,i} \, \delta\Delta u_{k,j} + \Delta\sigma_{ij} \, \delta\Delta u_{i,j}$$

$$+ \Delta\sigma_{ij} \Delta u_{k,i} \, \delta\Delta u_{k,j}) \, dV = \int_V \Delta F_i \, \delta\Delta u_i \, dV \qquad (3.58)$$

$$+ \int_S \Delta T_i \, \delta\Delta u_i \, dS + \int_V (F_i^{(o)} \delta\Delta u_i - \sigma_{ij}^{(o)} \delta\Delta u_{i,j}) dV + \int_S T_i^{(o)} \delta\Delta u_i dS$$

The incremental constitutive law in Lagrangian variables is (Ref. 54)

$$\Delta\sigma_{ij} = C_{ijk\ell} \Delta E_{k\ell} \qquad (3.59)$$

where $C_{ijk\ell}$ may include the effect of past loading history, as in elastic-plastic problems. Various forms of the constitutive law are considered in more detail in a later section. Using Eq. (3.59) in (3.57) and neglecting high order terms gives

$$\int_V (\sigma_{ij}^{(o)} \Delta u_{k,i} \, \delta\Delta u_{k,j} + C_{ijk\ell} \Delta u_{k,\ell} \, \delta\Delta u_{i,j}) dV$$

$$= \int_V \Delta F_i \, \delta\Delta u_i \, dV + \int_S \Delta T_i \, \delta\Delta u_i \, dS + \int_V (F_i^{(o)} \delta\Delta u_i - \sigma_{ij}^{(o)} \delta\Delta u_{i,j}) dV$$

$$+ \int_S T_i^{(o)} \delta\Delta u_i dS \qquad (3.60)$$

If it is now assumed that the initial stress state, denoted by $\sigma_{ij}^{(o)}$, $T_i^{(o)}$ and $F_i^{(o)}$, is in equilibrium prior to the addition of the incremental loads for step N, then the last three integrals in Equation (3.60) vanish, and the formulation similar to that of Ref. 39 results. However, due to the numerical incremental solution technique for solving

a large strain problem, the initial stress state may _not_ be in equilibrium before load step N.  As will be shown in a later  section, it is possible to derive an equilibrium error check if these terms are retained.

Note that the _total_ stresses $\sigma_{ij}$ resulting from load step N become _initial_ stresses for step (N+1).  For step N, these stresses are referred to a unit of undeformed area, and current axes $x_i$.  However, for step (N + 1), these stresses must be referred to deformed area and the initial axes $X_i$.  The relation between Kirchoff stress tensor $\sigma_{ij}$ and the Eulerian stress tensor $\sigma_{ij}^{(o)}$ is (Ref. 54)

$$\sigma_{ij} = \left| \frac{\partial x}{\partial X} \right| \sigma_{k\ell}^{(o)} \frac{\partial X_i}{\partial x_k} \frac{\partial X_j}{\partial x_\ell} \qquad (3.61)$$

where $\left| \partial x/\partial X \right|$ is the determinant of the matrix $\left[ \partial x_i/\partial X_j \right]$.  Neglecting higher order terms, the inverse transform of Eq. (3.61)   gives

$$\sigma_{ij}^{(o)} = \left| \frac{\partial x}{\partial X} \right|^{-1} \sigma_{k\ell} \frac{\partial x_i}{\partial X_k} \frac{\partial x_j}{\partial X_\ell} \qquad (3.62)$$

as the desired transformation.  From Equation  (3.53),

$$\frac{\partial x_i}{\partial X_k} = \delta_{ik} + \Delta u_{i,k} \qquad (3.63)$$

gives the derivatives of Eq. (3.62), and

$$\left| \frac{\partial x}{\partial X} \right|^{-1} \cong (1 - \Delta u_{1,1} - \Delta u_{2,2} - \Delta u_{3,3}) \qquad (3.64)$$

the scaling factor.  Using Eq. (3.63) and (3.64) in (3.62) and neglecting higher order terms gives

$$\sigma_{ij}^{(o)} = (1 - \Delta \varepsilon_{kk}) \sigma_{ij} + \sigma_{ik} \Delta u_{j,k} + \sigma_{jk} \Delta u_{i,k} \qquad (3.65)$$

Likewise, the surface tractions transform as

$$T_i^{(o)} = (1 - \Delta\varepsilon_{kk})T_k(\delta_{ik} + \Delta u_{i,k}). \tag{3.66}$$

### III.5.3 Alternate Variational Statements

It is instructive to consider the way in which the present formulation differs from those of other investigators (Refs. 38,40,55). Oden (Ref. 55) uses the original undeformed structure in constructing an incremental virtual work statement. Therefore, the strains and displacements in Equation (3.55a) are <u>total</u> strains and displacements.

Since the undeformed body is taken as the reference state, the forces, stresses, <u>and</u> displacements can be written as

$$\sigma_{ij} = \sigma_{ij}^{(o)} + \Delta\sigma_{ij} \tag{3.67a}$$

$$T_i = T_i^{(o)} + \Delta T_i \tag{3.67b}$$

$$F_i = F_i^{(o)} + \Delta F_i \tag{3.67c}$$

$$u_i = u_i^{(o)} + \Delta u_i \tag{3.67d}$$

where $u_i^{(o)}$ is the initial displacement prior to the current incremental step. Using Equations (3.67) in (3.55a), neglecting higher order terms, and assuming the initial stress state is in equilibrium gives

$$\int_v (\sigma_{ij}^{(o)} \Delta u_{k,i} \, \delta u_{k,j} + \Delta\sigma_{ij}\delta\Delta u_{i,j} + \Delta\sigma_{ij}u_{k,i}^{(o)}\delta\Delta u_{k,j})dV$$

$$= \int_v \Delta F_i\delta\Delta u_i dV + \int_s \Delta T_i\delta\Delta u_i dS \tag{3.68}$$

Furthermore, using the constitutive law, Equation (3.59), and the surface traction transformation, Equation (3.67), and again neglecting higher order terms, gives

$$\int_V (\sigma_{ij}^{(o)} \Delta u_{k,i} \delta \Delta u_{k,j} + C_{ijk\ell} \Delta u_{k,\ell} \delta \Delta u_{i,j}$$

$$+ C_{ijk\ell} \Delta u_{k,\ell} u_{n,i}^{(o)} \delta \Delta u_{n,j} + T_k^{(o)} \Delta u_{i,k} \delta \Delta u_i) dV \qquad (3.69)$$

$$= \int_S \Delta T_i (\delta_{ik} + u_{k,i}^{(o)}) \delta \Delta u_k dS + \int_V \Delta F_i \delta \Delta u_i dV$$

Note the presence of the initial displacements $u_i^{(o)}$ in Equation (3.69). These are not necessary in the incremental virtual work statement of Equation (3.60) due to the selection of a different frame of reference.

Mallett and Marcal (Ref. 34) start their formulation with equation (3.55a) but do not neglect higher order terms after the strain-displacement and stress-strain relations have been substituted into the virtual work statement. This gives

$$\int_V (C_{ijk\ell} u_{k,} \delta u_{i,j} + C_{ijk\ell} u_{n,k} \delta(u_{i,j} u_{n,\ell})$$

$$+ C_{ijk\ell} u_{m,k} u_{m,\ell} u_{n,j} \delta u_{n,i}) dV = \int_S T_i \delta u_i dS + \int_V F_i \delta u_i dV$$

$$(3.70)$$

In a later section, it will be shown how the various virtual work statements lead to different finite element formulations.

III.5.4  Constitutive Law

In this section, the constitutive law used for the work reported herein will be considered. Equation (3.59) gives the general form which will be specialized for elastic and elasto-plastic problems. For planar problem, the stresses and strains will be arranged in a vector as

$$\sigma_{ij} = \{\sigma_{11} \sigma_{22} \sigma_{33} \sigma_{12}\} = \{\sigma\} \qquad (3.71a)$$

$$E_{ij} = \{E_{11} E_{22} E_{33} 2E_{12}\} = \{E\} \qquad (3.71b)$$

It should be noted that for plane stress, $\sigma_{33} = 0$, and for plane strain, $E_{33} = 0$. In matrix form (which is more convenient for the following development), the stress-strain law becomes

$$\{\sigma\} = [C]\{E\} \tag{3.72}$$

where $[C]$ is a 4 x 4 matrix containing the $C_{ijk\ell}$.

### III.5.4.1 Elastic Behavior

For plane stress, the $[C]$ matrix is

$$[C] = \frac{E}{(1-\mu^2)} \begin{bmatrix} 1 & \mu & 0 & 0 \\ \mu & 1 & 0 & 0 \\ 0 & 0 & 0 & 0 \\ 0 & 0 & 0 & \frac{1}{2}(1-\mu) \end{bmatrix} \equiv [C_e] \tag{3.73}$$

where $E$ is the elastic modulus, and $\mu$ is Poisson's Ratio. For plane strain and axisymmetric stress analysis,

$$[C] = \frac{E}{(1+\mu)(1-2\mu)} \begin{bmatrix} (1-\mu) & \mu & \mu & 0 \\ \mu & (1-\mu) & \mu & 0 \\ \mu & \mu & (1-\mu) & 0 \\ 0 & 0 & 0 & \frac{1}{2}(1-2\mu) \end{bmatrix} \equiv [C_e] \tag{3.74}$$

In the following development, the matrix $[C_e]$ will be referred to as the elasticity matrix.

### III.5.4.2 Elasto-Plastic Behavior

For elasto-plastic problems, the strains can be considered as being composed of elastic portion, $\{E_e\}$, and a plastic portion, $\{E_p\}$. The total incremental strain is then

$$\{dE\} = \{dE_e\} + \{dE_p\} \tag{3.75}$$

where "d" indicates differential. With this definition, Equation (3.72) becomes

$$\{d\sigma\} = [C_e]\{dE_e\} \tag{3.76a}$$

or, using Equation (3.75),

$$\{d\sigma\} = [C_e] \, (\{dE\} - \{dE_p\}) \qquad (3.76b)$$

In order to relate stresses to <u>total</u> strains, the plastic strains in Equation (3.76b) must be expressed in terms of total strains. This is considered in the following section.

The flow rule of plasticity states (Ref. 51)

$$\{dE_p\} = \frac{3}{2\bar{\sigma}} \frac{d\bar{\sigma}}{H'} \{S\} \qquad (3.77)$$

where

$$S_{ij} = \sigma_{ij} - \frac{1}{3}\sigma_{kk} \qquad (3.78a)$$

are the devatoric stresses, arranged as

$$\{S\} = \{S_{11} \ S_{22} \ S_{33} \ 2S_{12}\} \qquad (3.78b)$$

and H' is the slope of the equivalent stress (denoted by $\bar{\sigma}$)-equivalent strain ($\bar{e}_p$) curve

$$d\bar{\sigma} = H' \, d\bar{e}_p \qquad (3.78c)$$

The Von Mises Yield Criterion gives

$$2\bar{\sigma}^2 = (\sigma_{11} - \sigma_{22})^2 + (\sigma_{22} - \sigma_{33})^2 + (\sigma_{11} - \sigma_{33})^2 \qquad (3.79)$$
$$+ 6 \, \sigma_{12}^2$$

for two-dimensional problems. Differentiating Equation (3.79) implicitly leads to

$$d\bar{\sigma} = \frac{3}{2\bar{\sigma}} \{S\}^T \{d\sigma\} \qquad (3.80a)$$

Combining Equations (3.76b), (3.77) and (3.80a) eventually leads to

$$\{d\sigma\} = [C_e] \; ([I] - [\Omega]) \; \{dE\} \qquad (3.81a)$$

where

$$[\Omega] = \frac{\{S\} \{S\}^T [C_e]}{(\frac{2\bar{\sigma}}{3})^2 H' + \{S\}^T [C_e] \{S\}} \qquad (3.81b)$$

is the plasticity matrix. For plane strain and axisymmetric stress analysis,

$$[C_e][\Omega] = \beta \begin{bmatrix} S_{11}^2 & S_{11}S_{22} & S_{11}S_{33} & S_{11}S_{12} \\[2mm] & S_{22}^2 & S_{22}S_{33} & S_{22}S_{12} \\[2mm] & & S_{33}^2 & S_{33}S_{12} \\[2mm] \text{SYM.} & & & S_{12}^2 \end{bmatrix} \qquad (3.82a)$$

where

$$\beta = \frac{3E}{2\bar{\sigma}^2 (1+\mu)[1+\frac{2(1+\mu)}{3}\frac{H'}{E}]} \qquad (3.82b)$$

For plane stress

$$[C_e][\Omega] = \beta \begin{bmatrix} (S_{11}+\mu S_{22})^2 & (S_{11}+\mu S_{22})(S_{22}+\mu S_{11}) & 0 & (1-\mu)S_{12}(S_{11}+\mu S_{22}) \\[2mm] & (S_{22}+\mu S_{11})^2 & 0 & (1-\mu)S_{12}(S_{22}+\mu S_{11}) \\[2mm] & & 0 & 0 \\[2mm] \text{SYM.} & & 0 & (1-\mu)^2 S_{12}^2 \end{bmatrix} \qquad (3.83a)$$

3-29

where

$$\frac{1}{\beta} = \frac{(1-\mu^2)}{E} \left[ \frac{4}{9} \bar{\sigma}^2 (1-\mu^2) \frac{H'}{E} + \frac{5-4\mu}{9} (\sigma_{11}^2 + \sigma_{22}^2) \right.$$

$$\left. + \frac{10\mu-8}{9} \sigma_{11} \sigma_{22} + 2(1-\mu)\sigma_{12}^2 \right] \tag{3.83b}$$

Note that in both of the above cases, $\beta = 0$ if the structure is loading or unloading elastically.

The quantity $H'$ can be decuced from a simple uniaxial tensile test as follows. Figure 3-3 shows a bi-linear uniaxial stress-strain curve,
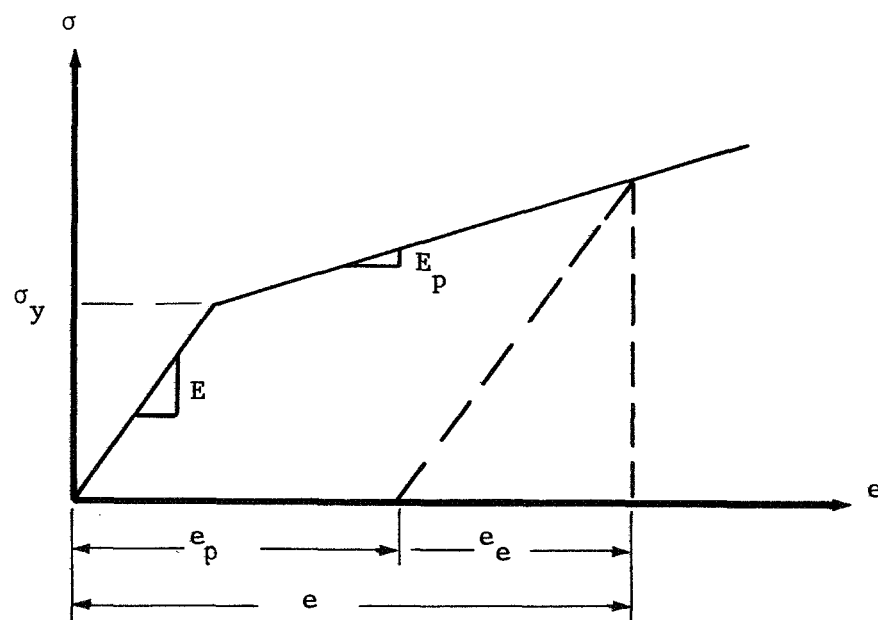


Figure 3-3. Uniaxial Test

where $\sigma_y$ denotes the yield stress, $E_p$ the post-yield modulus, and e the strain. From Figure 3-3,

$$e_p = \left( \frac{1}{E_p} - \frac{1}{E} \right) (\sigma - \sigma_y) \tag{3.84}$$

Rearranging this gives

$$\sigma = \frac{EE_p}{E-E_p} e_p + \sigma_y \qquad (3.85a)$$

or, incrementally

$$d\sigma = \frac{EE_p}{E-E_p} de_p \qquad (3.85b)$$

Comparing Equation (3.78c) with (3.85b) shows

$$\frac{H'}{E} = \frac{E_p}{E-E_p} \qquad (3.86)$$

The work reported herein assumes that the material behavior can be approximated by a bi-linear model such as that shown in Figure 3-3. For this model, the behavior can be completely determined by the quantities $E$, $\mu$, $E_p$, and $\sigma_y$.

In summary, the $C_{ijk\ell}$ for elastic problems are given by the matrix terms of Equations (3.73) and (3.74), and for elasto-plastic problems by Equations (3.81), (3.82), and (3.83). Due to the incremental nature of the formulation, many other types of constitutive relations, such as for viscoelasticity, nonlinear elasticity, etc., could be considered.

III.5.5   Finite Element Formulation

The incremental finite element displacement equilibrium equations can be derived from the virtual work statement, Equation (3.60), by interpolation or node point displacements as

$$\Delta u_k = \emptyset_{ik} \Delta r_i \qquad (3.87)$$

where $\emptyset_{ik}$ are the interpolation (or shape) functions, and $\Delta r_i$ is an incremental node point displacement. The interpolating functions should satisfy certain requirements (Ref. 43) if the numerical solution is to represent an upper bound to the true solution. Substituting Equation (3.87) in (3.60), and assuming the variations $\delta \Delta r_i$ are arbitrary, gives

$$(k_{ij}^{(G)} + k_{ij}) \, \Delta r_j = \Delta f_i + \varepsilon_i \qquad (3.88a)$$

for each element, where

$$k_{ij}^{(G)} = \int_V \phi_{in,k} \sigma_{k\ell}^{(o)} \phi_{jn,\ell} dV \qquad (3.88b)$$

$$k_{ij} = \int_V \phi_{ik,\ell} \, C_{k\ell mn} \, \phi_{jm,n} \, dV \qquad (3.88c)$$

$$\Delta f_i = \int_S \Delta T_k \, \phi_{ik} \, dS + \int_V \Delta F_k \, \phi_{ik} \, dV \qquad (3.88d)$$

$$\varepsilon_i = \int_S T_k^{(o)} \phi_{ik} \, dS + \int_V (F_k^{(o)} \phi_{ik} - \sigma_{k\ell}^{(o)} \phi_{ik,\ell}) dV \qquad (3.88e)$$

The terms given in Equation (3.88b) form the incremental geometric stiffness matrix, and the terms of Equation (3.88c) gives the conventional incremental stiffness matrix. The incremental loading vector is composed of the terms of Equation (3.88d). The components of Equation (3.88e) are referred to herein as _residuals_, since they represent the error left over from the previous loading history. Due to the approximations introduced by the linear incremental solution procedure, these residuals will not, in general, be zero.

Once an element type and shape functions have been chosen, and a material law considered, the integrals of Equations (3.88) can be evaluated, usually in closed form. Then Equation (3.88a) becomes

$$([k^{(G)}] + [k])_N \, \{\Delta r\}_N = \{\Delta f\}_N + \{\varepsilon\}_N \qquad (3.89)$$

for load step N. If the finite element _shape_ changes during the incremental loading process prior to step N, then some approximations are introduced in the integrations for step N. This is the case for large strain problems in which so-called refined elements are used. However, if the element size is kept small in the regions of high strain, the approximation introduced should be accurate.

Next, Equation (3.89) can be evaluated for each discrete element, and by considering inter-element compatibility and boundary conditions, these can be assembled into a system of linear incremental equilibrium equations for the entire structure,

$$([K^{(G)}] + [K])_N \{\Delta R\}_N = \{\Delta F\}_N + \{ER\}_N \qquad (3.90)$$

For load step N, these equations can be easily solved for $\{\Delta R\}_N$, the nodal point displacements.

III.5.6  Solution Procedure

The linear incremental solution technique for nonlinear structural response problems proceeds as follows. For the first step, the terms of Equation (3.90) are

$$\{ER\}_1 = \{0\} \qquad (3.91a)$$

and since there are no initial stresses,

$$[K^{(G)}]_1 = [0] \qquad (3.91\ b)$$

then the linear problem

$$[K]_1 \{\Delta R\}_1 = \{\Delta F\}_1 \qquad (3.91c)$$

is solved. After this first step, and after each succeeding step, nodal point coordinates are updated, and total displacements, strains and stresses are computed by adding all incremental contributions. The total stresses at the end of step N, $\sigma_{ij}$, must be transformed to $\sigma_{ij}(o)$, initial stresses for step (N + 1), by using the transformation of Equation (3.65). Note that in this type of procedure, the stiffness matrices $[K^{(G)}]_N$ and $[K]_N$ are recomputed for each load step, as indicated by the subscript N. This is due to the fact that both stresses (which effect the geometric stiffness matrix) and the stress-strain law (which effects the conventional stiffness matrix) change during the incremental solution process. For loadings which "follow" the structure, such as normal pressures, the load vector must also be updated for each step.

The step-by-step procedure is shown graphically in Figure 3-4, in which R is some measure of deflection, and F a measure of applied force. Initially, $\Delta F_1$ is applied to the structure, with $ER_1 = 0$ (no initial unbalance), and the response $R_1 = \Delta R_1$ computed from Equation (3.90). Note that, in general, $R_1 \neq R_1^{(T)}$, where the superscript "T" denotes <u>true</u> solution. Next, the residual $ER_2$, i.e., the error associated with the <u>first</u> incremental step, is computed, after updating displacements, strains and stresses. This quantity can be used to check the accuracy of the incremental procedure, since it represents the unbalance in nodal point equilibrium introduced by the linearizing assumptions in the present theory. For the second incremental step, the load $(\Delta F_2 + ER_2)$ is applied, giving eventually $R_2$. The process is continued in this manner.
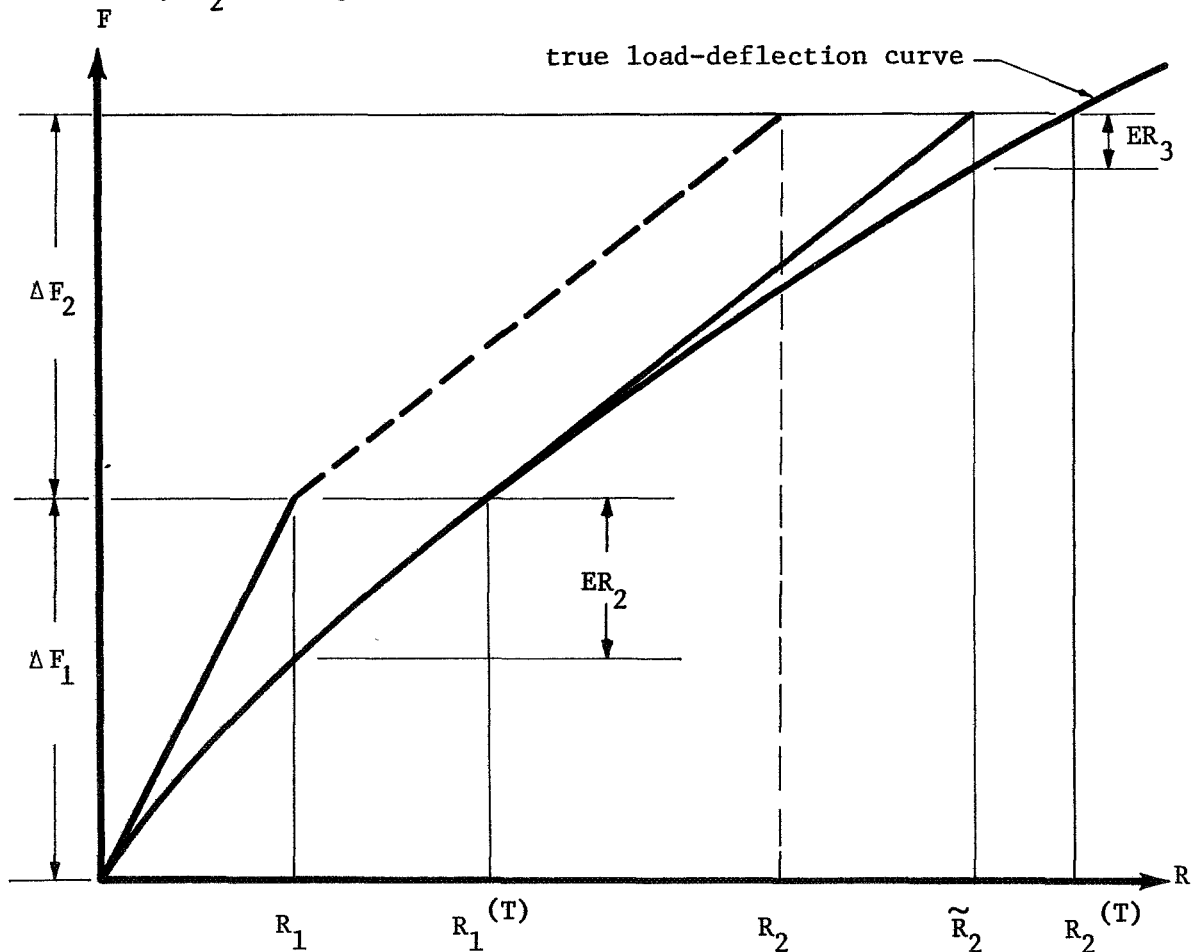


Figure 3-4. Incremental Solution Process

It is important to note how this method differs from the incremental procedures outlined by other investigators. First, an equilibrium check is automatically provided in the form of the residual vector $\{ER\}_N$. Below it is shown how this quantity can additionally be used to reduce the equilibrium unbalance. Also, the addition of the residual vector to the force vector, leads to displacements which are closer to the true values than would be obtained by using only the incremental force vector. This can be seen from the example of Figure 3-4. If just $\Delta F_2$ is added to the structure for step 2, instead of $(\Delta F_2 + ER_2)$, then $R_2$ would result, which is a poorer approximation to the true displacement than $\tilde{R}_2$. Therefore, the omission of the residual vector leads to a load-deflection curve considerably above the true curve, for structures which "soften" with increasing load.

If the structural response is highly nonlinear, even the above procedure will lead to computed results which are in error. For these types of problems, a Newton-Raphson iteration, which uses the residual vector, can be employed to reduce the error in nodal point equilibrium to any desired degree. The procedure is as follows. After $\{\Delta R\}_N$, $\{ER\}_N$, etc., have been computed for step N, all informaiton is updated. Then Equation (3.90) is reassembled and resolved using only $\{ER\}_N$ as a load vector. The resulting additional incremental deflections, strains and stresses are added to the previous values for step N. A new residual is computed, and the process is repeated. In fact, this iteration can be performed at constant load as often as desired. In the work reported herein, the ratio of the norms of the residual vector and total force vector

$$\epsilon = \left( \frac{\{ER\}^T \{ER\}}{\{F\}^T \{F\}} \right)^{1/2} \tag{3.92}$$

is used to control the iteration by specifying that the corrective cycling continue until $\epsilon$ is less than some small number. Note that this process is similar to a Newton-Raphson iteration, as can be seen from Figure 3-5. In this figure, the stiffness matrix computed for point 1 is used to predict $(\Delta R_N)_1$ as the response to $\Delta F_N$, as a first approximation to the displacement $\Delta R_N$. Next, the stiffness matrix for point 2 and the load of
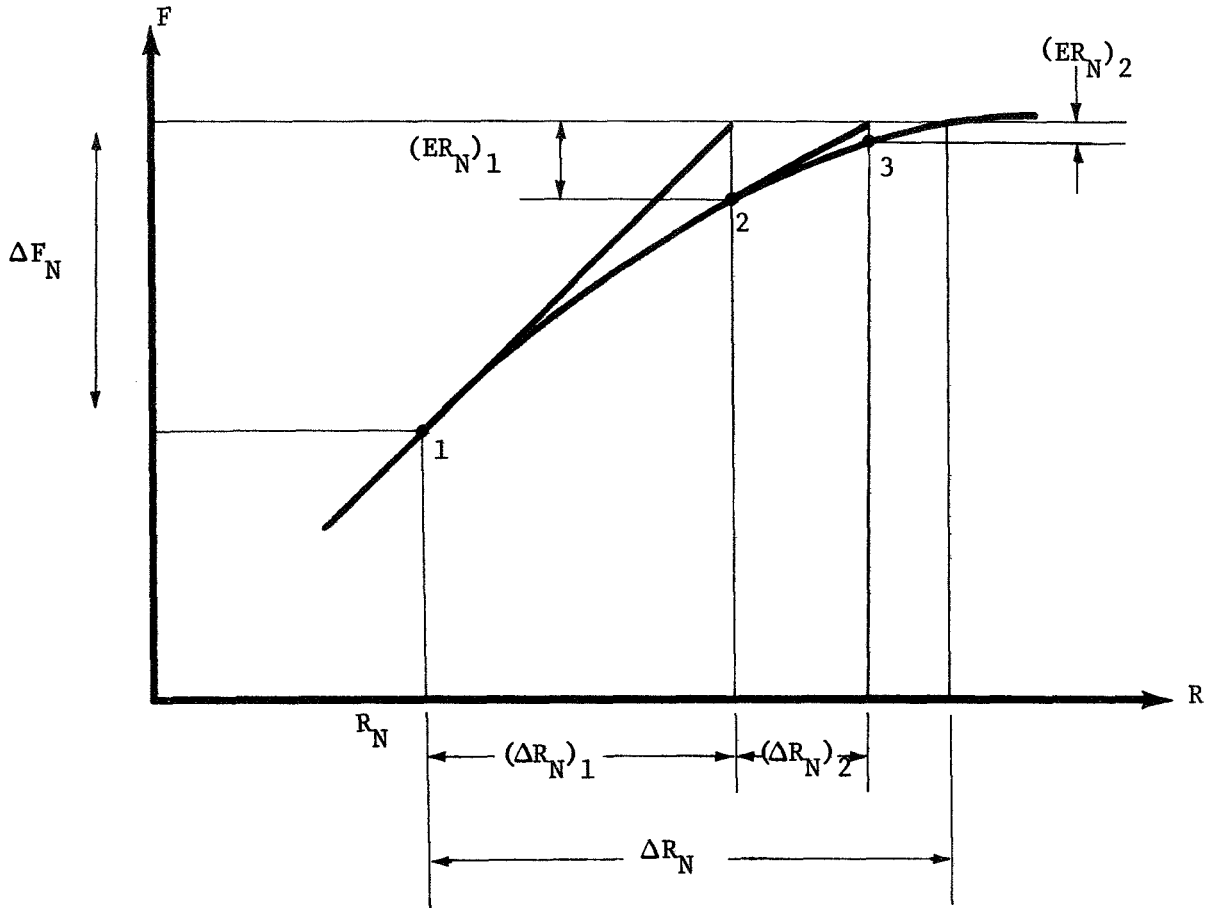
Figure 3-5. Corrective Iteration

$(ER)_1$ is used to compute $(\Delta R_N)_2$, giving $[(\Delta R_N)_1 + (\Delta R_N)_2]$ as the new approximation to $\Delta R_N$. Note that $(ER_N)_2$ is much smaller than $(ER_N)_1$, indicating the iteration is converging. After suitable accuracy has been achieved, the next load increment may be added to the structure.

III.5.7  Comparison with Other Methods

In this section, it will be shown how the alternate variational statements given in Section III.5.3 lead to different finite element formulations and solutions. By substituting Equation (3.87) in (3.69), the incremental equilibrium equation

$$(k_{ij}^{(G)} + k_{ij} + h_{ij} + r_{ij})\Delta r_i = \Delta q_i \qquad (3.93a)$$

is derived, in which $k_{ij}^{(G)}$ and $k_{ij}$ are given by Equations (3.88), and

$$h_{ij} = \int_V C_{k\ell mn} \, \phi_{jm,n} \, \phi_{qp,k} \, u_q^{(o)} \, \phi_{ip,\ell} \, dV \qquad (3.93b)$$

$$r_{ij} = \int_V T_k^{(o)} \, \phi_{jn,k} \phi_{in} \, dV \qquad (3.93c)$$

$$\Delta q_i = \int_V \Delta F_k \, \phi_{ik} \, dV + \int_S \Delta T_n (\delta_{nk} + \phi_{jk,n} \, u_j^{o)}) \phi_{ik} \, dS \qquad (3.93d)$$

In Equations (3.93), $h_{ij}$ is called the "initial displacement" matrix (Ref. 55), which is needed only if the motion is referred to some pre-selected fixed reference frame. Since the formulation given by Equation (3.88a) is referred to the current configuration, $h_{ij}$ is not necessary. The term $r_{ij}$ is the "initial load" matrix (Ref. 55) that arises due to changes in the loading surface caused by deformation. Again, Equation (3.88a) does not contain this term since the transformation of Equation (3.66) accomplishes the same effect. The incremental load is given by $\Delta q_i$. Note that no equilibrium check or correction is included in the formulation of Equation (3.93), and hence it is a Class I method. It should also be noted that the information for "updating" the coordinates, etc., is contained explicitly in this formulation, and therefore need not be done at the end of each load step as in the method presented herein (given by Equations (3.88)).

A different finite element formulation is achieved by using the interpolating functions in Equation (3.70). This gives

$$(k_{ij} + n_{ij}^{(1)} + n_{ij}^{(2)}) \, r_j = f_i \qquad (3.94a)$$

where $k_{ij}$ is given in Equation (3.88b), and

$$n_{ij}^{(1)} = 2 \int_V C_{k\ell mn} \, \phi_{qp,m} \, r_q \, \phi_{ip,n} \, \phi_{jk,\ell} \, dV \qquad (3.94b)$$

$$n_{ij}^{(2)} = \int_V C_{k\ell mn} \, \phi_{tq,m} \, r_t \, \phi_{sp,k} \, r_s \, \phi_{jq,n} \, \phi_{ip,\ell} \, dV \qquad (3.94c)$$

$$f_i = \int_S T_k \, \phi_{ki} \, kS + \int_V F_k \, \phi_{ki} \, dV \qquad (3.94d)$$

Note that this is a total, rather than incremental formulation, and that the matrix components $n_{ij}^{(1)}$ and $n_{ij}^{(2)}$ are linear and quadratic functions, respectively, of the unknown nodal point displacements. Reference 34 derives a linear incremental formulation from Equation (3.94a) as follows:

$$(k_{ij} + n_{ij}^{(1)} + n_{ij}^{(2)})\big|_{r_j} \, \Delta r_j = \Delta f_i \qquad (3.95)$$

where the $n_{ij}^{(1)}$ and $n_{ij}^{(2)}$ terms are evaluated at the known *previous* solution, $r_j$, of the incremental loading process. This is a Class I solution procedure. A Class II method is used in Ref. 42 by first writing the potential energy from Equation (3,94a) as

$$\pi = r_i (k_{ij} + n_{ij}^{(1)} + n_{ij}^{(2)})r_j - r_i f_i \qquad (3.96)$$

and then numerically minimizing this energy to find the unknown nodal point displacements.

The final alternative finite element formulation that will be reviewed herein is that of Ref. 56. In this work, the virtual work statement of Equation (3.57) is considered with the exceptions that, (1) the initial stresses are assumed to be in equilibrium, and (2) the stress transformation of Equation (13) is included explicitly in the virtual work expression. This is also a Class I approach.

In reviewing this past research on nonlinear structural analysis, it can be concluded that the new formulation presented herein has the following advantages:

(1) It can be used for problems with physical or material, or combined, nonlinearities;

(2) It checks and corrects for equilibrium at each incremental load step;

(3) It uses current coordinates.

In the next sections, details of the derivations of the various terms in Equation (3.88) will be presented for several types of finite elements, in order to eventually illustrate the present method.

### III.5.8  Linear Strain Triangle

A triangular finite element having six node points was used for the plane strain analysis reported herein. By interpolation on six nodal points, quadratic displacement variations, and corresponding linear strain variations, can be admitted within the element. Several alternative derivations of the stiffness matrices for this element will be presented, since each derivation has its advantages. The element and its displacement degrees-of-freedom are shown in Figure 3-6.
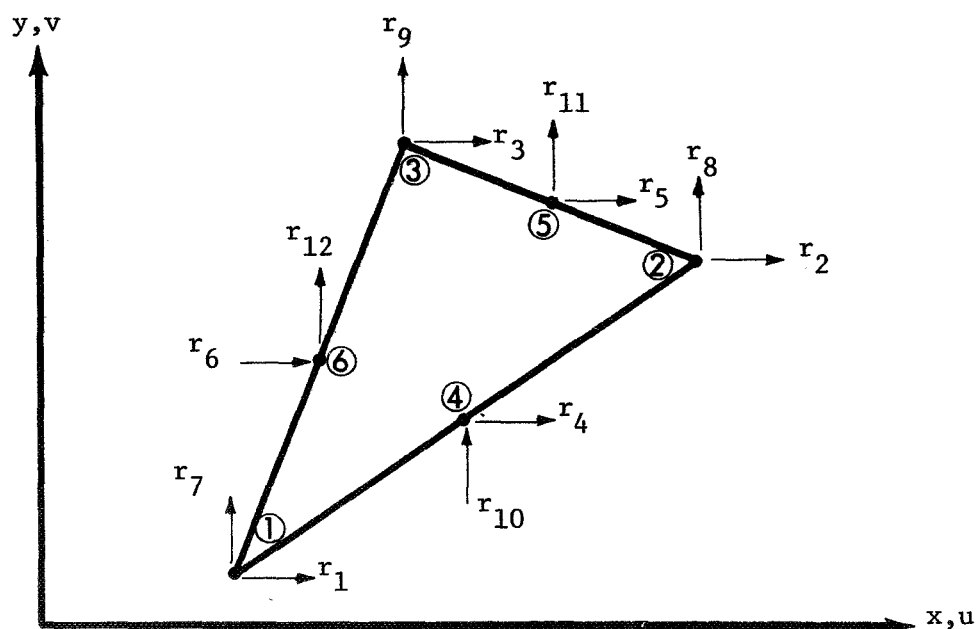


Figure 3-6.  Coordinates for LST

### III.5.8.1  Derivation Following Felippa (Ref. 39)

The elements $k_{ij}$ of Eq. (3.88a) can be derived very easily if the operations are carried out in "triangular coordinates" (Ref. 39). The triangular coordinates $\xi_1$, $\xi_2$, $\xi_3$ are defined in terms of node point coordinates $(x_i, y_i)$, for node $i = 1,2,3$, as

$$
\begin{Bmatrix} \xi_1 \\ \xi_2 \\ \xi_3 \end{Bmatrix} = \frac{1}{2A} \begin{bmatrix} (x_2 \, y_3 - x_3 \, y_2) & b_1 & a_1 \\ (x_3 \, y_1 - x_1 \, y_3) & b_2 & a_2 \\ (x_1 \, y_2 - x_2 \, y_1) & b_3 & a_3 \end{bmatrix} \begin{Bmatrix} 1 \\ x \\ y \end{Bmatrix} \qquad (3.97a)
$$

where

$$ b_1 = y_2 - y_3 \qquad\qquad b_2 = y_3 - y_1 \qquad\qquad b_3 = y_1 - y_2 $$

$$ a_1 = x_3 - x_2 \qquad\qquad a_2 = x_1 - x_3 \qquad\qquad a_3 = x_2 - x_1 \qquad (3.97b) $$

$$ 2A = a_1 \, b_2 - a_2 \, b_1 = a_1 \, b_3 - a_3 \, b_1 = a_2 \, b_3 - a_3 \, b_2 $$

The shape functions for a quadratic variation in displacements in terms of the triangular coordinates are

$$ \phi_{11} = \phi_{72} = \xi_1 \, (2\xi_1 - 1) \qquad\qquad \phi_{21} = \phi_{82} = \xi_2 \, (2\xi_2 - 1) $$

$$ \phi_{31} = \phi_{92} = \xi_3 \, (2\xi_3 - 1) \qquad\qquad \phi_{41} = \phi_{102} = 4\xi_1 \xi_2 $$

$$ \phi_{51} = \phi_{112} = 4\xi_2 \xi_3 \qquad\qquad\qquad \phi_{61} = \phi_{122} = 4\xi_1 \xi_3 $$

$$ \phi_{i1} = 0 \quad i = 7,8,\ldots,12 \qquad \phi_{j2} = 0 \quad j = 1,2,\ldots,6 \qquad (3.98) $$

where $r_1$ through $r_{12}$ (Fig. 3-6) are the displacements (the $\Delta$ notation has been dropped for brevity). These interpolation functions are consistent with Eq. (3.87), and thus can be used directly in Eqs. (3.88).

Substituting Eqs. (3.98) in (3.88c) and carrying out the indicated operations gives

$$ [k] = [B]^T [N][B] \qquad (12 \times 12) \qquad\qquad (3.99a) $$

where $k_{ij}$ is the i-th, j-th component of the conventional stiffness matrix $[k]$, and

where

$$[B] = \begin{bmatrix} [U] & \vdots & [0] \\ \overline{\phantom{xx}} & \dashv & \overline{\phantom{xx}} \\ [0] & \vdots & [V] \\ \overline{\phantom{xx}} & \neg & \overline{\phantom{xx}} \\ [V] & \vdots & [U] \end{bmatrix} \qquad (9 \times 12)$$  (3.99b)

is proportional to the transformation matrix from nodal strain coordinates to $\{r\}$ coordinates. In Equation (3.99b)

$$[U] = \begin{bmatrix} 3b_1 & -b_2 & -b_3 & 4b_2 & 0 & 4b_3 \\ -b_1 & 3b_2 & -b_3 & 4b_1 & 4b_3 & 0 \\ -b_1 & -b_2 & 3b_3 & 0 & 4b_2 & 4b_1 \end{bmatrix}$$  (3.99c)

$$[V] = \begin{bmatrix} 3a_1 & -a_2 & -a_3 & 4a_2 & 0 & 4a_3 \\ -a_1 & 3a_2 & -a_3 & 4a_1 & 4a_3 & 0 \\ -a_1 & -a_2 & 3a_3 & 0 & 4a_2 & 4a_1 \end{bmatrix}$$  (3.99d)

The elements of [N] are given by

$$[N] = \frac{h}{48A} \begin{bmatrix} [N_{11}] & [N_{12}] & [N_{13}] \\ & [N_{22}] & [N_{23}] \\ SYM & & [N_{33}] \end{bmatrix} \qquad (9 \times 9)$$  (3.99e)

and h is the elemental thickness.

For the elastic case, the elements of the $[N_{ij}]$ matrices of Equation (3.99e) are given by (no summation on i and j)

$$[N_{ij}] = \begin{bmatrix} 2C_{iijj} & C_{iijj} & C_{iijj} \\ & 2C_{iijj} & C_{iijj} \\ SYM. & & 2C_{iijj} \end{bmatrix}$$  (3.100a)

3-41

and $C_{iijj}$ are shown in Eq. (3.73), with the exception that row and column 3 of Eq. (3.73) are neglected, given

$$C_{3333} = \frac{E}{(1-\mu^2)} \; \frac{1}{2} \; (1-\mu) \tag{3.100b}$$

for use in Eq. (3.100a). For elasto-plastic analysis, to allow a more accurate representation of the actual bladder behavior, the material pro-perties were assumed to vary linearily inside the element. Then interpola-tion can be used in the volume integration for the element stiffness matrix as

$$[C] = \xi_1[C^{(1)}] + \xi_2[C^{(2)}] + \xi_3[C^{(3)}] \tag{3.101}$$

where the $\xi_i$ are interpolating functions and $[C^{(k)}]$ the stress-strain matrix at node k. After performing the integrations, the elements of $[N_{ij}]$ are

$$[N_{ij}] = 1/10 \begin{bmatrix} n_{11}^{ij} & n_{12}^{ij} & n_{13}^{ij} \\ & n_{22}^{ij} & n_{23}^{ij} \\ \text{sym} & & n_{33}^{ij} \end{bmatrix} \tag{3.102a}$$

and the $n_{k\ell}^{ij}$ are given by

$$n_{11}^{ij} = \{6 \quad 2 \quad 2\}\{C^{(k)}\}$$

$$n_{12}^{ij} = \{2 \quad 2 \quad 1\}\{C^{(k)}\}$$

$$n_{13}^{ij} = \{2 \quad 1 \quad 2\}\{C^{(k)}\}$$

$$n_{22}^{ij} = \{2 \quad 6 \quad 2\}\{C^{(k)}\}$$

$$n_{23}^{ij} = \{1 \quad 2 \quad 2\}\{C^{(k)}\}$$

$$n_{33}^{ij} = \{2 \quad 2 \quad 6\}\{C^{(k)}\}$$

(3.102b)

where

$$\left\{ C^{(k)} \right\}^T = \left\{ C^{(1)}_{iijj} \quad C^{(2)}_{iijj} \quad C^{(3)}_{iijj} \right\} \qquad (3.102c)$$

The individual components $C^{(k)}_{iijj}$ are given by $[C_e]([I] - [\Omega])$ of Eq. (3.81a), where the third row and column are omitted for brevity.

The geometric stiffness matrix $[k^{(G)}]$ can also be computed using the interpolating functions of Eq. (3.98) in Eq. (3.88b). For the case of a linear variation in strain and constant material properties over the element, the stresses also vary linearly. Therefore, to specify completely the stress state in an element, three nodal values of each stress component must be known. It is convenient to choose the stress values at the corner nodes and designate them as $\sigma_{x_i}$, $\sigma_{y_i}$, and $\tau_{xy_i}$ at node i, where i = 1,2,3. Then the stress components in Eq. (3.88b) for the geometric stiffness matrix can be written in terms of these nodal values as

$$\sigma_{11} = \left\{ \xi \right\}^T \left\{ \sigma_x \right\}$$

$$\sigma_{22} = \left\{ \xi \right\}^T \left\{ \sigma_y \right\} \qquad (3.103a)$$

$$\sigma_{12} = \left\{ \xi \right\}^T \left\{ \tau_{xy} \right\}$$

where

$$\left\{ \xi \right\}^T = \left\{ \xi_1 \quad \xi_2 \quad \xi_3 \right\}$$

$$\left\{ \sigma_x \right\}^T = \left\{ \sigma_{x_1} \quad \sigma_{x_2} \quad \sigma_{x_3} \right\}$$

$$\left\{ \sigma_y \right\}^T = \left\{ \sigma_{y_1} \quad \sigma_{y_2} \quad \sigma_{y_3} \right\} \qquad (3.103b)$$

$$\left\{ \tau_{xy} \right\}^T = \left\{ \tau_{xy_1} \quad \tau_{xy_2} \quad \tau_{xy_3} \right\}$$

Using Equations (3.103) and (3.98) in (3.88b) gives the geometric stiffness matrix as

$$[k^{(G)}] = \begin{bmatrix} [U]^T & [V]^T \\ \hline [U]^T & [V]^T \end{bmatrix} \begin{bmatrix} [J_x] & [J_{xy}] \\ \hline [J_{xy}] & [J_y] \end{bmatrix} \begin{bmatrix} [U] & [U] \\ \hline [V] & [V] \end{bmatrix} \qquad (3.104)$$

where

$$[J_i] = \frac{h}{240A} \left\{ \begin{bmatrix} 6 & 2 & 2 \\ 2 & 2 & 1 \\ 2 & 1 & 2 \end{bmatrix} \sigma_{i_1} + \begin{bmatrix} 2 & 2 & 1 \\ 2 & 6 & 2 \\ 1 & 2 & 2 \end{bmatrix} \sigma_{i_2} + \begin{bmatrix} 2 & 1 & 2 \\ 1 & 2 & 2 \\ 2 & 2 & 6 \end{bmatrix} \sigma_{i_3} \right\} \qquad (3.105)$$

for $i = x, y, xy$.

In the elasto-plastic case, both the strains and the material proper-
ties vary linearly over the element. Therefore, since the stresses are
a product of the material properties and the strains, they vary quadratic-
ally over the element. This must be taken into account when the geometric
stiffness matrix and the residual vector for each element are computed.
Equations (3.103a) must be redefined by changing its components as follows:

$$\{\xi\}^T = \{\xi_1(2\xi_1 - 1) \quad \xi_2(2\xi_2 - 1) \quad \xi_3(2\xi_3 - 1)$$

$$4\xi_1\xi_2 \quad 4\xi_2\xi_3 \quad 4\xi_3\xi_1\}$$

$$\{\sigma_x\}^T = \{\sigma_{x_1} \quad \sigma_{x_2} \quad \sigma_{x_3} \quad \sigma_{x_4} \quad \sigma_{x_5} \quad \sigma_{x_6}\}$$

$$\{\sigma_y\}^T = \{\sigma_{y_1} \quad \sigma_{y_2} \quad \sigma_{y_3} \quad \sigma_{y_4} \quad \sigma_{y_5} \quad \sigma_{y_6}\}$$

$$\{\tau_{xy}\}^T = \{\tau_{xy_1} \quad \tau_{xy_2} \quad \tau_{xy_3} \quad \tau_{xy_4} \quad \tau_{xy_5} \quad \tau_{xy_6}\}$$

where $\sigma_{x_i}$ is the stress in the x direction at node i, etc. Using Equations (3.106), Eq. (3.105) is replaced by

$$
[J_i] = \frac{Ah}{180} \left\{ \begin{bmatrix} 6 & 0 & 0 \\ 0 & -2 & -1 \\ 0 & -1 & -2 \end{bmatrix} \sigma_{i_1} + \begin{bmatrix} -2 & 0 & -1 \\ 0 & 6 & 0 \\ -1 & 0 & -2 \end{bmatrix} \sigma_{i_2} \right.
$$

$$
+ \begin{bmatrix} -2 & -1 & 0 \\ -1 & -2 & 0 \\ 0 & 0 & 6 \end{bmatrix} \sigma_{i_3} + \begin{bmatrix} 12 & 8 & 4 \\ 8 & 12 & 4 \\ 4 & 4 & 4 \end{bmatrix} \sigma_{i_4} \qquad (3.107)
$$

$$
\left. + \begin{bmatrix} 4 & 4 & 4 \\ 4 & 12 & 8 \\ 4 & 8 & 12 \end{bmatrix} \sigma_{i_5} + \begin{bmatrix} 12 & 4 & 8 \\ 4 & 4 & 4 \\ 8 & 4 & 12 \end{bmatrix} \sigma_{i_6} \right\} \quad i = x, y, xy
$$

The load vector for a uniform surface pressure increment $\Delta P_i$ on side i (the side _opposite_ node i) can be computed from Eq. (3.88d), giving

$$
\Delta f_1 = \frac{h}{6} (\Delta P_2 b_2 + \Delta P_3 b_3)
$$

$$
\Delta f_2 = \frac{h}{6} (\Delta P_1 b_1 + \Delta P_3 b_3)
$$

$$
\Delta f_3 = \frac{h}{6} (\Delta P_1 b_1 + \Delta P_2 b_2)
$$

$$
\Delta f_4 = \frac{4h}{6} \Delta P_3 b_3 \qquad\qquad (3.108)
$$

$$
\Delta f_5 = \frac{4h}{6} \Delta P_1 b_1
$$

$$
\Delta f_6 = \frac{4h}{6} \Delta P_2 b_2
$$

The last six elements of the incremental load vector, $\Delta f_7$ to $\Delta f_{12}$, can be computed from the first six, Eqs. (3.108), by replacing $b_i$ with $a_i$. The quantities $a_i$ and $b_i$ are given in Eq. (3.97b). The first part of the

residual vector, Eq. (3.88e), can be obtained from the above by substituting $P_i$, the initial pressure on side i, for $\Delta P_i$. The other part of the residual vector (neglecting body forces) can be computed using the shape functions, giving, for a quadratic stress variation,

$$\varepsilon_1 = \frac{h}{6} \, (P_2 b_2 + P_3 b_3) - \frac{h}{30} \, \{b_1 \; 0 \; 0\} [W_1] \{\sigma_x\}$$

$$- \frac{h}{30} \, \{a_1 \; 0 \; 0\} [W_1] \{\tau_{xy}\}$$

$$\varepsilon_2 = \frac{h}{6} \, (P_1 b_1 + P_3 \, b_3) - \frac{h}{30} \, \{0 \; b_2 \; 0\} [W_1] \{\sigma_x\}$$

$$- \frac{h}{30} \, \{0 \; a_2 \; 0\} [W_1] \{\tau_{xy}\}$$

$$\varepsilon_3 = \frac{h}{6} \, (P_1 b_1 + P_3 b_3) - \frac{h}{30} \, \{0 \; 0 \; b_3\} [W_1] \{\sigma_x\}$$

$$- \frac{h}{30} \, \{0 \; 0 \; a_3\} [W_1] \{\tau_{xy}\}$$

$$\varepsilon_4 = \frac{4h}{6} \, P_3 b_3 - \frac{h}{30} \, \{b_2 b_1 \; 0\} [W_2] \{\sigma_x\}$$

$$- \frac{h}{30} \, \{a_2 \; a_1 \; 0\} [W_2] \{\tau_{xy}\}$$

$$\varepsilon_5 = \frac{4h}{6} \, P_1 b_1 - \frac{h}{30} \, \{0 \; b_3 \; b_2\} [W_2] \{\sigma_x\}$$

$$- \frac{h}{30} \, \{0 \; a_3 \; a_2\} [W_2] \{\tau_{xy}\}$$

$$\varepsilon_6 = \frac{4h}{6} \, P_2 b_2 - \frac{h}{30} \, \{b_3 \; 0 \; b_2\} [W_2] \{\sigma_x\}$$

$$- \frac{h}{30} \, \{a_3 \; 0 \; a_1\} [W_2] \{\tau_{xy}\} \qquad (3.109)$$

where $\{\sigma_x\}$ and $\{\tau_{xy}\}$ are found in Eq. (3.106), and

$$[W_1] = \begin{bmatrix} 2 & -1 & -1 & 3 & -1 & 3 \\ -1 & 2 & -1 & 3 & 3 & -1 \\ -1 & -1 & 2 & -1 & 3 & 3 \end{bmatrix} \qquad (3.110a)$$

$$[W_2] = \begin{bmatrix} 2 & -1 & -1 & 8 & 4 & 8 \\ -1 & 2 & -1 & 8 & 8 & 4 \\ -1 & -1 & 2 & 4 & 8 & 8 \end{bmatrix} \qquad (3.110b)$$

The last six components of $\varepsilon_i$ can be derived from the first six, Eq. (3.109) by substituting $a_i$ for $b_i$, in the first term only, and $\{\tau_{xy}\}$ for $\{\sigma_x\}$, and $\{\sigma_y\}$ for $\{\tau_{xy}\}$, in the last two terms.

The formulation described above for plane strain nonlinear finite element analysis has been programmed. Some example problems and a detailed description of the code will be given in latter sections.

III.5.8.2  <u>Alternate Derivation - Linear Strain Triangle</u>

When the first load increment has been applied to a structure modeled by the triangular finite elements of Figure 3-6, the sides of each element will become curved.  Therefore, in subsequent increments, an undesirable error will be introduced into the analysis by assuming the sides of the elements remain straight.  For this reason, an alternate formulation of the linear strain triangle was considered which could be extended to a curved-sided triangular finite element.  This element could also be used to model structures whose sides are initially curved.  The derivation given below follows closely the work of Greenbaum (Reference 57), who used the procedure for axisymmetric stress analysis.

The displacements of the triangle of Figure 3-6 are assumed to be

$$
\left\{ \begin{array}{c} u(x,y) \\ \\ v(x,y) \end{array} \right\} = \left[ \begin{array}{cccccc|cccccc} 1 & x & y & x^2 & xy & y^2 & 0 & 0 & 0 & 0 & 0 & 0 \\ & & & & & & & & & & & \\ 0 & 0 & 0 & 0 & 0 & 0 & 1 & x & y & x^2 & xy & y^2 \end{array} \right] \left\{ \begin{array}{c} A_1 \\ \cdot \\ \cdot \\ \cdot \\ A_{12} \end{array} \right\}
$$

(3.111a)

or

$$
\left\{ V\ (x,y) \right\} = \left[ \phi\ (x,y) \right] \left\{ A \right\}
$$

(3.111b)

Evaluating Eq. (3.111a)  at the nodal point of the triangle gives

$$
\left\{ r \right\} = \left[ M \right] \left\{ A \right\}
$$

(3.112a)

or

$$
\begin{Bmatrix} r_1 \\ r_2 \\ r_3 \\ r_4 \\ r_5 \\ r_6 \\ r_7 \\ r_8 \\ r_9 \\ r_{10} \\ r_{11} \\ r_{12} \end{Bmatrix}
=
\begin{bmatrix}
1 & x_1 & y_1 & x_1^2 & x_1 y_1 & y_1^2 & 0 & 0 & 0 & 0 & 0 & 0 \\
1 & x_2 & y_2 & x_2^2 & x_2 y_2 & y_2^2 & 0 & 0 & 0 & 0 & 0 & 0 \\
1 & x_3 & y_3 & x_3^2 & x_3 y_3 & y_3^2 & 0 & 0 & 0 & 0 & 0 & 0 \\
1 & x_4 & y_4 & x_4^2 & x_4 y_4 & y_4^2 & 0 & 0 & 0 & 0 & 0 & 0 \\
1 & x_5 & y_5 & x_5^2 & x_5 y_5 & y_5^2 & 0 & 0 & 0 & 0 & 0 & 0 \\
1 & x_6 & y_6 & x_6^2 & x_6 y_6 & y_6^2 & 0 & 0 & 0 & 0 & 0 & 0 \\
0 & 0 & 0 & 0 & 0 & 0 & 1 & x_1 & y_1 & x_1^2 & x_1 y_1 & y_1^2 \\
0 & 0 & 0 & 0 & 0 & 0 & 1 & x_2 & y_2 & x_2^2 & x_2 y_2 & y_2^2 \\
0 & 0 & 0 & 0 & 0 & 0 & 1 & x_3 & y_3 & x_3^2 & x_3 y_3 & y_3^2 \\
0 & 0 & 0 & 0 & 0 & 0 & 1 & x_4 & y_4 & x_4^2 & x_4 y_4 & y_4^2 \\
0 & 0 & 0 & 0 & 0 & 0 & 1 & x_5 & y_5 & x_5^2 & x_5 y_5 & y_5^2 \\
0 & 0 & 0 & 0 & 0 & 0 & 1 & x_6 & y_6 & x_6^2 & x_6 y_6 & y_6^2
\end{bmatrix}
\begin{Bmatrix} A_1 \\ A_2 \\ A_3 \\ A_4 \\ A_5 \\ A_6 \\ A_7 \\ A_8 \\ A_9 \\ A_{10} \\ A_{11} \\ A_{12} \end{Bmatrix}
\qquad (3.112b)
$$

Inverting this gives

$$\{A\} = [M]^{-1}\{r\} \qquad (3.113)$$

By using Eq. (3.113) in (3.111b)

$$\{V(x,y)\} = [\phi(x,y)][M]^{-1}\{r\} = [\Phi]\{r\} \qquad (3.114)$$

The displacements in the element are obtained in terms of the nodal displacements $\{r\}$. Therefore, the terms of the matrix $[\Phi]$ are analogous to the interpolating functions given in Eq. (3.98).

The conventional stiffness matrix can be derived by considering the linear strain-displacement relationships

$$\epsilon_x = u,_x \quad \epsilon_y = v,_v \tag{3.115}$$

$$\gamma_{xy} = u,_x + v,_y$$

Using Eq. (3.114) in (3.115) gives the strains in terms of nodal displacements

$$\left\{ \epsilon(x,y) \right\} = [N(x,y)][M]^{-1}\{r\} \tag{3.116a}$$

where

$$\left\{ \epsilon(x,y) \right\}^T = \left\{ \epsilon_x \; \epsilon_y \; \gamma_{xy} \right\} \tag{3.116b}$$

$$[N(x,y)] = \begin{bmatrix} 0 & 1 & 0 & 2x & y & 0 & 0 & 0 & 0 & 0 & 0 & 0 \\ 0 & 0 & 0 & 0 & 0 & 0 & 0 & 0 & 1 & 0 & x & 2y \\ 0 & 0 & 1 & 0 & x & 2y & 0 & 1 & 0 & 2x & y & 0 \end{bmatrix} \tag{3.116c}$$

The stress-strain relation is

$$\left\{ \begin{array}{c} \sigma_x \\ \sigma_y \\ \tau_{xy} \end{array} \right\} = \begin{bmatrix} C_{11} & C_{12} & C_{13} \\ & C_{22} & C_{23} \\ SYM & & C_{33} \end{bmatrix} \left\{ \begin{array}{c} \epsilon_x \\ \epsilon_y \\ \gamma_{xy} \end{array} \right\} \tag{3.117a}$$

or

$$\left\{ \sigma \right\} = [C] \left\{ \epsilon(x,y) \right\} \tag{3.117b}$$

By virtual work, the stiffness matrix is

$$[k] = ([M]^{-1})^T [\kappa] [M]^{-1} \tag{3.118}$$

where the stiffness matrix in $\{A\}$ coordinates is

$$[\kappa] = \int_V [N(x,y)]^T [C][N(x,y)] \; dV \tag{3.119a}$$

and V is the volume of the element. The terms of the matrix inside the integral are given in Eq. (3.119b).

Let $$[K'] = [N(x,y)]^T [C] [N(x,y)] \quad (12 \times 12)$$

Then

$$K'_{1j} = 0 \quad j = 1,2,\ldots,12$$

$$K'_{22} = C_{11} \quad K'_{23} = C_{13} \quad K'_{24} = 2x\,C_{11} \quad K'_{25} = y\,C_{11} + x\,C_{13}$$

$$K'_{26} = 2y\,C_{13} \quad K'_{27} = 0 \quad K'_{28} = C_{13} \quad K'_{29} = C_{12}$$

$$K'_{210} = 2x\,C_{13} \quad K'_{211} = x\,C_{12} + y\,C_{13} \quad K'_{212} = 2y\,C_{12}$$

$$K'_{33} = C_{33} \quad K'_{34} = 2x\,C_{13} \quad K'_{35} = y\,C_{13} + x\,C_{33}$$

$$K'_{36} = 2y\,C_{33} \quad K'_{37} = 0 \quad K'_{38} = C_{33} \quad K'_{39} = C_{23}$$

$$K'_{310} = 2x\,C_{33} \quad K'_{311} = x\,C_{23} + y\,C_{33} \quad K'_{312} = 2y\,C_{23}$$

$$K'_{44} = 4x^2\,C_{11} \quad K'_{45} = 2\left(xy\,C_{11} + x^2\,C_{13}\right) \quad K'_{46} = 4xy\,C_{13}$$

$$K'_{47} = 0 \quad K'_{48} = 2x\,C_{13} \quad K'_{49} = 2x\,C_{12}$$

$$K'_{410} = 4x^2\,C_{13} \quad K'_{411} = 2\left(x^2\,C_{12} + xy\,C_{13}\right) \quad K'_{412} = 4xy\,C_{12}$$

$$K'_{55} = y^2\,C_{11} + x^2\,C_{33} + 2xy\,C_{13} \quad K'_{56} = 2\left(y^2\,C_{13} + xy\,C_{33}\right)$$

$$K'_{57} = 0 \quad K'_{58} = y\,C_{13} + x\,C_{33} \quad K'_{59} = y\,C_{12} + x\,C_{23}$$

$$K'_{510} = 2\left(xy\,C_{13} + x^2 C_{33}\right) \quad K'_{511} = y^2 C_{13} + x^2 C_{23} + xy\,C_{12} + xy\,C_{33}$$

$$K'_{512} = 2\left(y^2\,C_{12} + xy\,C_{23}\right)$$

$$K'_{66} = 4y^2\,C_{33} \quad K'_{67} = 0 \quad K'_{68} = 2y\,C_{33} \quad K'_{69} = 2y\,C_{23}$$

$$K'_{610} = 4xy\,C_{33} \quad K'_{611} = 2\left(xy\,C_{23} + y^2\,C_{33}\right) \quad K'_{612} = 4y^2\,C_{23}$$

$$K'_{7j} = 0 \quad j = 7,8,\ldots,12 \qquad\qquad\qquad (3.119b)$$

(continued)

$$K'_{88} = C_{33} \quad K'_{89} = C_{23} \quad K'_{810} = 2x\, C_{33}$$

$$K'_{811} = x\, C_{23} + y\, C_{33} \quad K'_{812} = 2y\, C_{23}$$

$$K'_{99} = C_{22} \quad K'_{910} = 2x\, C_{23} \quad K'_{911} = x\, C_{22} + y\, C_{23}$$

$$K'_{912} = 2y\, C_{22}$$

$$K'_{1010} = 4x^2\, C_{33} \quad K'_{1011} = 2\left(x^2 C_{23} + xy\, C_{33}\right) \quad K'_{1012} = 4xy\, C_{23}$$

$$K'_{1111} = x^2 C_{22} + y^2 C_{33} + 2xy\, C_{23} \quad K'_{1112} = 2\left(xy\, C_{22} + y^2 C_{23}\right)$$

$$K'_{1212} = 4y^2\, C_{22}$$

From Eq. (3.119b), only the following integrals need be evaluated:

$$V = \int_V dV \qquad \lambda_1 = \int_V x \ dV \qquad \lambda_2 = \int_V y \ dV$$

$$(3.120)$$

$$\lambda_3 = \int_V x^2 \ dV \qquad \lambda_4 = \int_V y^2 \ dV \qquad \lambda_5 = \int_V xy \ dV$$

By using a form of Green's Theorem (Reference 57) and $dV = h \ dx \ dy$, the above integrals can be transformed to

$$V = -h \oint_C y \ dx \qquad \lambda_1 = -h \oint_C xy \ dx \qquad \lambda_2 = -h \oint_C \frac{1}{2} y^2 \ dx$$

$$(3.121)$$

$$\lambda_3 = -h \oint_C x^2 y \ dx \qquad \lambda_4 = -h \oint_C \frac{1}{3} y^3 \ dx \qquad \lambda_5 = -h \oint_C \frac{1}{2} xy^2 \ dx$$

To illustrate how such integration can be performed, Eq. (3.121) will be evaluated for the case of a straight-sided triangular finite element, shown in Figure 3-7.
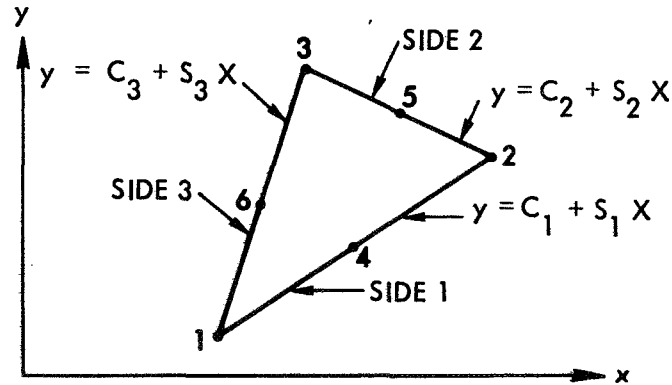


Figure 3-7 .  Evaluation of a Straight-Sided
Triangular Finite Element

The equation for side i is $y = c_i + s_i x$. Evaluating these equations at the corner points gives

$$y_1 = c_1 + s_1 x_1$$

$$y_2 = c_1 + s_1 x_2$$

$$y_2 = c_2 + s_2 x_2$$

$$y_3 = c_2 + s_2 x_3$$

$$y_3 = c_3 + s_3 x_3$$

$$y_1 = c_3 + s_3 x_1 \qquad (3.122)$$

Solving each pair of the above for the $c_i$ and $s_i$ gives

$$s_1 = \frac{y_2 - y_1}{x_2 - x_1} \qquad c_1 = y_1 - s_1 x_1 = \frac{x_2 y_1 - x_1 y_2}{x_2 - x_1}$$

$$s_2 = \frac{y_3 - y_2}{x_3 - x_2} \qquad c_2 = y_2 - s_2 x_2 = \frac{x_3 y_2 - x_2 y_3}{x_3 - x_2}$$

$$s_3 = \frac{y_1 - y_3}{x_1 - x_3} \qquad c_3 = y_3 - s_3 x_3 = \frac{x_1 y_3 - x_3 y_1}{x_1 - x_3} \qquad (3.123)$$

Using Eq. (3.123) in the first of Eq. (3.121) gives

$$V = -h \oint_c y \, dx = -h \int_1^2 y \, dx - h \int_2^3 y \, dx - h \int_3^1 y \, dx$$

or

$$-V = h \int_{x_1}^{x_2} (c_1 + s_1 x) \, dx + h \int_{x_2}^{x_3} (c_2 + s_2 x) \, dx + h \int_{x_3}^{x_1} (c_3 + s_3 x) \, dx$$

After carrying out the operations,

$$V = hA \qquad (3.124)$$

where A is given in Eq. (3.97b). Simarly, the other integrals are

$$\lambda_1 = \frac{1}{3} (x_1 + x_2 + x_3) \, hA$$

$$\lambda_2 = \frac{1}{3} (y_1 + y_2 + y_3) \, hA$$

$$\lambda_3 = \frac{1}{6} \left( x_1^2 + x_2^2 + x_3^2 + x_1 x_2 + x_1 x_3 + x_2 x_3 \right) hA$$

$$\lambda_4 = \frac{1}{6} \left( y_1^2 + y_2^2 + y_3^2 + y_1 y_2 + y_1 y_3 + y_2 y_3 \right) hA$$

$$\lambda_5 = \frac{1}{6} (x_1 y_1 + x_2 y_2 + x_3 y_3) \, hA + \frac{h}{12} \, [A_{21}(x_2 y_1 + x_1 y_2$$

$$-2x_3 y_3) + A_{32}(x_3 y_2 + x_2 y_3 - 2x_1 y_1) + A_{13}(x_1 y_1 + x_3 y_1 - 2x_2 y_2)]$$

with

$$A_{21} = \frac{1}{2} (x_1 y_2 - x_2 y_1)$$

$$A_{32} = \frac{1}{2} (x_2 y_3 - x_3 y_2)$$

$$A_{13} = \frac{1}{2} (x_3 y_1 - x_1 y_3) \qquad (3.125)$$

Using Eq. (3.125) in (3.119) and the result in (3.118) gives the conventional stiffness matrix.

The geometric stiffness matrix in $\{A\}$ coordinates can be derived by using Equation (3.58) giving

$$[\kappa_G] = \frac{1}{2} \int_V \left( \{u'\}^T [\tau] \{u'\} + \{u''\}^T [\tau] \{u''\} \right) dV \qquad (3.126)$$

where

$$\{u'\}^T = \{u_{1,1} \quad u_{1,2}\} = \{u_x \quad u_y\}$$

$$\{u''\}^T = \{u_{2,1} \quad u_{2,2}\} = \{v_x \quad v_y\}$$

$$[\tau] = \begin{bmatrix} \sigma_{11} & \sigma_{12} \\ \sigma_{12} & \sigma_{22} \end{bmatrix} \qquad (3.127)$$

From Equation (3.111a)

$$\{u'\} = [[M(x,y)] \mid [0]] \{A\}$$

$$\{u''\} = [[0] \mid [M(x,y)]] \{A\} \qquad (3.128)$$

where

$$[M(x,y)] = \begin{bmatrix} 0 & 1 & 0 & 2x & y & 0 \\ 0 & 0 & 1 & 0 & x & 2y \end{bmatrix} \qquad (3.129)$$

then

$$[k_G] = \int_V \left[ \begin{array}{c|c} [K_G'] & [0] \\ \hline [0] & [K_G'] \end{array} \right] dV \quad (12 \times 12) \qquad (3.130)$$

where

$$[K_G'] = [M(x,y)]^T [\tau] [M(x,y)] \quad (6 \times 6) \qquad (3.131a)$$

and the elements $K'_{Gij}$ are given in Eq. (3.131b).

$$K'_{G_{1j}} = 0 \quad j = 1,2,\ldots,6$$

$$K'_{G_{22}} = \tau_{11} \quad K'_{G_{23}} = \tau_{12} \quad K'_{G_{24}} = 2x\,\tau_{11}$$

$$K'_{G_{25}} = y\,\tau_{11} + x\,\tau_{12} \quad K'_{G_{26}} = 2y\,\tau_{12}$$

$$K'_{G_{33}} = \tau_{22} \quad K'_{G_{34}} = 2x\,\tau_{12} \quad K'_{G_{35}} = y\,\tau_{12} + x\,\tau_{22}$$

$$K'_{G_{36}} = 2y\,\tau_{22}$$

$$K'_{G_{44}} = 4x^2\,\tau_{11} \quad K'_{G_{45}} = 2\left(xy\,\tau_{11} + x^2\,\tau_{12}\right) \quad K'_{G_{46}} = 4xy\,\tau_{12}$$

$$K'_{G_{55}} = y^2\,\tau_{11} + 2xy\,\tau_{12} + x^2\,\tau_{22} \quad K'_{G_{56}} = 2\left(y^2\,\tau_{12} + xy\,\tau_{22}\right)$$

$$K'_{G_{66}} = 4y^2\,\tau_{22} \qquad (3.131b)$$

The geometric stiffness in r coordinates is then

$$[k^{(G)}] = ([M]^{-1})^T [K_G] [M]^{-1} \qquad (3.132)$$

The force vector for uniform pressure can similarly be computed. For example, for a uniform pressure on side 3 of Figure 3-7 of $(P_3 + \Delta P_3)$

$$\{\Delta R^{(1)}\} = ([M]^{-1})^T \{F\} \tag{3.133}$$

where

$$F_1 = h(P_3 + \Delta P_3)(y_1 - y_3)$$

$$F_2 = h(P_3 + \Delta P_3)(y_1 - y_3)(x_1 + x_3)/2$$

$$F_3 = h(P_3 + \Delta P_3)(y_1 - y_3)(y_1 + y_3)/2$$

$$F_4 = h(P_3 + \Delta P_3)(y_1 - y_3)(x_3^2 + x_3 x_1 + x_1^2)/3$$

$$F_5 = h(P_3 + \Delta P_3)(y_1 - y_3)(2y_1 x_1 + x_1 y_3 + 2y_3 x_3 + x_3 y_1)/6$$

$$F_6 = h(P_3 + \Delta P_3)(y_1 - y_3)(y_1^2 + y_1 y_3 + y_3^2)/3$$

$$F_7 = h(P_3 + \Delta P_3)(x_1 - x_3)$$

$$F_8 = h(P_3 + \Delta P_3)(x_1 - x_3)(x_1 + x_3)/2$$

$$F_9 = h(P_3 + \Delta P_3)(x_1 - x_3)(y_1 + y_3)/2$$

$$F_{10} = h(P_3 + \Delta P_3)(x_1^3 - x_3^3)/3$$

$$F_{11} = h(P_3 + \Delta P_3)(x_1 - x_3)(x_1 y_3 + 2x_1 y_1 + 2x_3 y_3 + x_3 y_1)/6$$

$$F_{12} = h(P_3 + \Delta P_3)(x_1 - x_3)(y_1^2 + y_1 y_3 + y_3^2)/3 \tag{3.134}$$

The expressions for pressure loadings on the other sides can be obtained by permuting the indices in Eq. (3.134) as follows

| Side | Index | Index |
|------|-------|-------|
| 1 | 1 | 2 |
| 2 | 2 | 3 |
| 3 | 3 | 1 |

The other portion of the load vector, that due to the unbalance of the initial stress field, can be deduced

$$\{\Delta R^{(2)}\} = - \left([M]^{-1}\right)^T \int_V [E(x,y)]^T [\sigma]\{\xi\} \, dV \tag{3.135}$$

3-57

where

$$[E(x,y)] = \begin{bmatrix} 0 & 1 & 0 & 2x & y & 0 & 0 & 0 & 0 & 0 & 0 & 0 \\ 0 & 0 & 1 & 0 & x & 2y & 0 & 1 & 0 & 2x & y & 0 \\ 0 & 0 & 0 & 0 & 0 & 0 & 0 & 0 & 1 & 0 & x & 2y \end{bmatrix}$$

$$[\sigma] = \begin{bmatrix} \sigma_{x_1} & \sigma_{x_2} & \sigma_{x_3} \\ \tau_{xy_1} & \tau_{xy_2} & \tau_{xy_3} \\ \sigma_{y_1} & \sigma_{y_2} & \sigma_{y_3} \end{bmatrix}$$

$$\{\xi\} = \begin{Bmatrix} \xi_1 \\ \xi_2 \\ \xi_3 \end{Bmatrix} = \frac{1}{2A} \begin{bmatrix} 2A_{32} & b_1 & a_1 \\ 2A_{13} & b_2 & a_2 \\ 2A_{21} & b_3 & a_3 \end{bmatrix} \begin{Bmatrix} 1 \\ x \\ y \end{Bmatrix} \qquad (3.136)$$

## III.5.8.3  Integrations for Curved Sides

All the above formulas would apply to an element with curved sides, as shown in Figure 3-8 except the integrations of Equation (3.125).
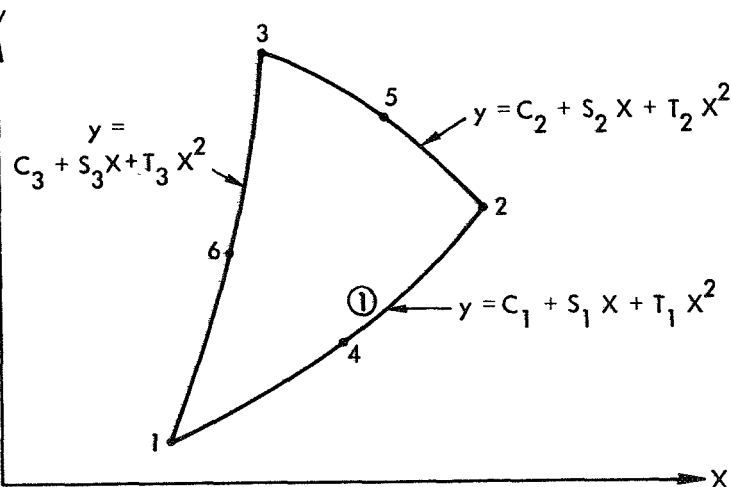


Figure 3-8.  Curved-Sided Element

To perform the volume integrations for a curved sided element, consider that the three points on side i determine a parabola

$$y = C_i + S_i x + T_i x^2 .$$
(3.137)

The constants can be found by evaluating this expression at the nodal points along side i. For example, for side 1,

$$y_1 = C_1 + S_1 x_1 + T_1 x_1^2$$

$$y_4 = C_1 + S_1 x_4 + T_1 x_4^2$$

$$y_2 = C_1 + S_1 x_2 + T_1 x_2^2$$
(3.138)

Inverting these relations gives

$$\begin{Bmatrix} C_1 \\ S_1 \\ T_1 \end{Bmatrix} = \frac{1}{(x_1 - x_4)(x_1 - x_2)(x_4 - x_2)}$$

$$\begin{bmatrix} x_2 x_4 (x_4 - x_2) & -x_1 x_2 (x_1 - x_2) & x_1 x_4 (x_1 - x_4) \\ x_2^2 - x_4^2 & x_1^2 - x_2^2 & x_4^2 - x_1^2 \\ (x_4 - x_2) & (x_2 - x_1) & (x_1 - x_4) \end{bmatrix} \begin{Bmatrix} y_1 \\ y_4 \\ y_2 \end{Bmatrix}$$
(3.139)

Eq. (3.141) lists all the necessary constants. These can then be used to derive closed-form expressions for the integrals of Eq. (3.119a) For example,

$$V = h\left[C_1(x_2 - x_1) + C_2(x_3 - x_2) + C_3(x_1 - x_3)\right.$$

$$+ \frac{1}{2} S_1\left(x_2^2 - x_1^2\right) + \frac{1}{2} S_2\left(x_3^2 - x_2^2\right) + \frac{1}{2} S_3\left(x_1^2 - x_3^2\right)$$

$$\left. + \frac{1}{3} T_1\left(x_2^3 - x_1^3\right) + \frac{1}{3} T_2\left(x_3^3 - x_2^3\right) + \frac{1}{3} T_3\left(x_1^3 - x_3^3\right)\right] \qquad (3.140)$$

The other integrals can similarly be evaluated.

$$C_1 = \frac{y_1\,x_2\,x_4(x_4-x_2) - y_4\,x_1\,x_2(x_1-x_2) + y_2\,x_1\,x_4(x_1-x_4)}{(x_1-x_4)(x_1-x_2)(x_4-x_2)}$$

$$S_1 = \frac{y_1\left(x_2^2-x_4^2\right) + y_4\left(x_1^2-x_2^2\right) + y_2\left(x_4^2-x_1^2\right)}{(x_1-x_4)(x_1-x_2)(x_4-x_2)}$$

$$T_1 = \frac{y_1(x_4-x_2) - y_4(x_1-x_2) + y_2(x_1-x_4)}{(x_1-x_4)(x_1-x_2)(x_4-x_2)}$$

$$C_2 = \frac{y_2\,x_3\,x_5(x_5-x_3) - y_5\,x_2\,x_3(x_2-x_3) + y_3\,x_2\,x_5(x_2-x_5)}{(x_2-x_5)(x_2-x_3)(x_5-x_3)}$$

$$S_2 = \frac{y_2\left(x_3^2-x_5^2\right) + y_5\left(x_2^2-x_3^2\right) + y_3\left(x_5^2-x_2^2\right)}{(x_2-x_5)(x_2-x_3)(x_5-x_3)}$$

$$T_2 = \frac{y_2(x_5-x_3) - y_5(x_2-x_3) + y_3(x_2-x_5)}{(x_2-x_5)(x_2-x_3)(x_5-x_3)}$$

$$C_3 = \frac{y_3\,x_1\,x_6(x_6-x_1) - y_6\,x_3\,x_1(x_3-x_1) + y_1\,x_3\,x_6(x_3-x_6)}{(x_3-x_6)(x_3-x_1)(x_6-x_1)}$$

$$S_3 = \frac{y_3\left(x_1^2-x_6^2\right) + y_6\left(x_3^2-x_1^2\right) + y_1\left(x_6^2-x_3^2\right)}{(x_3-x_6)(x_3-x_1)(x_6-x_1)}$$

$$T_3 = \frac{y_3(x_6-x_1) - y_6(x_3-x_1) + y_1(x_3-x_6)}{(x_3-x_6)(x_3-x_1)(x_6-x_1)} \tag{3.141}$$

## III.5.9  Numerical Examples

The plane strain derivation given in Section III.5.8.1 was programm-
ed in FORTRAN IV for operation on TRW's CDC 6500 computer.  The program has
the option to perform either a single fold bladder analysis, or a general
elasto-plastic, large deflection plane strain analysis.  The program itself
is described in detail in a separate document.  In this section, several
example problems are presented for which alternate solutions have been ob-
tained.  In all cases, the computer results generated herein agree very
well with previous published solutions, giving a high degree of confidence
that the program will conduct the single fold bladder analysis accurately.

### II.5.9.1  Hollow Cylinder

To investigate the application of the theory presented herein to
elasto-plastic problems, a long cylinder subjected to internal pressure
was studied.  This example was used by Ref. 49 in a finite element solution.
The cylinder had the following characteristics:

| | |
|---|---|
| Shear Modulus | $G$ = 3,850 ksi |
| Inner Radius | $a$ = 1.0" |
| Outer Radius | $b$ = 2.0" |
| Elastic Modulus | $E$ = 10,000 ksi |
| Poisson's Ratio | $\mu$ = 0.3 |
| Yield Stress in Tension | $\sigma_y$ = 20 ksi |
| Post Yield Modulus | $E_p$ = 0 |
| Yield Stress in Shear | $K$ = 11.54 ksi |

A cross-section cut through the cylinder was assumed to be in a
state of plane strain.  One-quarter of this slice was modeled using 24
linear strain triangular elements.  A total load of 15 ksi internal
pressure was applied in five equal increments, and the iterative correc-
tion continued until $\varepsilon \leq .01$.

Some typical results are shown in Figures 3-9, in which r is the
radius of the cylinder.  The circles represent finite element results,
while the solid lines are from Ref. 55 using the Von Mises yield criterion
and the Prandtl-Reuss flow law.  Figure 3-9a is a normalized load-deflection
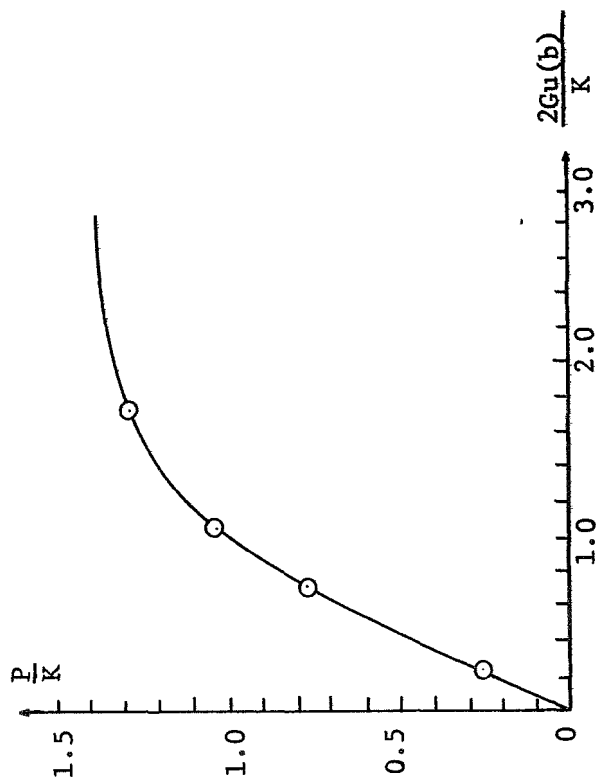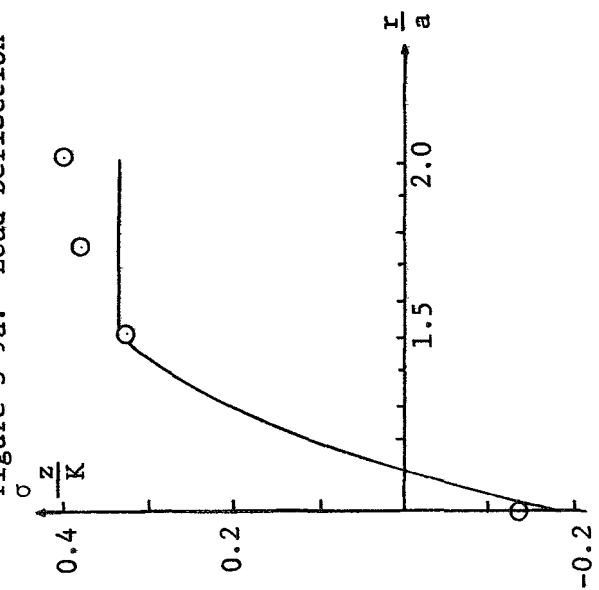
Figure 3-9b. Radial Stress

Figure 3-9d. Circumferential Stress
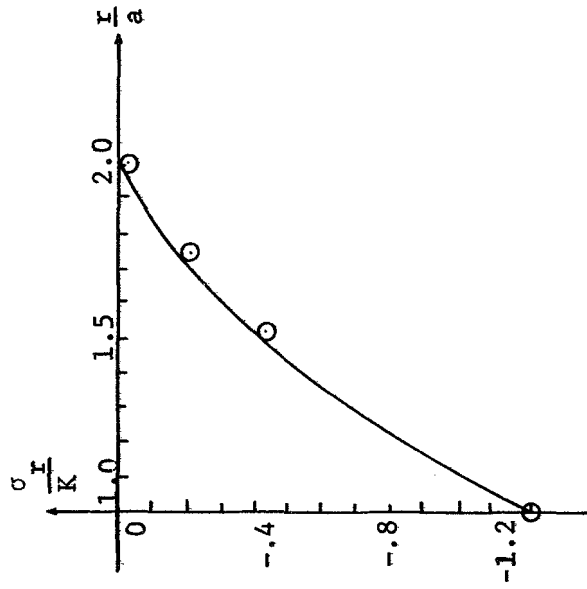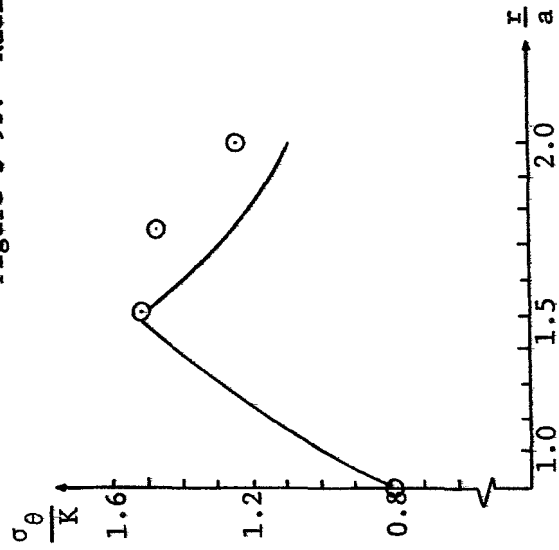
Figure 3-9a. Load Deflection

Figure 3-9c. Axial Stress

curve, where u(b) is the radial displacement measured at r = b, the outer radius of the cylinder. In this problem, the nonlinearity is caused by yielding which begins in the finite element model at the inner surface r = a at a load slightly greater than P = 9 ksi (P/K = 0.78). The other figures are plotted for the maximum load of P = 15 ksi (P/K = 1.3). These results show that accurate solutions for displacements and stresses can be obtained using the theory proposed herein. Note also that this problem represents the most severe type of elasto-plastic behavior, since no strain hardening is assumed.

### III.5.9.2 Notched Tensile Specimen

A notched tensile specimen assumed to be in the condition of plane strain was analyzed in Ref. 49. However, in Ref. 49 constant strain triangular finite elements were used, whereas the present theory has been implemented using linear strain triangles. This problem is used to investigate the various solution procedures outlined above. The nonlinearity in this problem is caused by localized yielding of the notched sheet.

Figure 3-10 shows the tensile strip and the finite element mesh. Due to symmetry, only one quarter of the strip was considered. A total tension load $\sigma$ = 30 ksi applied in eight equal increments.

Figure 3-11 shows some of the results obtained for this problem in the form of a plot of maximum strain in the x direction versus applied load. The solid dots represent a solution for which iteration at constant load was performed until $\varepsilon \leq 10^{-4}$. The circles give the results obtained by adding the residual error to the incremental load for the next step. The x data points show the conventional linear incremental solution. Both of the methods for correcting equilibrium unbalance gave solutions significantly different from those obtained by the conventional step-by-step procedure. For this problem, the addition of the residual to the next step ("o" in Figure 3-11) improved the strain predictions considerably over the conventional solutions ("x" in Figure 3-11), at no additional cost in computer time.
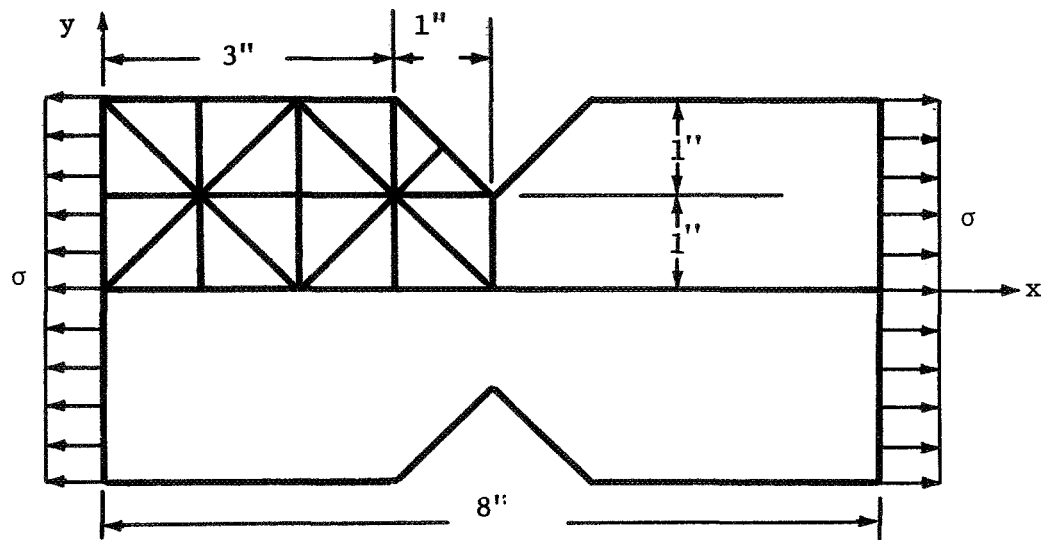
E = 10,000 ksi

$\mu$ = 0.33

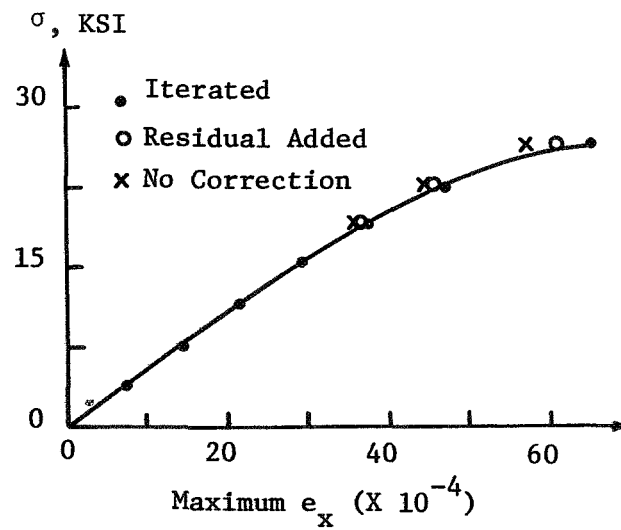$E_p$ = 0

$\sigma_y$ = 35 ksi

Figure 3-10.  Tensile Strip



Figure 3-11.  Stress Versus Maximum Strain
for Tensile Strip

III.5.9.3  Elastic Cylindrical Bending Problem

In Ref. 36, large deflection-moderate strain plate problems were
solved by using triangular plate bending discrete elements. These solu-
tions were limited to the elastic range and compared very well with
analytical solutions given by Ref. 31. In particular, cylindrical bending
of infinitely long plates due to uniform pressure was considered. This
same type of plate problem was used herein to verify the theory and solu-
tion method for large deflection problems.

The infinite length plate was considered as a plane strain problem.
Figure 3-12 shows the geometry of the plate section and the finite element
grid. The width of the plate was taken as 20", and only half of the plate
was modeled due to symmetry about the centerline. The material properties
were

$$E = 30,000 \text{ ksi}$$
$$\mu = 0.3$$

and a total load of q = 5 ksi was applied in 40 equal increments. The
iteration at constant load was applied after each increment until
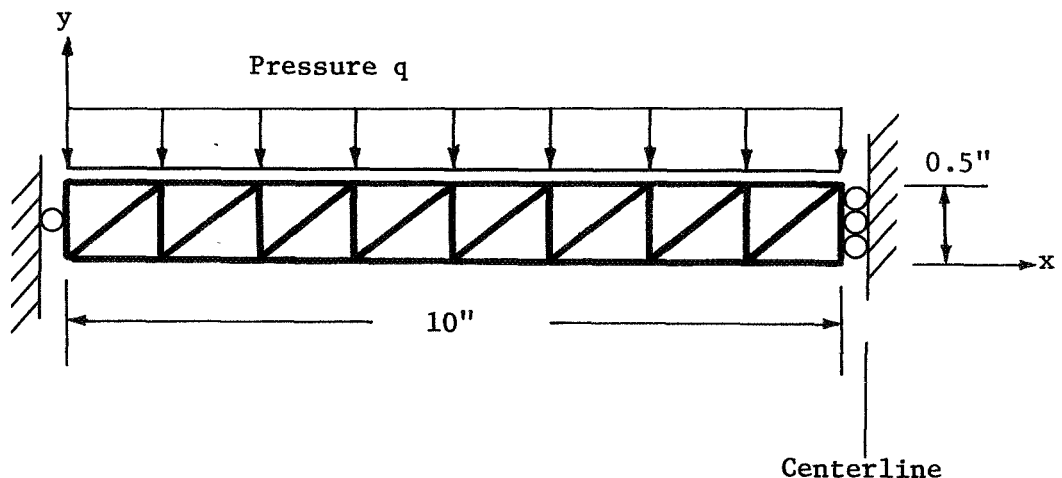$\varepsilon \leq 10^{-4}$.



Figure 3-12.  Plate Bending Problem

Some of the computer results are shown in Figures 3-13 and 3-14 as circles, with the analytical solutions from Ref. 31 represented by the solid lines. As can be seen from Figure 3-13, excellent agreement was obtained between the analytical and finite element solutions for deflection at the center of the plate. Good agreement was also obtained for membrane stresses, as measured at the center of the plate and shown in Figure 3-14.

This plate problem also demonstrated the need to use the nonlinear strain-displacement equations to compute elemental strains, and eventually stresses. In Ref. 39, only the linear portion of the strain-displacement equations was used, since in any one step, the incremental strains should be small enough that the nonlinear terms can be neglected. However, for the plate problem considered above, large midplane strains develop due mostly to the rotation of this plane, and enters into the problem only through the nonlinear portion of the strain-displacement relations.
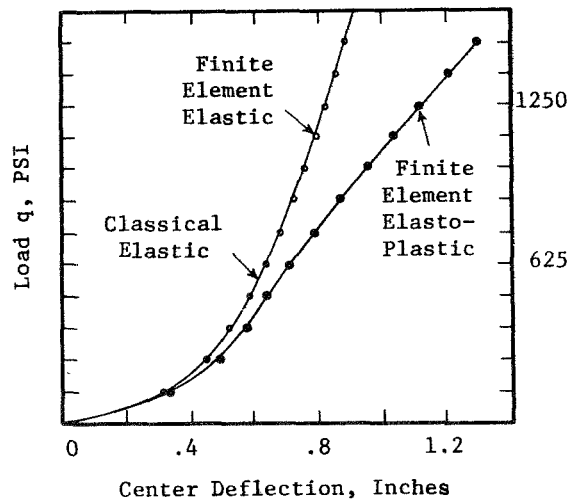


Figure 3-13.  Load-Deflection Curve for Plate Problem
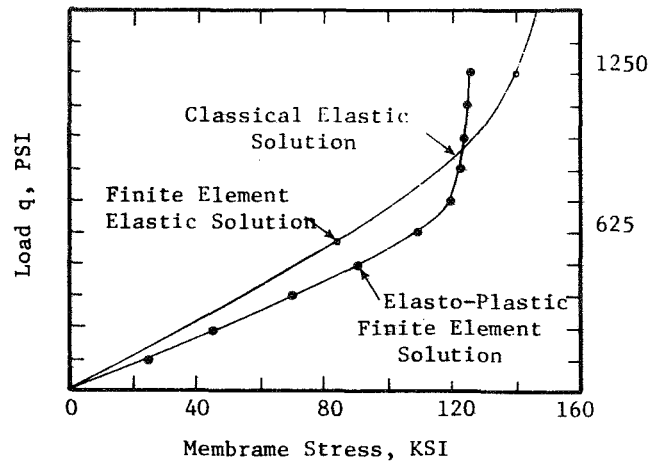
Figure 3-14.   Membrane Stress Versus
              Load for Plate Problem

Numerical results generated by neglecting the nonlinear contribution to
the strain, even for small load increments, (0 to 2.5 ksi in 20 steps),
are considerably in error.  This error was eliminated by rerunning the
same problem in 200 steps, at the expense of much more computer time.

III.5.9.4   Elasto-Plastic Cylindrical Bending Problem

The elastic large deflection plate cylindrical bending problem con-
sidered above was rerun using the following changes:

$$E_p = 75 \text{ ksi}$$

$$\sigma_y = 110 \text{ ksi}$$

These values were obtained by fitting a bilinear approximation to a typical
true stress-true strain curve of a low-alloy structural steel.  True
strains greater than 20% were neglected in the fitting.

A total load of q = 1.25 ksi was applied to the plate in ten equal
increments, and iteration after each increment was performed until $\varepsilon \leq 10^{-4}$.
Figures 3-13 and 3-14 show some of the numerical results for this problem.
The elastic solution from above is also given for comparison in these
plots.  From both figures it can be seen that considerable difference
exists between the elastic and elasto-plastic solutions for both deflec-
tions and stresses.  In fact, due to the progressive yielding through the
plate thickness, the slope of the load-deflection curve, Figure 3-13,

changes noticeably at a load near 625 psi. Large strains were not developed during the solution to this problem.

III.5.9.5  Computer Running Times

All of the above examples were run on a CDC 6500 computer. Typical run times are shown in Table 3-2.

Table 3-2  Solution Times

| Example | Degrees-of Freedom | Running Time (seconds) |
|---|---|---|
| Hollow Cylinder | 130 | 69 |
| Notched Strip - No Correction | 98 | 34 |
| Notched Strip - Residual Added | 98 | 34 |
| Notched Strip - Iterated | 98 | 146 |
| Elastic Cylindrical Bending | 51 | 223 |
| Plastic Cylindrical Bending | 51 | 236 |

III.5.10  Finite Element Analysis of Single Folds

During the course of this investigation, several finite element models of single folds were devised and used to compute critical plastic bending strains. In this section, these models will be reviewed and recommendations for simulating the single fold will be presented. It should be noted that all models considered herein are assumed to fold symmetrically about the folding centerline.

III.5.10.1  Flat Plate Loaded by Uniform Pressure

Figure 3-15a shows the finite element grid and loading for this model, and Fig. 3-15b gives the deformed shape after a total load of 88 psi had been applied. The dimensions were chosen arbitrarily as 1/8" thick and 1-1/2" long. The material properties of E = 300 KSI, $\mu$ = 0.3, $E_p$ = 42 KSI, and $\sigma_y$ = 6 KSI were obtained by fitting a bilinear approximation to a uniaxial stress-strain curve of 1100-0 aluminum. The convergence
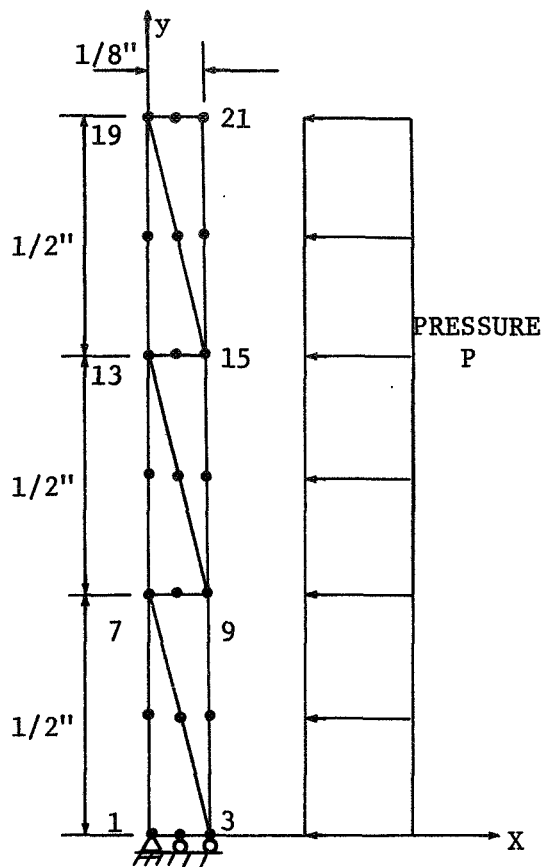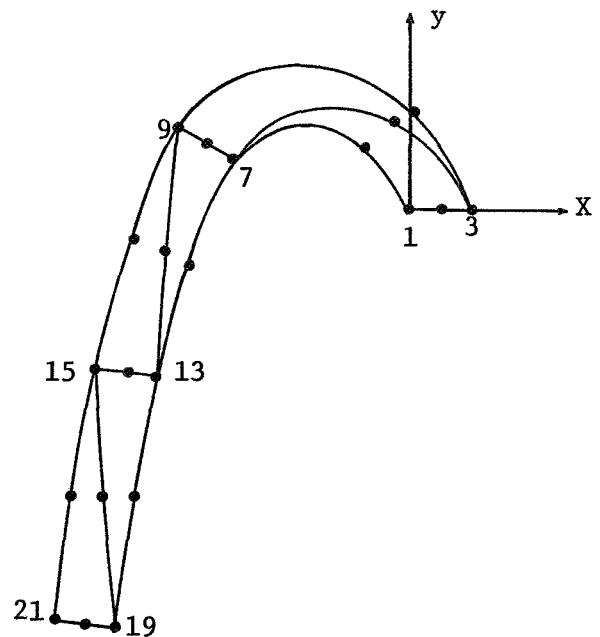
Fig. 3-15a - Model



Fig. 3-15b - Folded Bladder

criterion was $\varepsilon \leq 1.0$, and a total load of 88 psi was applied in 11 equal increments. Including the iterative corrective procedure, a total of 192 complete solutions were performed on the CDC 6500 in 174 seconds. Convergence slowed down drastically after the 11-th step, and the problem was therefore terminated.

Table 3-3 shows the results obtained for this problem. However, Fig. 3-15b illustrates best the reason why this model is unsuitable for large strain bladder analysis. Note that in Fig. 3-15b, the elements defined by nodes 1-3-7 and 3-7-9 are severely distorted from their original triangular shape. However, the area integrations used to derive the stiffness matrix for this element assume the sides remain straight, and therefore considerable error is introduced into the model due to the curving of the sides. Dividing the region into many more elements would minimize this

Table 3-3 — Aluminum Bladder

| Total Load (KSI) | $\sigma_{eq}$ Node 1 (KSI) | Elastic Strains, Node 1 $\varepsilon_x$ | $\varepsilon_y$ | $\gamma_{xy}$ | Plastic Strains, Node 1 $\varepsilon_x$ | $\varepsilon_y$ | $\gamma_{xy}$ | Total Defl. Node 21 (IN.) X | Y |
|---|---|---|---|---|---|---|---|---|---|
| .008 | 2.26 | .0031 | -.0078 | -.0016 | .0 | .0 | .0 | -.0897 | .0029 |
| .016 | 4.50 | .0062 | .0157 | -.0030 | .0 | .0 | .0 | -.1798 | -.0003 |
| .024 | 6.21 | .0088 | -.0228 | -.0037 | .0028 | -.0038 | -.009 | -.2931 | -.0130 |
| .032 | 8.28 | .0118 | -.0312 | .0012 | .0305 | -.0402 | -.0035 | -.6976 | -.1405 |
| .040 | 11.37 | .0153 | -.0434 | .0090 | .0723 | -.0943 | .0045 | -1.1642 | -.5210 |
| .048 | 17.29 | .0147 | -.0666 | .0379 | .1480 | -.1925 | .0488 | -1.4484 | -1.3689 |
| .056 | 22.19 | .0078 | -.0863 | .0651 | .2009 | -.2655 | .1019 | -1.3278 | -1.8702 |
| .064 | 25.31 | .0022 | -.1040 | .0824 | .2258 | -.3019 | .1314 | -1.1669 | -2.1179 |
| .072 | 28.25 | -.0037 | -.1213 | .0929 | .2395 | -.3233 | .1486 | -1.0311 | -2.2503 |
| .080 | 31.16 | -.0066 | -.1293 | .1004 | .2484 | -.3374 | .1597 | -.9240 | -2.3257 |
| .088 | 35.19 | -.0075 | -.1156 | .1051 | .2562 | -.3510 | .1702 | -.8436 | -2.3664 |

problem, but would greatly increase computer running time. In addition, the large pressure difference across the bladder may introduce unwanted variations in strains, etc. For these reasons, this model was not investigated further for folding strain analysis.

III.5.10.2  Model to Check Analytical Solution

In Section III.1, an analytical solution to the "N-layered" single folding bladder problem was presented. If the bladder is made from only one material, and there is no internal or external pressure, the hoop strain at the inner radius can be computed from

$$e = \ln \frac{a_o (a_s + t/2)}{a_s (a_o + t/2)} \tag{3.142}$$

where

$$t = \text{sheet thickness}$$

$$a_s = \text{starting inner radius}$$

$$a_o = \text{final inner radius.}$$

This equation was plotted for $t = 0.02''$ and a range of $a_o$ values in Figure 3-16 as a solid line. The starting inner radius $a_s$ was computed from theory of elasticity as the radius at which yielding first occurs. For this problem, $a_s = 14.95''$.
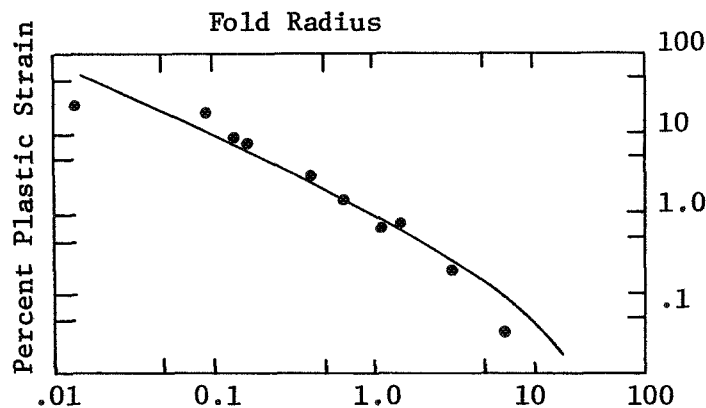


Figure 3-16  Plastic Strain Versus Fold Radius for Sheet Bending

Figure 3-17 shows the grid of a finite element plane strain model of this same problem. This model was devised for two reasons: (1) to define
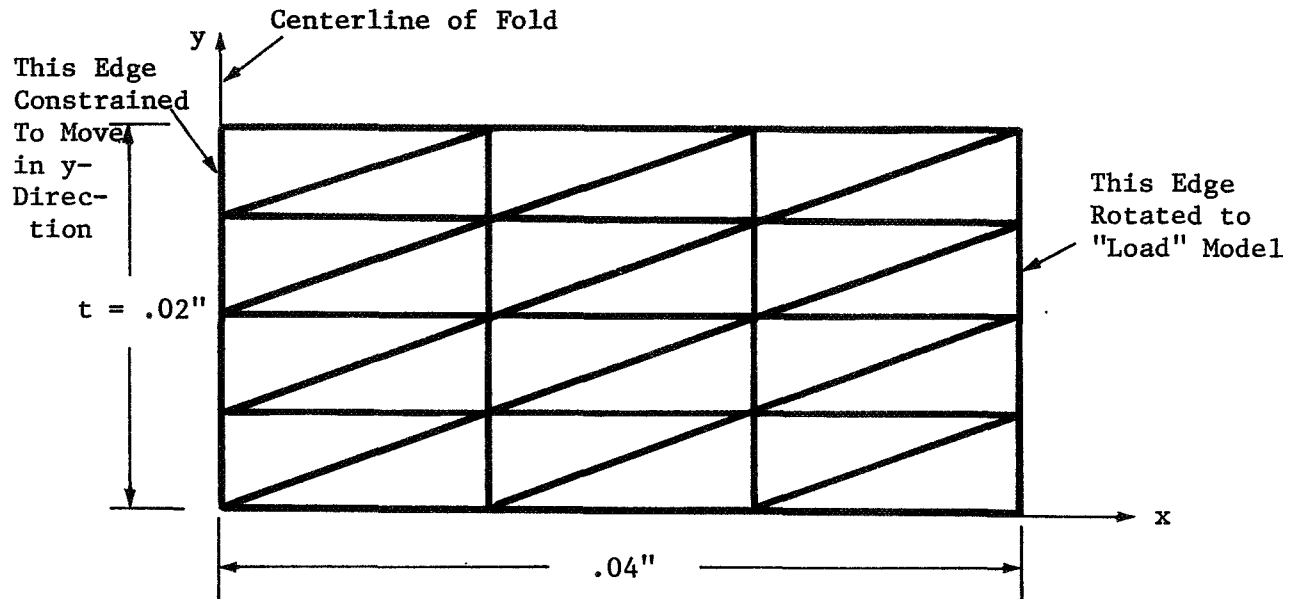


Figure 3-17   Bladder Model

regions in which the solution of Section III.1 is valid; and (2) to investigate its usefulness as a model for bladder folding. The model was "loaded" by specifying displacements along one boundary such that this edge remains plane and the nodal points do not move radially along this boundary with respect to each other. This was done to simulate the "planes remain plane" assumption in the analytical solution. The inner radius was computed by fitting a second order curve to the two nodal points on the inner surface closest to the centerline of the fold. Zero hardening was postulated to duplicate the assumptions made in the analytical model. The other input quantities were

$$E = 10,000 \text{ ksi}$$

$$\mu = 0.33$$

$$\sigma_y = 6 \text{ ksi}$$

$$\varepsilon \leq 10^{-2}$$

The model was loaded, starting from a radius of $a_s$ = 18.30" (at which the first yield occurred) to an inner radius of $a_o$ = 0.0125" in thirteen steps. Some typical plastic hoop strains obtained for this solution are shown as circles in Figure 3-16.

As can be seen from Figure 3-16, the finite element solution agrees well with the analytical results over a wide range of folding radii. However, for small and large folding radii, the solutions did not agree closely. At large radii, part of the cross-section of the finite element model was still elastic, whereas the analytic solution neglects elastic behavior. At small radii, shear strains grew large in the numerical model, distorting originally plane sections (except at the end boundaries). The closed-form solution assumed planes remain plane. The shear strains tended to relieve the hoop strains in the finite element idealization at small radii. The thirteen steps took 376 seconds of CDC 6500 time.

This model was quite successful in duplicating the analytical solution for the range of inner radius/thickness ratio of 5 to 100. That is, within this range, the solution of Section III.1 is adequate, however, for a ratio of less than 5, the finite element model should be used.

III.5.10.3  Loading by Imposed Displacements

A finite element model similar to the above was loaded by displacing one node as shown in Fig. 3-18. Thus the right end of the model is not constrained to remain straight as in Section III.5.10.2. The loading process is set up so that the size of the increment decreases as the folding radius decreases. This is illustrated in Figure 3-18 for five load steps. Also shown is the final folded configuration.

Several computer runs demonstrated that this method of loading is inefficient for two reasons. Firstly, the initial step for loading any model should be such that the yield stress is not exceeded, in order to minimize convergence problems. However, the loading method proposed in Fig. 3-18 imposes a very large displacement during the first step, and $\sigma_y$ is easily exceeded at many nodes. Increasing the number of steps (and therefore decreasing the size of the first step) was not successful because computer running time went up drastically. A scheme of equal load steps was also unsuccessful because the final step size was too large. Secondly,
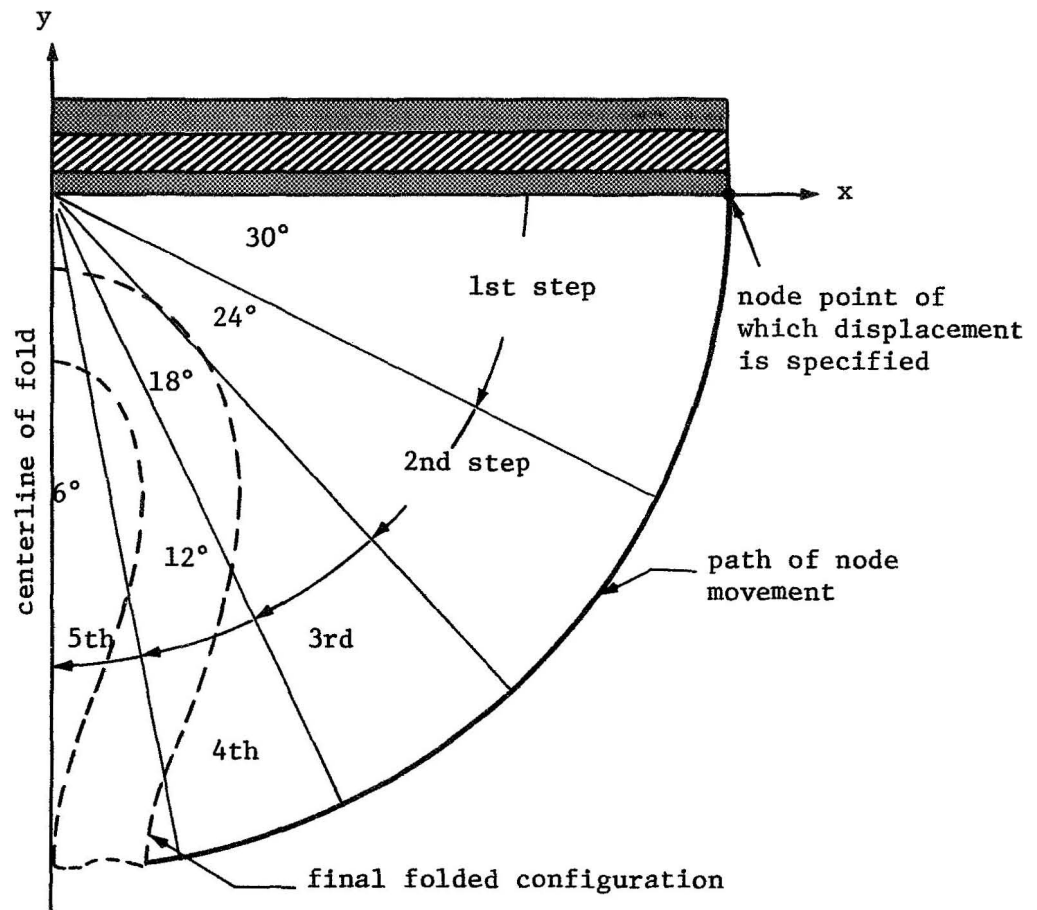
Figure 3-18   Incremental Loading

the model had to be relatively long to realistically simulate the bladder, resulting in excessive computer running times.  For these reasons, this loading procedure was given up.

III.5.10.4   Final Single Folding Model

A model very similar to that described in Section III.5.10.2 was selected for single fold analysis.  This model was chosen because of the good agreement with the analytical solution, and also because a valid bladder folding strain analysis can be accomplished in a reasonable period of computer time.  The mesh generation, etc., for this model was automated so that a minimum of input is necessary.

For the single fold, the user must input the following information:

Number of layers

Number of materials

Which material is in which layer

Properties of each material

Thickness of each layer

Some variables will be set to nominal values if not entered by the user. These are

| Variables | Nominal Value |
|---|---|
| Maximum Load Steps | 25 |
| Maximum Band Width | 50 |
| Length/Thickness Ratio | 10 |

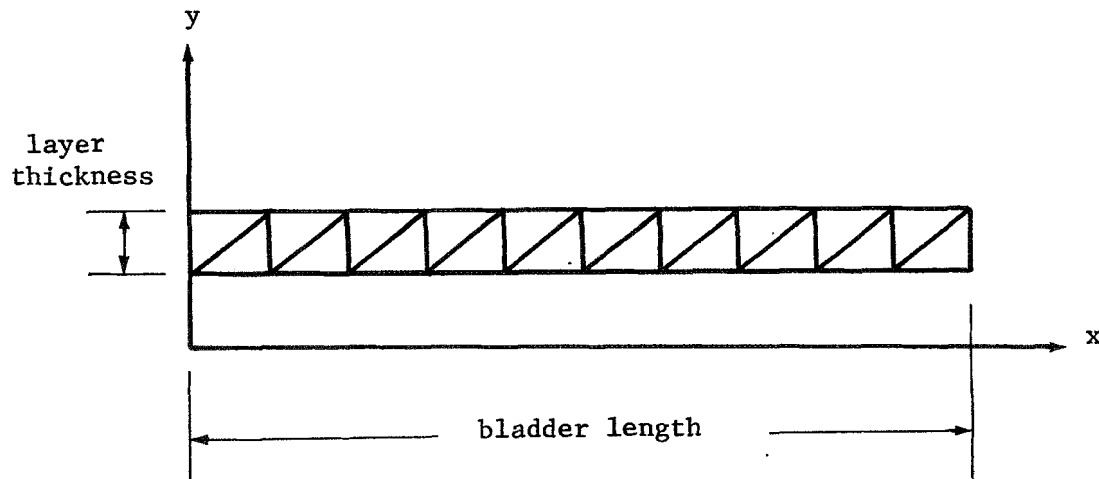Each layer will consist of finite element arrays as shown in Figure 3-19.



Figure 3-19   Finite Element Layer:   Single Fold

Up to ten such layers can be stacked in the y direction to simulate composite bladders.   The fold will be formed by rotating the free edge (right-hand side) as in the model of Section III.5.10.2.

Equivalent plastic strains will be computed for each node in the bladder.   The maximum of these strains in each layer will be found for each load increment.   These will then be used to compute fatigue life in

each layer as described subsequently.  In addition, an approximation to the inner folding radius is computed at each step.

III.6.0  Task 2.3:  Conduct Single Fold Experiments

The following test plan was approved by JPL. These limited experiments were for the purpose of guiding the theoretical analysis and providing some direct bladder fatigue information.

### TEST 1

In order to support the theoretical analysis of the behavior of folded materials, a long strip of material will be folded to bring together the edges opposite and perpendicular to the fold. Means will be provided to seal the contacting surfaces and to evacuate the open space inside the folded sheet specimen. The thickness and rigidity of the specimen will be chosen to produce minimum or no plastic strain before evacuation but to produce considerable plastic strain at 15 psi pressure difference. The spacing of grid lines drawn parallel to the fold will be measured with the 2-component microscope when the sheet is flat, when folded but not evacuated, and for various amounts of pressure difference applied to the folded and sealed pocket. (See Fig. 3-20)

### TEST 2

A correlation will be made between the strains produced by test 1 above, which is amenable to theoretical analysis, and the strains produced by compressing folds between parallel jaws. This will provide a tie-in between the computed situations prevailing in item 1 above and the fatigue tests of item 3 below.

### TEST 3

Apparatus for low-cycle fatigue testing will be devised for subjecting single folds to compressions correlated to items 1 and 2 above and for compressing double folds to primary-fold radii having such correlation. The secondary fold of the double-fold tests will be controlled and related, through the primary-fold radius, to the simpler tests and to the theoretical computations.

The folding operations will be duplicated with sufficient accuracy to insure that each fold repetition is free to occur at the same position on the material. One cycle is to be measured from the flat configuration. Examination of the condition of the material will be made after each of

SINGLE FOLD MODEL

VACUUM
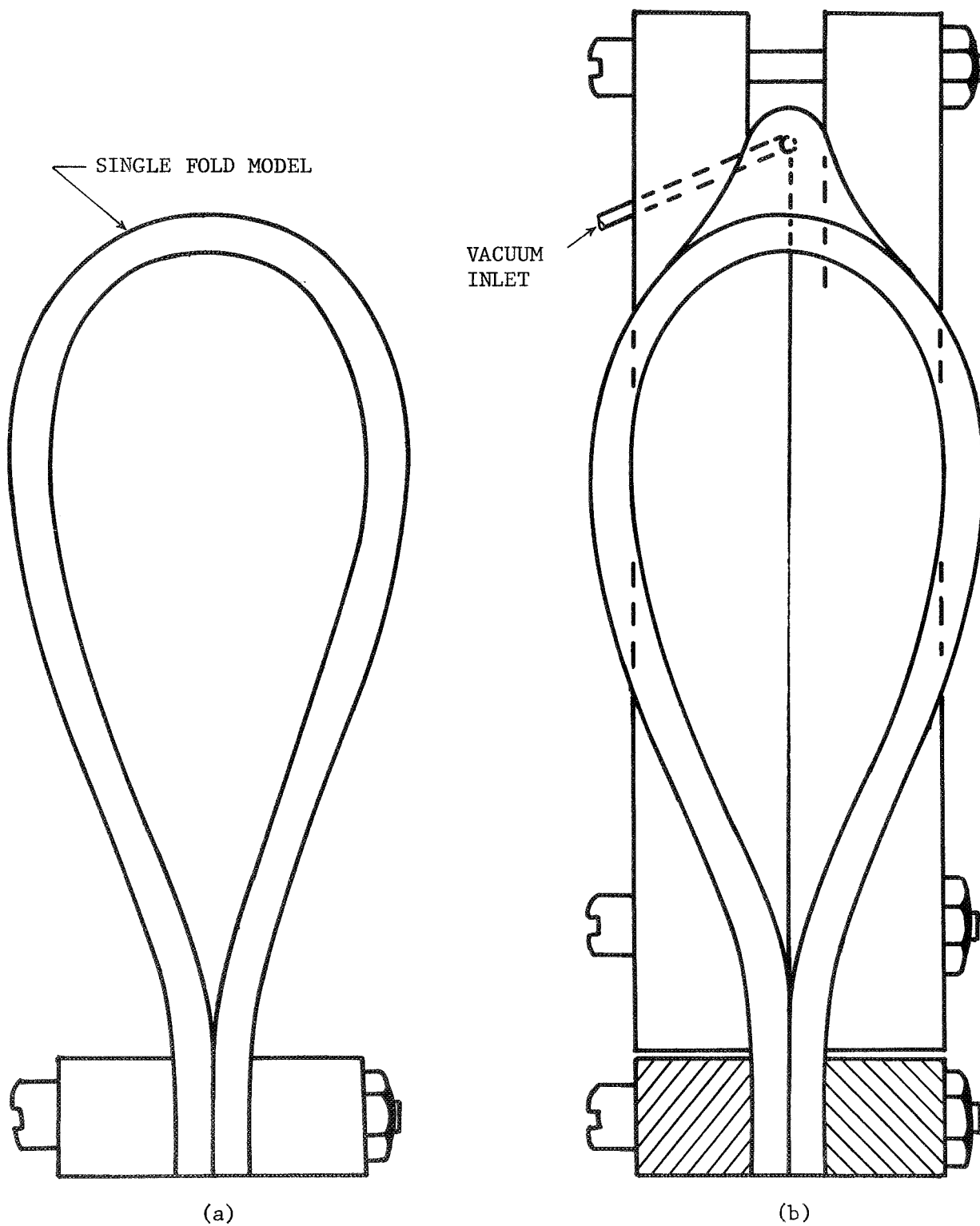INLET

(a)                                    (b)

Figure 3-20  - Single Fold Pressure Test Setup

the earlier cycles and less frequently during the later cycles, when a longer test is warranted. Examinations will be based on surface condition, penetration as determined by electric spark or other appropriate techniques, or loss of strength when subjected to tension or pressure.

Uniaxial fatigue tests will be conducted using the same material as in the folding-unfolding tests. Thus information can be generated to verify any theory which seeks to use uniaxial fatigue test data to interpret multiaxial fatigue strains in bladders.

However, after several computer runs, it was concluded that the 15 psi pressure difference across the bladder in Test 1 was not adequate to produce large folding strains. Therefore, the static single folding device was redesigned. This new folder allowed tests 1 and 2 above to be combined and is described in the following section.

### III.6.1 Static Single Folding Device

A device has been designed and built which will allow controlled single folding of sheet specimens. The folder, shown in Fig. 3-21, applies forces to the end of a sheet to create the fold. No bending moments are transmitted to the sheet, since the jaws gripping the ends of the sheet are mounted in bearings and are counterbalanced. Thus analysis of this type of fold is straightforward using the plane strain finite element program.
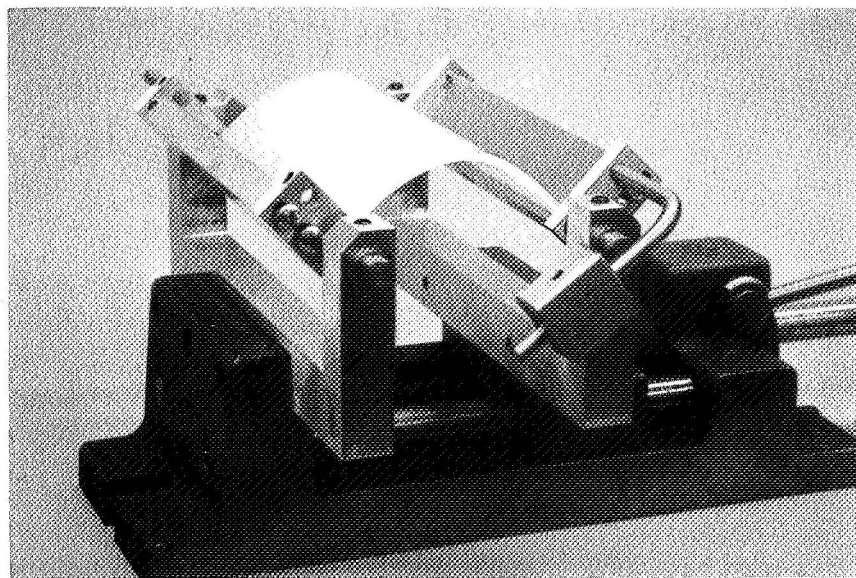


Figure 3-21  Single Fold Device

The single-fold bending fixture was developed to apply well-defined constraints to a specimen and to determine the configuration. Using pivoted end (zero bending moment) loading of a wide flat column of the flexible material, the pivot axes were brought together to various spacings and the resulting outside bend radius was measured. Since such a buckled column does not bend to a configuration characterized by a single value of the radius, the equivalent radius of a 60° arc of the material was determined. A measuring fixture was constructed to determine this equivalent radius by use of three lines of contact at the ends and at the center of the 60° arc.

The single-fold bending fixture allows convenient access to the convex surface of the fold for the purpose of measuring strain between contour lines. For short, thick specimen of soft materials, the exterior radius r/t ratio can approach 2.

Figure 3-22 shows the type specimen used in the single fold device. In this figure, the following quantities are defined:
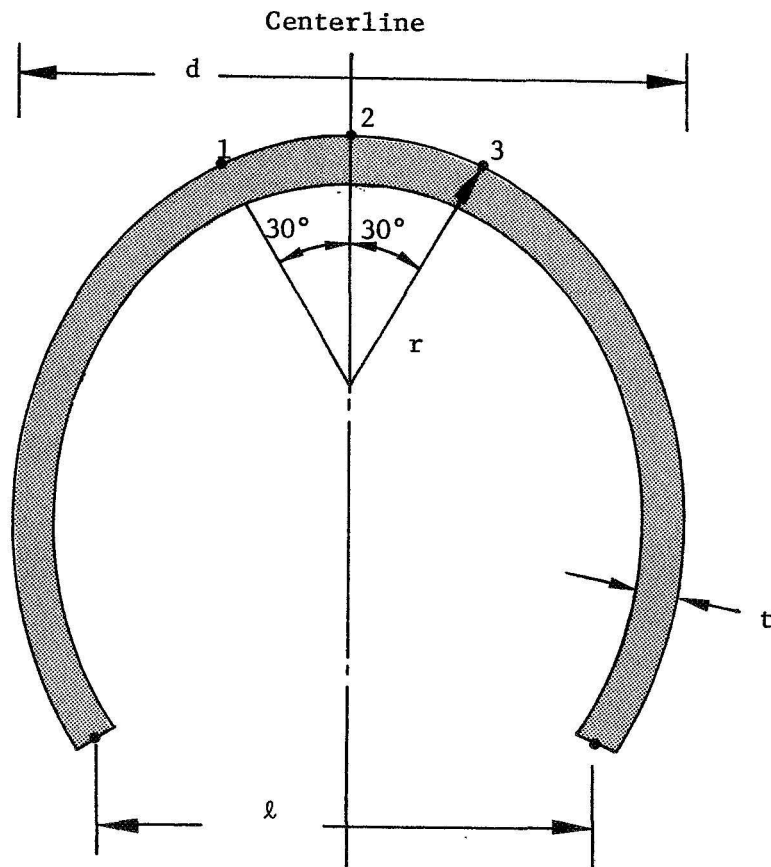


Figure 3-22 - Single Fold Test Specimen

$\ell$ = length between free ends

$\ell_o$ = original $\ell$

t = sheet thickness

r = equivalent radius of a 60° arc of material for minimum radius

The specimen is "loaded" by decreasing the distance between free edges from the initial $\ell_o$ to $\ell$. For each increment of load, r is measured over a 60° arc by fitting a special gaging device to points 1, 2, and 3. The distance d is determined by calipers as long as d > ($\ell$ + t).

Figure 3-23 gives results obtained for two different thicknesses of low-density polyethylene sheet. The solid dots in Fig. 3-23 are for t = 0.125" and $\ell_o$ = 4.0", while the solid triangles are for t = 0.252" and $\ell_o$ = 3.652". The circles are from a finite element solution and will be discussed in a subsequent section.
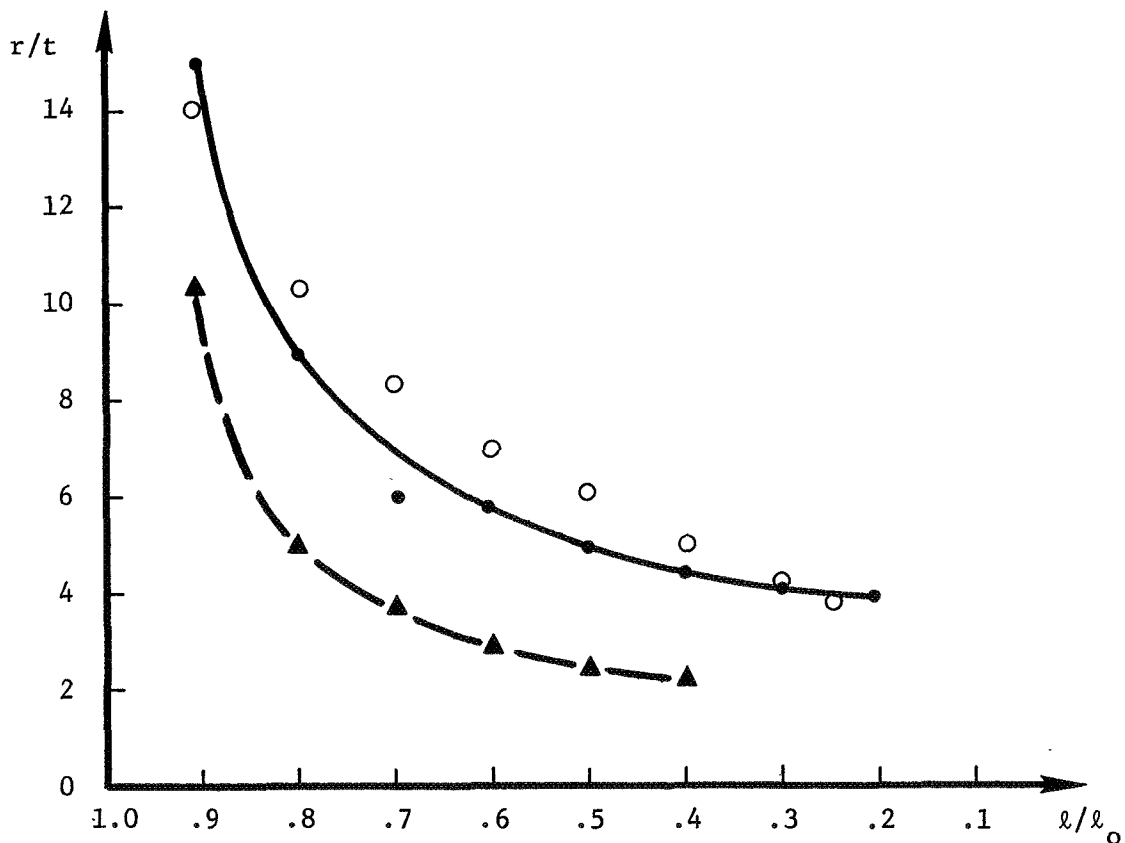


Figure 3-23 - Single Fold Results

3-82

## III.6.2  Uniaxial Tensile Tests

In order to duplicate the results of the above section using the
finite element computer program, uniaxial stress-strain curves of the
materials of interest were obtained.  Since such tests are straight for-
ward, only the final results will be presented here.  The low-density
polyethylene specimens were 1/4" thick and 1/2" wide, while the cellulose
acetate butyrate specimens were 3/32" thick and 1/2" wide.

The stress-strain plots showed that the characteristics of low-density
polyethylene can be represented by a bi-linear approximation with a
modulus of elasticity of about 15,000 psi joined by a line of constant
stress of about 1,080 psi.  The bi-linear approximation for cellulose
acetate butyrate is about 180,000 psi for the modulus of elasticity in
the initial-strain region and a 4,000 psi constant stress in the plastic-
flow region.

## III.6.3  Single Folding Fatigue Tests

Two versions of a single-fold fatigue fixture were built and tested.
These fixtures were made for use in the Research Incorporated programmable
loading machine.  A cyclic programmer was added to this machine for con-
trolling the time in which the fatigue specimen was held in a folded
condition and the time in which it was held in the straightened condition
after opening the fold.  The first fixture allowed the machine to pull
the specimen approximately to a straight and unbent condition between
folding cycles but the folded condition included two 90° bends in addition
to the 180° fold between parallel jaws.  After preliminary tests, the
second single-fold fatigue fixture was prepared to eliminate the 90°
bends and to provide a smooth and very gradual rolloff of the parallel
jaws.  This rolloff, well within the specimen width, prevented premature
fold damage at the edge of the specimen.  The recorded data on single-
fold fatigue tests was obtained with the second fixture.  Figure 3-24
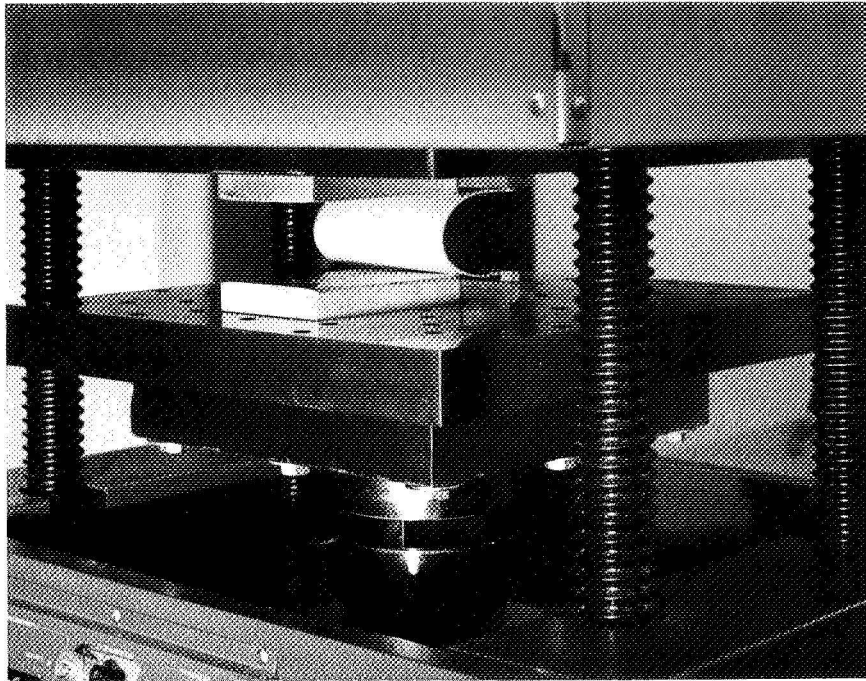shows the experimental setup.

Figure 3-24 - Single Fold Fatigue Test

Table 3-4 gives a summary of the test results.

Table 3-4  Folding Fatigue Results

| Material | Radius/Thickness of Fold | No. Cycles | Condition |
|---|---|---|---|
| Cellulose Acetate Butyrate | 4 | 5 | Failure |
| Cellulose Acetate Butyrate | 6 | 10 | Failure |
| Teflon | 2.5 | 2100 | No Failure |
| (continued from 2100 cycles) | 2 | 1780 | No Failure |
| S/N 31269  JPL 103 | 2.5 | 2320 | No Failure |
| (continued from 2320 cycles) | 2 | 1160 | No Failure |

The fatigue testing equipment was intended for use with materials and bend radii which exhibit low-cycle, fatigue damage.  Tests have ranged from folding cellulose acetate butyrate between a jaw spacing of four times the thickness (4t), which produced a hole after five cycles, to folding Teflon to 2.5t for 2,100 cycles and then to 2.0t for 1,780 cycles without failure.

III.6.4  Conclusions

The experimental investigation to date has been primarily devoted to the development of testing techniques.  This included development and use of single-fold fatigue fixtures, a single-fold bending apparatus, and a radius-measuring fixture.  An investigation was made of various sheet materials that might be used as thick-sheet models of other sheet materials. In developing techniques for the use of such materials, data was obtained on single fold fatigue performance, on the characteristics of single-fold bends, and on the stress-strain characteristics of the materials.

Although extensive measurements were not performed during this program, considerable progress was made in the development of experimental techniques.  The test fixtures will be retained and the laboratory capability will be available for future investigations of materials that are subjected to large strains causing plastic flow.

It should be noted here that the general shape of the curve of Figure 3-23 will be similar for teflon and other plastics.  Polyethylene was used in the actual static folding tests reported herein since it is much less stiff than teflon.  That is, the static folder could not fold a sheet of teflon of the thickness required to reach low r/t ratios.

III.7.0   Task 2.4:   Compare Theory and Experiment-Single Folds

In order to verify the finite element theory and coding for single fold analysis, the test specimen shown in Fig. 3-22 was modeled using the code developed in Section III.5.   The finite element model simulated half of the sheet, contained sixteen plane strain elements and 102 degrees-of-freedom, and is shown in Fig. 3-25.   The left-hand nodes (along the center-line) were constrained to move only in the vertical direction, and node
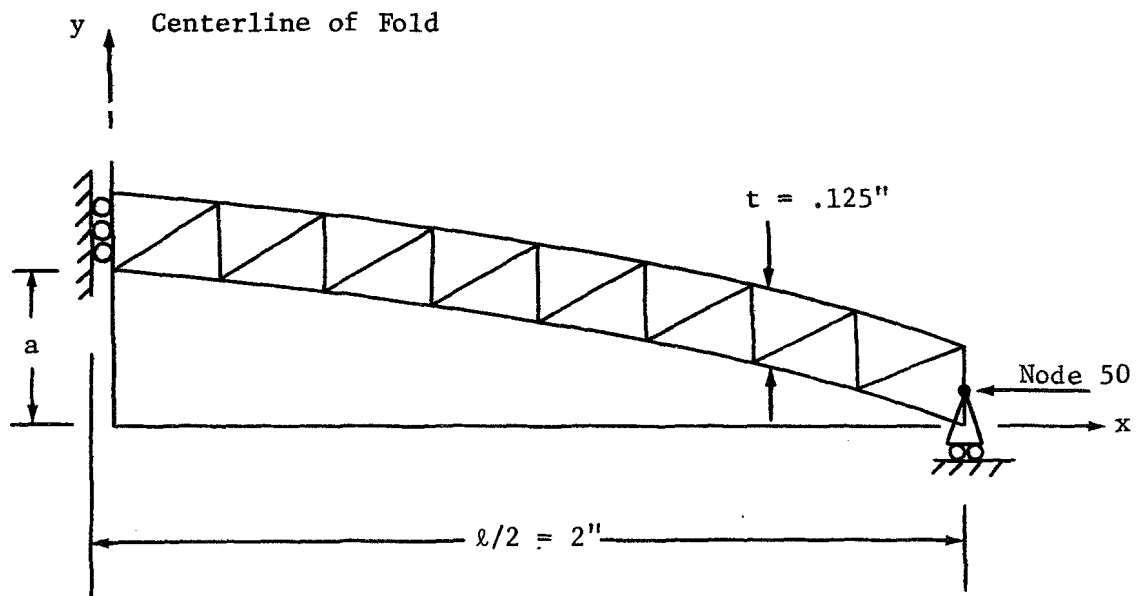


Figure 3-25 -   Single Fold Test Model

50 was constrained to move only in the horizontal direction.   The model was "loaded" by moving node 50 toward the centerline.   To avoid Euler buckling, the sheet was given a slight initial curvature of $a \sin \frac{\pi}{\ell} (\frac{\ell}{2} - x)$ with $a = .1"$, along the bottom surface.

The material properties were obtained from a uniaxial tension test (described in Section III.6.2) as $E = 15$ ksi, $\mu = .35$, $\sigma_y = 1.1$ ksi, $E_p = 0$.   The load was applied to the finite element model in 77 equal increments of $0.02"$/step, giving a final $\ell/\ell_o$ value of $0.23$.   Such a small step size was found to be necessary to successfully avoid the buckling instability as the sheet was initially loaded.   The load-deflection

curve obtained by the finite element solution is shown in Fig. 3-26. The horizontal line at a load of 1.71 #/in represents the conventional elastic Euler buckling load. The sheet began to yield at $\ell/\ell_o$ = .55, changing the slope of the load displacement curve. The problem took 16 minutes of CDC 6500 computer time.
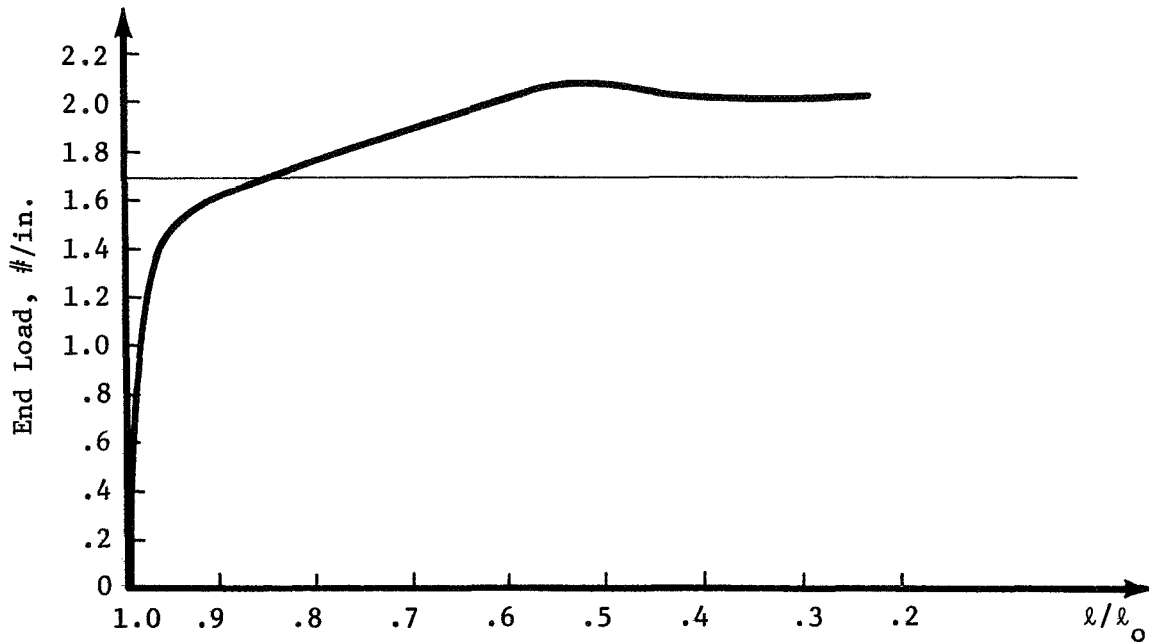


Figure 3-26 -  Load-Displacement Curve

Some of the finite element results are shown in Fig. 3-23 as circles. As can be seen by comparing the finite element results (circles) to the experimental results (solid dots and line), excellent agreement was obtained, particularly in the critical range of low r/t ratios. In addition, the following comparison was also made:

| $\ell/\ell_o$ | d/t (see Fig. 3-22) | |
| --- | --- | --- |
| | Experimental | Finite Element |
| 0.4 | 14.2 | 13.9 |
| 0.3 | 11.9 | 11.7 |

III.7  Conclusions

In view of the excellent agreement between the finite element plane strain results and the experimental results shown above, and the fine comparison between previous published solutions and finite element solutions in Section III.5.9, no "refinement" of the finite element theory and coding presented herein is necessary.  The present computer program should be capable of accurately predicting single folding strains in composite bladder structures.

## III.8.0  Task 2.5:  Rolling Single Folds

A quasi-static analysis of a rolling single fold is proposed herein.
In this type of analysis, a complete single fold is first formed, using
the plane strain finite element computer program to predict strains,
stresses, etc., during the formation of this fold.  The program is then
interrupted, and the resulting information is stored on tape and disk.
Next, the loading sequence is modified so that in the next series of load
increments the folded sheet is "rolled" by moving one free edge relative
to the other.  This process is illustrated in Fig. 3-27.
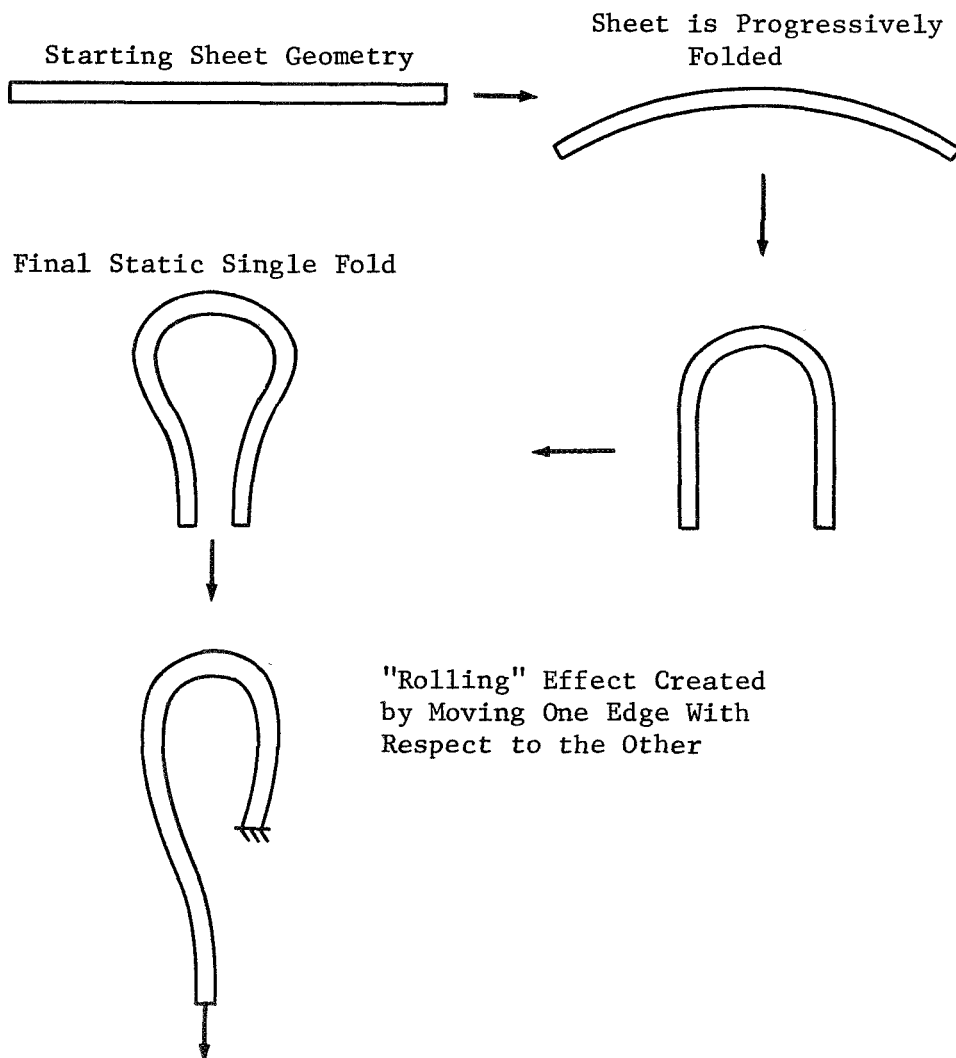


Figure 3-27 - Simulating Rolling Fold

The information stored on tape or disk is necessary to start the "rolling" process, since the pre-rolling stresses and geometry must be considered in the finite element model.

This task was not emphasized herein, although the computer program can perform the above mentioned analysis. Rather, the rolling <u>double fold</u>, which creates a much more severe environment for the bladder, was modeled in detail using a procedure similar to that of Fig. 3-27. This analysis is described in detail in a latter section.

## III.9.0 Task 2.6: Estimate Fatigue Life of Single Folds

In this section, the method coded into the finite element plane strain computer program to estimate fatigue life cycles to failure N after plastic folding strains have been computed is reviewed. These computations lean heavily upon the methods of Sections II and III.5.

Since almost all fatigue tests are uniaxial in nature, whereas the state of strain in a folded bladder is multiaxial, a method for converting the multiaxial strains into equivalent uniaxial strains is necessary. This is accomplished herein using Eq. (2.9). The result is an equivalent plastic strain at each node of the finite element model, computed at the completion of each load increment. A search over all nodes is conducted in order to locate the maximum equivalent plastic strain $e_p$. This strain is next used to compute fatigue life N from Eq. (2.7), which can be re-arranged as

$$N = \left( \frac{e_p}{M_i} \right)^{1/z_i} \qquad (3.143)$$

where $M_i$ and $z_i$ are constants for material $i$, computed as described below.

The quantities $M_i$ and $z_i$ can be obtained by the program in two different ways. In one method, the user may input these numbers directly after having computed $M_i$ and $z_i$ by the methods of Section II.2.2.1.1, or by any other means at his disposal. Alternately, these quantities can be computed by the program by using a "least-squares" fit to data input to the program. Noting that log-log plots of $e_p$ versus N for most materials are straight, or nearly straight, lines motivated the least-squares computation for $M_i$ and $z_i$. For example, assume that the user inputs $e_{p1}$ and $e_{p2}$, and correspondign $N_1$ and $N_2$ (obtained from fatigue tests). If Eq. (3.143) is valid, then

$$\ell u\ e_{p_1} = \ell u\ M_i + z_i\ \ell u\ N_1$$

$$\ell u\ e_{p_2} = \ell u\ M_i + z_i\ \ell u\ N_2 \qquad (3.144)$$

Solving Eq. (3.144) for $M_i$ and $z_i$ gives

$$M_i = EXP \; \frac{\ell u N_2 \; \ell u e_{P_1} - \ell u N_1 \; \ell u e_{P_2}}{\ell u \dfrac{N_2}{N_1}} \qquad (3.145a)$$

$$z_i = \frac{\ell u \dfrac{e_{P_2}}{e_{P_1}}}{\ell u \dfrac{N_2}{N_1}} \qquad (3.145b)$$

By following a similar line of reasoning, if the user wishes to input values $e_{P_1}$, $e_{P_2}$, ... $e_{P_n}$ and corresponding $N_1$, $N_2$, ... $N_n$, a least-squares fit gives

$$M_i = EXP \; \frac{[\sum_{j=1}^{n}(\ell u \, N_j)^2][\sum_{j=1}^{n}\ell u \, e_{P_j}] - [\sum_{j=1}^{n}\ell u \, N_j][\sum_{j=1}^{n}\ell u \, e_{P_j} \, \ell u \, N_j]}{n\sum_{j=1}^{n}(\ell u \, N_j)^2 - (\sum_{j=1}^{n}\ell u \, N_j)^2} \qquad (3.146a)$$

$$z_i = \frac{n\sum_{j=1}^{n}\ell u e_{P_j} \, \ell u \, N_j - [\sum_{j=1}^{n}\ell u \, N_j][\sum_{j=1}^{n}\ell u \, e_{P_j}]}{n\sum_{j=1}^{n}(\ell u \, N_j)^2 - (\sum_{j=1}^{n}\ell u \, N_j)^2} \qquad (3.146b)$$

Note that for n=2, Eqs. (3.146) reduce to Eqs. (3.145). To illustrate the program, and its use for folding fatigue life calculations, several example problems are presented in the next section.

III.9.1  Fatigue Examples

Two different materials, teflon and aluminum, were used in the sample single fold fatigue life calculations. Table 3-5 gives the fatigue information for each material, and the original source. The purpose of this study was to investigate the sensitivity of the life cycle predictions

Table 3-5  Uniaxial Fatigue Data

| Material | $\varepsilon_{p_1}$ (%) | $N_1$ | $\varepsilon_{p_2}$ (%) | $N_2$ | M | z | Source |
|---|---|---|---|---|---|---|---|
| Aluminum | 28 | 10 | 18 | $10^4$ | .916 | -.515 | Table 2-1 |
| Teflon | 81 | 10 | 55 | $10^3$ | .983 | -.085 | Table 2-2 |

to variations in material properties and finite element model geometry.
The thickness of all bladders considered was t = 0.02". Table 3-6 gives
the results of this investigation.

Table 3-6

| Material | Time (sec.) | No. Layer | Length (in.) | D.O.F. | E (KSI) | $\mu$ | $\sigma_y$ (KSI) | $E_p$ (KSI) | $R_t/t$ | $e_p$ (%) | N |
|---|---|---|---|---|---|---|---|---|---|---|---|
| Teflon | 62 | 1 | .06 | 42 | 7 | .35 | 2 | 0 | 1.43 | 6.97 | Large |
| Aluminum | 69 | 1 | .06 | 42 | 200 | .33 | 10 | 33 | 1.59 | 16.05 | 29 |
| Aluminum | 103 | 1 | .04 | 30 | 10000 | .33 | 6 | 1400 | 1.18 | 21.04 | 17 |
| Aluminum | 244 | 2 | .02 | 50 | 10000 | .33 | 6 | 0 | 1.53 | 28.74 | 10 |
| Aluminum | 138 | 1 | .06 | 42 | 10000 | .33 | 6 | 0 | 5.70 | 7.21 | 140 |
| Aluminum | 108 | 1 | .04 | 30 | 10000 | .33 | 6 | 0 | 1.18 | 19.65 | 24 |
| Aluminum | 46 | 1 | .02 | 18 | 10000 | .33 | 6 | 0 | 1.41 | 17.00 | 26 |

The second column in this table gives the CDC 6500 computer running time.
The third column gives the number of finite element layers through the
.02" thickness, and column four shows the length of the model. The next
column lists the number of displacement degrees-of-freedom in the finite
element model. The tenth column shows the ratio of the final inner radius
to the thickness, denoting the severity of the fold. The last two columns
give the maximum equivalent plastic strain in percent, and estimated
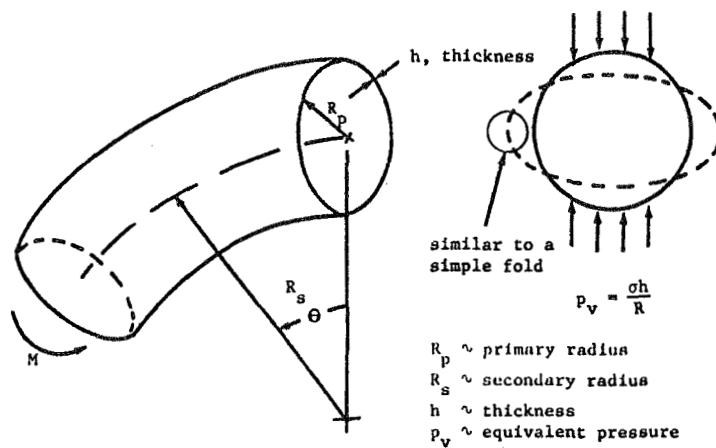folding fatigue life.

Several conclusions can be made from the results of Table 3-6.
First, the fatigue life of the aluminum bladders is relatively insensitive
to material properties and finite element model mesh. The life is, how-
ever, strongly dependent on the sharpness $(R_t/t)$ of the final folding
radius. Secondly, the teflon bladder has an almost indefinite fatigue life.
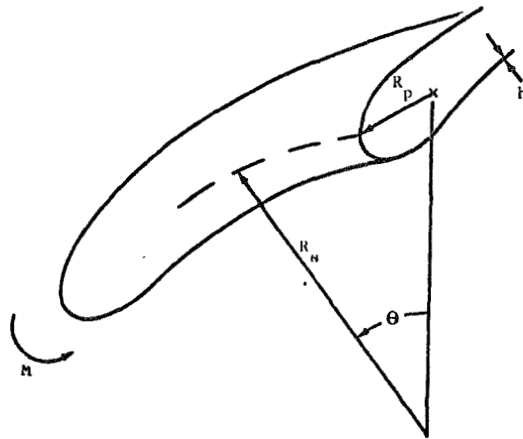
IV.0   TASK 3.0:   DOUBLE FOLD ANALYSIS

The double fold (Figure 1-1) is observed to occur during expulsion of bladders. This fold is formed by applying either compressive loads or moments along the length of a simple fold until local buckling occurs. In other words, the double fold can be visualized as a buckled simple fold. Before outlining the method for determining strains in double folds, the basic physical behavior of such folds will first be discussed. In the discussion which follows, the term "primary fold radius, $R_p$," refers to the radius of the simple fold in the buckled region of the sheet (see Fig. 1-1). Similarly, the "secondary fold radius, $R_s$," refers to the radius of the double fold in the buckled region.

To obtain some insight into the behavior of the double fold, a piece of mylar was doubly-folded and studied under a microscope. This simple experimental study took less than an hour to perform yet contributed significantly to an understanding of the double fold. It is experiments of this type which have been used to guide the analysis and point the way to simplifying approximations for the mathematical model. The major effect observed in this experimental study was that the primary fold radius $(R_p)$ is reduced to nearly zero when a simple fold is bent to form a double fold. This effect shows the appearance of yielding zones due to high tensile stresses which relate to the primary fold radius.

The reason that the primary fold radius is reduced when the sheet is doubly-folded can be readily explained, since the physical problem is analogous to the behavior of a toroidal shell acted upon by bending loads (See Reference 58). Figure 4-1 shows a portion of a toroidal shell being subjected to a bending moment; the analogous bladder problem is a simple fold that is being doubly-folded. From this figure, it can be seen that the circled region of the torus corresponds to the primary fold in the doubly-folded sheet. Similarly, the large radius of the torus is equivalent to the secondary fold radius of the sheet. It is reasonable to expect that the doubly-folded sheet will deform in a manner similar to the bent torus.

h, thickness

R
P
x

R
s

θ

M

similar to a
simple fold

$P_v = \dfrac{\sigma h}{R}$

$R_p \sim$ primary radius
$R_s \sim$ secondary radius
$h \sim$ thickness
$P_v \sim$ equivalent pressure

A. Bending of a Torus

R
P
x

h

R
H

θ

M

B. Bending of a Simple Fold to Form a Double Fold

Figure 4-1 Bending of a Torus and a Double Fold

Then the torus is subjected to bending moments, the cross-section of
the torus tends to flatten out, as shown by the dotted line in Figure 4-1.
This flattening action takes place because the stresses caused by the
bending moment give rise to force components which act in the plane of the
torus cross-section. Reissner (Reference 58) has shown that these force
components are equivalent to pressure forces which act in the vertical
direction and tend to flatten the cross-section. The pressure is related
to the bending stress by the relation

$$P_v = \frac{\sigma h}{R_s} \qquad\qquad (4.1)$$

where h is the thickness of the torus, $R_s$ is the radius of curvature of

the bent torus, and $\sigma$ is the stress due to the applied bending moment. Note that $\sigma$ is positive (tension) on the top portion of the cross-section (away from the center of curvature)and $\sigma$ is negative on the bottom half (compression). Thus, the equivalent pressure $p_v$ acts as shown in Figure 4-1 to flatten out the cross section.

In a similar manner, bending of a simple fold to form a double fold gives rise to equivalent pressure forces which cause the primary fold radius to become very small. The cross-section of the simple fold becomes flattened out, just as in the case of the torus. Thus we can conclude that the radius of the primary fold is dependent upon the stresses and curvature of the secondary fold.

Reissner's study (Reference 58) was performed for the case when the torus is considered to be a thin shell (i.e., where $h/R_s \ll 1$ and $R_p \ll R_s$). Consequently, Reissner assumed that the radius of curvature, R, of the bent torus is the same for every point on the cross-section. For the double fold problem, however, this assumption is not valid. In fact, one can show that the different radii of curvature (for different points on the cross-section of the primary fold) lead to an upward resultant force that causes a rubber sheet to bend upward when it is doubly folded.


In Reference 5 this upward deformation was attributed solely to anti-clastic behavior (Poisson's ratio), and no mention was made of the mechanism described here. The proof that this upward bending is not due to anticlastic effects can be seen from the rubber sheet. On the right half side of the sheets, anticlastic effects do occur, and a small upward bending is noted. On the doubly-folded side, a much larger deflection occurs. If the vertical deformation of the double fold was due solely to anticlastic effects, one would expect the deflections on the left and right to be nearly equal. Thus it appears that only a small part of the upward deflection of a double fold is due to anticlastic behavior.

From the preceding observations, including the analogy with the bending of a torus, a method for analyzing strains in a stationary double fold becomes apparent. The finite element technique (similar to the method proposed for simple folds) can be applied. In studying the simple fold,

the basic triangular element is taken to be infinite in length (normal to the paper) and a plane strain analysis results. For the double fold study, however, a ring-shaped triangular element will be employed. This element is simply a circular ring with a triangular cross-section, and it is commonly used to analyze axisymmetric bodies (Figure 4-2).

Simple tests on Mylar specimens shown that in the neighborhood of the double fold, plane sections (in the $\theta$ = constant direction, Figure 4-2) remain very nearly plane. In fact, the $\theta$ = 0 plane is a plane of symmetry, so it cannot deform. Thus, in the immediate locality of the double fold (where the strains are a maximum) the stresses and strains are independent of the angle $\theta$. In this case, the equations of equilibrium become identical to those for an axisymmetric problem, i.e.,

$$\frac{\partial \sigma_r}{\partial r} + \frac{\partial \tau_{rx}}{\partial x} + \frac{\sigma_r - \sigma_\theta}{r} = 0$$

and

$$\frac{\partial \tau_{rx}}{\partial r} + \frac{\partial \sigma_x}{\partial x} + \frac{\tau_{rx}}{r} = 0$$

(4.2)

where  x  is the axial coordinate

   r  is the radial coordinate

and   $\theta$  is the circumferential coordinate

Note that r is related to $R_s$, the secondary fold radius. The finite element model and the coordinate system are shown in Figure 4-2.

With the assumption that plane sections remain plane in the vicinity of the fold, it thus becomes clear that the double fold problem can be analyzed. The finite element technique outlined here will be used to include large deformation effects and nonlinear material properties. It is recognized, however, that the assumption of plane sections may break down when the secondary radius $R_s$ becomes very small (i.e., when $R_s$ < h, the thickness). In this case, the planes ($\theta$ = constant) may deform, and the shear strain $\gamma_{r\theta}$ may become important.
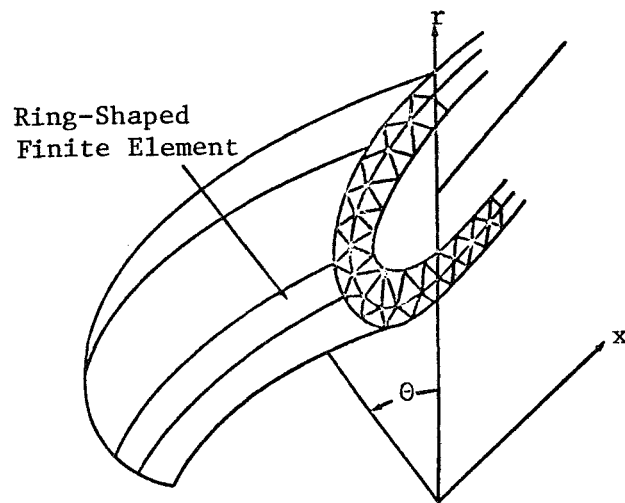
Figure 4-2.    Finite Element Idealization of a Double Fold

The axisymmetric finite element used herein for double fold analysis is a direct outgrowth of the plane strain element presented earlier.  Both the strains and material properties are assumed to vary linearily with the element.  The detailed derivation of the elemental characteristics are given in the following sections, and represent a significant contribution to the state-of-the-art in axisymmetric finite element analysis.

## IV.1    Task 3.1:    Axisymmetric Finite Element Model

As in the plane strain analysis, two alternative derivations for the six node axisymmetric finite element are given herein.  The first derivation follows Reference 39, and introduces approximations which simplify the analysis.  The second derivation is more rigorous and is used to assess the accuracy of the first formulation.  The coordinate system for both formulations is given in Figure 3-6, in which r replaces x, z replaces y, and w replaces v.

### IV.1.1   Derivation Following Felippa

In the following formulation, the hoop strain $\varepsilon_\theta$ is assumed to vary linearly over the element.  This approximation greatly simplifies the elemental area integrations, and will be discussed in a subsequent section.

The convention stiffness is derived from Equation (3.99a), in which [B] is redefined

$$[B] = \begin{bmatrix} [U] & | & [0] \\ \hline [0] & | & [V] \\ \hline [R] & | & [0] \\ \hline [V] & | & [U] \end{bmatrix} \qquad (12 \times 12)$$

(4.3a)

where [U] and [V] are given by Equations (3.99c) and (3.99d) and

$$[R] = \begin{bmatrix} 2A/r_1 & 0 & 0 & 0 & 0 & 0 \\ 0 & 2A/r_2 & 0 & 0 & 0 & 0 \\ 0 & 0 & 2A/r_3 & 0 & 0 & 0 \end{bmatrix}$$

(4.3b)

and is due to the hoop strains.  In Equation (4.3b), $r_i$ is the radius to corner nodal circle i.

4-6

The matrix [N] is given by

$$[N] = \frac{2\pi}{72A}
\begin{bmatrix}
[N_{11}] & [N_{12}] & [N_{13}] & [N_{14}] \\
& [N_{22}] & [N_{23}] & [N_{24}] \\
& & [N_{33}] & [N_{34}] \\
\text{SYM.} & & & [N_{44}]
\end{bmatrix}$$

(4.4a)

The elements of the (3 x 3) submatrices $[N_{ij}]$ are given by Equation (3.102a) and

$$n_{11}^{ij} = \{ (12r_1+3r_2+3r_3) \quad (3r_1+2r_2+r_3) \quad (3r_1+r_2+2r_3)\}\{c^{(k)}\}$$

$$n_{12}^{ij} = \{ (3r_1+2r_2+r_3) \quad (2r_1+3r_2+r_3) \quad (r_1+r_2+r_3)\}\{c^{(k)}\}$$

$$n_{13}^{ij} = \{ (3r_1+r_2+2r_3) \quad (r_1+r_2+r_3) \quad (2r_1+r_2+3r_3)\}\{c^{(k)}\}$$

$$n_{22}^{ij} = \{ (2r_1+3r_2+r_3) \quad (3r_1+12r_2+3r_3) \quad (r_1+3r_2+2r_3)\}\{c^{(k)}\}$$

$$n_{23}^{ij} = \{ (r_1+r_2+r_3) \quad (r_1+3r_2+2r_3) \quad (r_1+2r_2+3r_3)\}\{c^{(k)}\}$$

$$n_{33}^{ij} = \{ (2r_1+r_2+3r_3) \quad (r_1+2r_2+3r_3) \quad (3r_1+3r_2+12r_3)\}\{c^{(k)}\}$$

(4.4b)

where Equation (3.102c) gives $\{c^{(k)}\}$, and Section II.5.4 gives the particular $c_{iijj}^{(k)}$.

The geometric stiffness matrix is given as

$$[K^{(G)}] = 
\begin{bmatrix}
[K_{G_1}] & [0] \\
[0] & [K_{G_2}]
\end{bmatrix}$$
(12 x 12)     (4.5a)

$$[K_{G_1}] = \begin{bmatrix} [U]^T & | & [V]^T & | & [R]^T \end{bmatrix} \begin{bmatrix} [J_r] & | & [J_{rz}] & | & [0] \\ \hline [J_{rz}] & | & [J_z] & | & [0] \\ \hline [0] & | & [0] & | & [J_\theta] \end{bmatrix} \begin{bmatrix} [U] \\ \hline [V] \\ \hline [R] \end{bmatrix} \qquad (4.5b)$$

$$[K_{G_2}] = \begin{bmatrix} [U]^T & | & [V]^T \end{bmatrix} \begin{bmatrix} [J_r] & | & [J_{rz}] \\ \hline [J_{rz}] & | & [J_z] \end{bmatrix} \begin{bmatrix} [U] \\ \hline [V] \end{bmatrix} \qquad (4.5c)$$

The $[J_i]$ matrices, for $i = r, z, \theta$, and $rz$ are

$$[J_i] = \frac{2\pi}{5040A} \left\{ \begin{bmatrix} (36r_1 + 3r_2 + 3r_3) & (3r_1 - 2r_2 - r_3) & (3r_1 - r_2 - 2r_3) \\ & (-2r_1 - 9r_2 - 3r_3) & (-r_1 - 3r_2 - 3r_3) \\ \text{SYM.} & & (-2r_1 - 3r_2 - 9r_3) \end{bmatrix} (\sigma_i)_1 \right.$$

$$+ \begin{bmatrix} (-9r_1 - 2r_2 - 3r_3) & (-2r_1 + 3r_2 - r_3) & (-3r_1 - r_2 - 3r_3) \\ & (3r_1 + 36r_2 + 3r_3) & (-r_1 + 3r_2 - 2r_3) \\ \text{SYM.} & & (-3r_1 - 2r_2 - 9r_3) \end{bmatrix} (\sigma_i)_2$$

$$+ \begin{bmatrix} (-9r_1 - 3r_2 - 2r_3) & (-3r_1 - 3r_2 - r_3) & (-2r_1 - r_2 + 3r_3) \\ & (-3r_1 - 9r_2 - 2r_3) & (-r_1 - 2r_2 + 3r_3) \\ \text{SYM.} & & (3r_1 + 3r_2 + 36r_3) \end{bmatrix} (\sigma_i)_3$$

$$+ 4 \begin{bmatrix} (12r_1 + 6r_2 + 3r_3) & (6r_1 + 6r_2 + 2r_3) & (3r_1 + 2r_2 + 2r_3) \\ & (6r_1 + 12r_2 + 3r_3) & (2r_1 + 3r_2 + 2r_3) \\ & & (2r_1 + 2r_2 + 3r_3) \end{bmatrix} (\sigma_i)_4$$

$$+4 \begin{bmatrix} (3r_1 + 2r_2 + 2r_3) & (2r_1 + 3r_2 + 2r_3) & (2r_1 + 2r_2 + 3r_3) \\ & (3r_1 + 12r_2 + 6r_3) & (2r_1 + 6r_2 + 6r_3) \\ & & (3r_1 + 6r_2 + 12r_3) \end{bmatrix} (\sigma_i)_5$$

$$+4 \begin{bmatrix} (12r_1 + 3r_2 + 6r_3) & (3r_1 + 2r_2 + 2r_3) & (6r_1 + 2r_2 + 6r_3) \\ & (2r_1 + 3r_2 + 2r_3) & (2r_1 + 2r_2 + 3r_3) \\ & & (6r_1 + 3r_2 + 12r_3) \end{bmatrix} (\sigma_i)_6 \Bigg\}$$

<div align="right">(4.6)</div>

where $(\sigma_i)_j$ is evaluated at node j.

The load vector for uniform pressure is

$$\Delta f_1 = \frac{2\pi}{6} r_1 (\Delta P_2 b_2 + \Delta P_3 b_3)$$
$$\Delta f_2 = \frac{2\pi}{6} r_2 (\Delta P_1 b_1 + \Delta P_3 b_3)$$
$$\Delta f_3 = \frac{2\pi}{6} r_3 (\Delta P_1 b_1 + \Delta P_2 b_2)$$
$$\Delta f_4 = \frac{2\pi}{3} (r_1 + r_2) \Delta P_3 b_3 \tag{4.7}$$
$$\Delta f_5 = \frac{2\pi}{3} (r_2 + r_3) \Delta P_1 b_1$$
$$\Delta f_6 = \frac{2\pi}{3} (r_1 + r_3) \Delta P_2 b_2$$

where the last six components are obtained from Equation (4.7) by replacing $b_i$ with $a_i$. The other part of the residual vector (neglecting body forces) can be computed using the shape functions, giving, for a quadratic stress variation,

<div align="center">4-9</div>

$$\varepsilon_1 = \frac{2\pi r_1}{6} (P_2 b_2 + P_3 b_3) - \frac{2\pi}{360} \{b_1 \ 0 \ 0\}[W_1]\{\sigma_r\}$$

$$- \frac{2\pi}{360} \{a_1 \ 0 \ 0\}[W_1]\{\tau_{rz}\} - \frac{2\pi A}{720} \{\frac{1}{r_1} \ 0 \ 0\}[W_2]\{\sigma_\theta\}$$

$$\varepsilon_2 = \frac{2\pi r_2}{6} (P_1 b_1 + P_3 b_3) - \frac{2\pi}{360} \{0 \ b_2 \ 0\}[W_1]\{\sigma_r\}$$

$$- \frac{2\pi}{360} \{0 \ a_2 \ 0\}[W_1]\{\tau_{rz}\} - \frac{2\pi A}{720} \{0 \ \frac{1}{r_2} \ 0\}[W_2]\{\sigma_\theta\}$$

$$\varepsilon_3 = \frac{2\pi r_3}{6} (P_1 b_1 + P_3 b_3) - \frac{2\pi}{360} \{0 \ 0 \ b_3\}[W_1]\{\sigma_r\}$$

$$- \frac{2\pi}{360} \{0 \ 0 \ a_3\}[W_1]\{\tau_{rz}\} - \frac{2\pi A}{720} \{0 \ 0 \ \frac{1}{r_3}\}[W_2]\{\sigma_\theta\}$$

$$\varepsilon_4 = \frac{2\pi}{3} (r_1 + r_2) P_3 b_3 - \frac{2\pi}{360} \{b_2 b_1 \ 0\}[W_2]\{\sigma_r\}$$

$$- \frac{2\pi}{360} \{a_2 \ a_1 \ 0\}[W_2]\{\tau_{rz}\}$$

$$\varepsilon_5 = \frac{2\pi}{3} (r_2 + r_3) P_1 b_1 - \frac{2\pi}{360} \{0 \ b_3 \ b_2\}[W_2]\{\sigma_r\}$$

$$- \frac{2\pi}{360} \{0 \ a_3 \ a_2\}[W_2]\{\tau_{rz}\}$$

$$\varepsilon_6 = \frac{2\pi}{3} (r_1 + r_3) P_2 b_2 - \frac{2\pi}{360} \{b_3 \ 0 \ b_2\}[W_2]\{\sigma_r\}$$

$$- \frac{2\pi}{360} \{a_3 \ 0 \ a_1\}[W_2]\{\tau_{rz}\} \tag{4.8}$$

where

$$\{\sigma_r\}^T = \{\sigma_{r_1} \ \sigma_{r_2} \ \sigma_{r_3} \ \sigma_{r_4} \ \sigma_{r_5} \ \sigma_{r_6}\} \tag{4.9}$$

etc., and $\sigma_{r_i}$ is evaluated at node i. The last three elements are obtained from Equation (4.8) by using $\{\sigma_{rz}\}$ in place of $\{\sigma_r\}$ and $\{\sigma_z\}$ in place of $\{\sigma_{rz}\}$.

The matrices $[W_1]$ and $[W_2]$ are

$$[W_1] = \begin{bmatrix} (18r_1+3r_2+3r_3) & (-5r_1-6r_2-r_3) & (-5r_1-r_2-6r_3) \\ (-6r_1-5r_2-r_3) & (3r_1+18r_2+3r_3) & (-r_1-5r_2-6r_3) \\ (-6r_1-r_2-5r_3) & (-r_1-6r_2-5r_3) & (3r_1+3r_2+18r_3) \end{bmatrix}$$

$$\begin{bmatrix} (24r_1+8r_2+4r_3) & (4r_1-8r_2-8r_3) & (24r_1+4r_2+8r_3) \\ (8r_1+24r_2+4r_3) & (4r_1+24r_2+8r_3) & (-8r_1+4r_2-8r_3) \\ (-8r_1-8r_2+4r_3) & (4r_1+8r_2+24r_3) & (8r_1+4r_2+24r_3) \end{bmatrix} \quad (4.10a)$$

$$[W_2] = \begin{bmatrix} 24r_1 & (-8r_1-4r_3) & (-8r_1-4r_2) \\ (-8r_2-4r_3) & 24r_2 & (-4r_1-8r_2) \\ (-4r_2-8r_3) & (-4r_1-8r_3) & 24r_3 \end{bmatrix}$$

$$\begin{bmatrix} (48r_1+32r_2+16r_3) & (16r_1+16r_2+16r_3) & (48r_1+16r_2+32r_3) \\ (32r_1+48r_2+16r_3) & (16r_1+48r_2+32r_3) & (16r_1+16r_2+16r_3) \\ (16r_1+16r_2+16r_3) & (16r_1+32r_2+48r_3) & (32r_1+16r_2+48r_3) \end{bmatrix} \quad (4.10b)$$

Some preliminary computer results for a thick axisymmetric cylindrical shell indicate that the element described above produces numerical results that are slightly in error. It is felt that the error is caused by assuming the internal hoop strain varies linearily over the element, i.e.,

$$\varepsilon_\theta = \xi_1 \frac{u_1}{r_1} + \xi_2 \frac{u_2}{r_2} + \xi_3 \frac{u_3}{r_3} \tag{4.11a}$$

This assumption considerably simplified the volume integrations over each element. However, to be consistent with the assumed displacements, the strain should be

$$\varepsilon_\theta = \frac{\xi_1 (2\xi_1-1)u_1 + \xi_2(2\xi_2-1)u_2 + \xi_3(2\xi_3-1)u_3 + 4\xi_1\xi_2 u_4 + 4\xi_2\xi_3 u_5 + 4\xi_1\xi_3 u_6}{\xi_1 r_1 + \xi_2 r_2 + \xi_3 r_3} \tag{4.11b}$$

which is obviously not linear in the coordinates $\xi_i$. Using Equation (4.11b) would lead to integrals which would be very difficult to evaluate in closed form.

To attempt to reduce the error noted above, another assumption was tried for the hoop strain, namely

$$\varepsilon_\theta = \xi_1(2\xi_1-1) \frac{u_1}{r_1} + \xi_2(2\xi_2-1) \frac{u_2}{r_2} + \xi_3(2\xi_3-1) \frac{u_3}{r_3}$$

$$+ 4\xi_1\xi_2 \frac{u_4}{r_4} + 4\xi_2\xi_3 \frac{u_5}{r_5} + 4\xi_1\xi_3 \frac{u_6}{r_6} \tag{4.11c}$$

This allows a quadratic strain variation by interpolating on all nodal strain components. However, there was very little difference in the results obtained by using Equation (4.11c) in place of (4.11a). Therefore, the final coding is based upon the simplier assumption, Equation (4.11a).

## IV.1.1.1    Modeling and Loading Double Fold

In studying the double fold, an axisymmetric finite element model is intended.   A sketch of the model is shown in Figure 4-3.
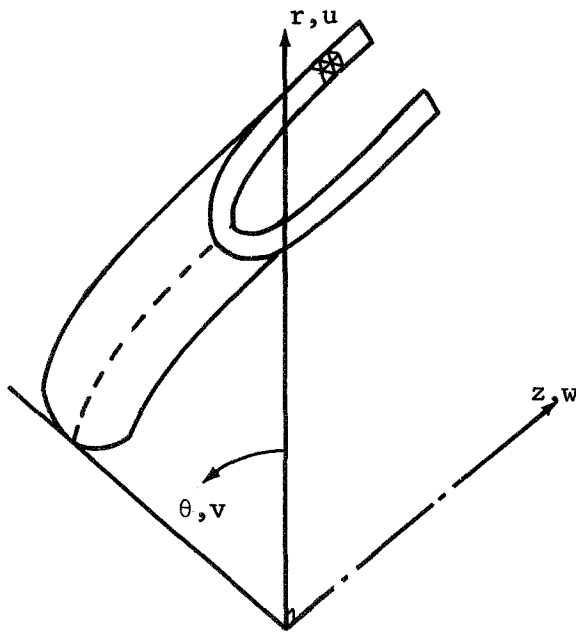


The co-ordinate directions are r, Θ , and z, with the corresponding displacements u, v, and w.

Figure 4-3   Axisymmetric Finite Element Model

In order to completely specify the problem, it is necessary to apply the proper boundary conditions and to define the applied loading.   It is the purpose of this section to discuss these loading and boundary conditions and to show how they will be incorporated in the finite element model.

## IV.1.1.1.1    Boundary Conditions

In specifying the double fold problem, the following boundary conditions will be applied:

(a) Along the plane $z = $ constant $= z_o$

$$\sigma_{zz} = 0 \text{ (no normal stress)}$$

$$\tau_{rz} = 0 \text{ (no shear stress)}$$

These boundary stresses will be input directly to the finite element program. In addition, since the problem is axisymmetric, we will also have $\tau_{\theta z} = 0$ along $z = z_o$.

(b) Along the plane $\theta = 0$

$v = 0$ (no circumferential displacement)

$\sigma_{\theta\theta} \neq 0$

u, w free (no restriction on these displacements)

(c) Along the outer surface $r = r_{outer}(z)$

$$\left. \begin{array}{l} \sigma_{rr} = 0 \\ \\ \tau_{rz} = 0 \end{array} \right\} \quad \text{no stresses applied}$$

These boundary stresses will be input directly to the finite element program; since the problem is axisymmetric, we will also have $\tau_{r\theta} = 0$ along this outer surface.

(d) Along the inner surface, $r = r_{inner}(z)$

$$\left. \begin{array}{l} \sigma_{rr} = 0 \\ \\ \tau_{rz} = 0 \end{array} \right\} \quad \text{no stresses applied}$$

These boundary stresses will be input directly as in part (c) above; again $\tau_{r\theta} = 0$ along this surface.

(e) Along the plane $\theta = $ constant $= \theta_o$,

u, w free (no restriction on these displacements)

$$\sigma_{\theta\theta} \neq 0$$

$$\int \sigma_{\theta\theta} dA = \iint \sigma_{\theta\theta} \, drdz = F_\theta = 0 \quad \text{(no net force in the } \theta -$$
$$\text{direction)}$$

$$\int \sigma_{\theta\theta} r dA = \iint \sigma_{\theta\theta} r drdz = \vec{M}_z \quad \text{(moment about the z - axis)}$$

$$\int \sigma_{\theta\theta} z dA = \iint \sigma_{\theta\theta} z drdz = \vec{M}_r = 0 \quad \text{(no net moment about a}$$
$$\text{radial line in the plane}$$
$$\theta = \theta_o)$$

These boundary conditions can be satisfied by the axisymmetric finite element model. The zero stress conditions can be met directly by the model, but it is necessary to investigate $\vec{M}_r$, $\vec{M}_z$, and $F_\theta$ further. These boundary forces will be discussed in the sections which follow.

IV.1.1.1.2    Satisfying the Boundary Conditions on $\theta = \theta_o$

To demonstrate that $\int \sigma_{\theta\theta} \, dA = 0$, consider the following:

For an axisymmetric body, the equilibrium equations are (Ref. 8)

$$\frac{\partial \sigma_{rr}}{\partial r} + \frac{\partial \tau_{rz}}{\partial z} + \frac{\sigma_{rr} - \sigma_{\theta\theta}}{r} - 0 \qquad (4.12a)$$

and

$$\frac{\partial \tau_{rz}}{\partial r} + \frac{\partial \sigma_{zz}}{\partial z} + \frac{\tau_{rz}}{r} = 0 \qquad (4.12b)$$

Solving equation (4.12a) for $\sigma_{\theta\theta}$, we can write

$$\int \sigma_{\theta\theta} dA = \iint \left[ \frac{\partial}{\partial r} \left( r\sigma_{rr} \right) + \frac{\partial}{\partial z} \left( r\tau_{rz} \right) \right] drdz$$

Integrating these terms gives

$$\int \sigma_{\theta\theta} dA = \int \left[ r\sigma_{rr} \Big|_{r = r_{inner}}^{r = r_{outer}} \right] dz + \int \left[ r\tau_{rz} \Big|_{z_1}^{z_2} \right] dr \qquad (4.13)$$

where the inner and outer radii are shown in Figure 4-4 along with $z_1$ and $z_2$.

By considering the boundary conditions $\sigma_{rr}\Big|_{r = r_{outer}} = 0,$

$\sigma_{rr}\Big|_{r = r_{inner}} = 0$, etc. of Section IV.1.1.1.1
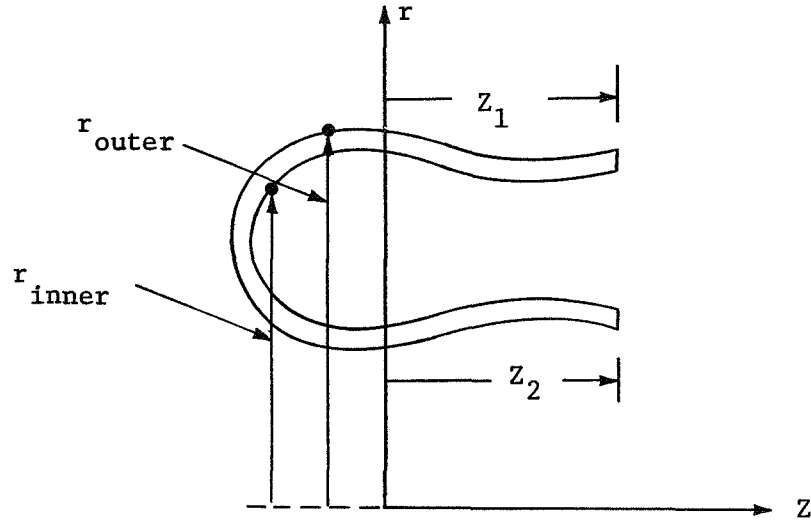


Figure 4-4 — Integration Limits

it is apparent that the boundary integrals vanish indentically in equation (4.13), giving $\int \sigma_{\theta\theta} dA = 0$.

In a similar fashion, one can show that $\vec{M}_r = 0$.

For example,

$$\vec{M}_r = \int \sigma_{\theta\theta} z dA = \iint z \left[ \frac{\partial}{\partial r}\left( r\sigma_{rr} \right) + \frac{\partial}{\partial z}\left( r\tau_{rz} \right) \right] dr dz$$

$$= \int \left[ zr\sigma_{rr} \Big|_{r = r_{inner}}^{r = r_{outer}} \right] dz + \int \left[ zr\tau_{rz} \Big|_{z_1}^{z_2} \right] dr$$

$$- \iint r\tau_{rz} dr dz$$

where the second term has been integrated by parts. As before, $\sigma_{rr} = 0$ on the boundary, and $\tau_{rz} = 0$ at $z_1$ and $z_2$. Thus we have

$$\vec{M}_r = - \iint r\tau_{rz} dr dz \qquad\qquad (4\text{-}14)$$

4-16

Using equation (4.12b) for $\tau_{rz}$, we have

$$-\iint r\tau_{rz}\,drdz = \iint r\left[r\,\frac{\partial \tau_{rz}}{\partial r} + r\,\frac{\partial \sigma_{zz}}{\partial z}\right]drdz$$

$$=\int\left\{r^2\sigma_{zz}\Big|_{z_1}^{z_1}\right\}dr +\int\left\{r^2\tau_{rz}\Bigg|_{r_{inner}}^{r_{outer}}\right\}dz$$

$$-\iint 2r\,\tau_{rz}\,drdz$$

where an integration by parts has been done. Transposing terms and using the boundary conditions on $\sigma_{zz}$ and $\tau_{rz}$ gives

$$\iint r\tau_{rz}\,drdz = 0$$

and from equation (4.14), we have $\vec{M}_r = 0$.

From the final integral, for $\vec{M}_z$, we have $\iint \sigma_{\theta\theta}r\,drdz = \vec{M}_z \neq 0$ which will be applied loading term. The method in which $\vec{M}_z$ is determined is discussed in the next section.


IV.1.1.1.3  Loading in Axisymmetric Model

In applying loads to the axisymmetric finite element model, it is necessary to consider what specific load-deformation information is desired. As a first approach to the problem, one would like to know the relationship between the secondary fold radius, $R_s$ and the primary fold radius, $R_p$. To generate this relationship, $R_s$ can be incrementally changed and the corresponding value or $R_p$ can be calculated. The method in which $R_s$ will be varied and $R_p$ determined is outlined in the following paragraphs.

Consider a ring-shaped axisymmetric finite element that has some initial curvature and a corresponding initial strain (see Fig. 4-5).
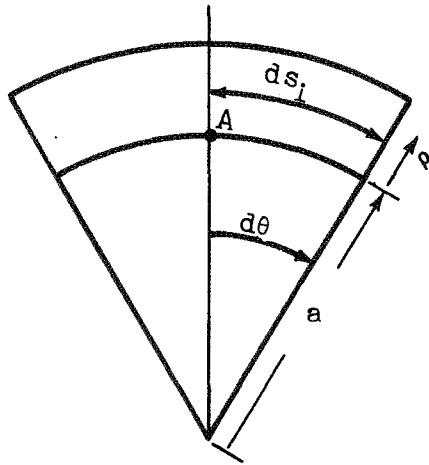
Note that a is the inside radius of curvature, and $\rho$ is measured from the inner surface. The length of any fiber in the initial state is given by

$$ds_i = (a + \rho)d\theta \qquad (4.15)$$

Figure 4-5 - Initially Curved Finite Element

Now we want to change the radius of curvature to a new value, call it R. After this change, the element will still be axisymmetric (i.e., constant curvature in the $\theta$ - direction) but it will have a new curvature (see Fig. 4-6).
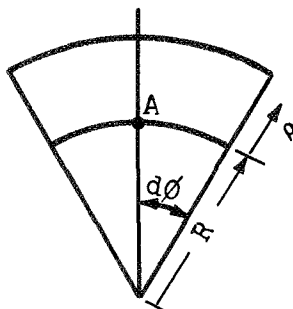


Figure 4-6 - Finite Element After Change in Curvature

In going from the initial state (figure 4-5) to the final state Fig. (4-6), incremental displacements $\Delta u$ and $\Delta v$ are involved. These incremental displacements contain rigid body motions which can be determined by fixing some element reference point before and after the deformation. One choice of a reference point is to make the center of curvature coincide before and after the deformation. This choice involves large rigid-body motions and is undesirable.

A more convenient reference choice is to fix point A (Fig. 4-5 and 4-6) and allow the center of curvature to move. The distortion of the element is most easily visualized as the combination of two separate motions. First, the element is deformed as shown in Figure 4-7. This deformation is taken such that the length of arc of the inner surface remains constant; in other words, the inner arc length is

$$L_i = ad\Theta = Rd\emptyset \qquad\qquad (4.16)$$

The displacements associated with this deformation are of the form

$$\Delta u = K(1 - \cos\Theta)$$
$$\Delta v = Cr\Theta + K \sin\Theta$$

Where the K terms are rigid body motion and $Cr\Theta$ represents a uniform circumferential strain. Note for this first deformation, $ds = (R + \rho)d\emptyset$.
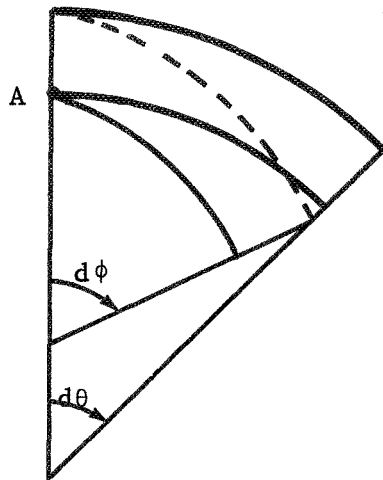
Figure 4-7 — First Part of the Deformation

Now a second deformation is allowed, namely a uniform radial contraction of $\Delta u$ (see Fig. 4-8).
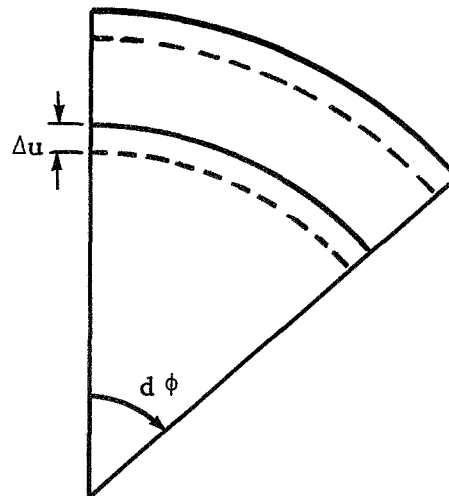
Figure 4-8 — Second Part of the Deformation — Uniform Radial Contraction

With these two deformations combined, the length of a fiber is given by

$$ds = (R + \rho + \Delta u)d\phi \qquad (4.17)$$

after the deformation. Thus the incremental circumferential strain can be computed as

$$\Delta\varepsilon_\theta = \frac{ds - ds_i}{ds_i} = \frac{(R + \rho + \Delta u)d\phi - (a + \rho)d\theta}{(a + \rho)d\theta} \qquad (4.18)$$

From equation (4.16) we have $\frac{d\phi}{d\theta} = \frac{a}{R}$ which can be substituted into Equation (4.18) to yield

$$\Delta\varepsilon_\theta = \frac{\rho\left(\frac{1}{R} - \frac{1}{a}\right)}{(1 + \rho/a)} + \frac{\Delta u}{R(1 + \rho/a)} \qquad (4.19)$$

$$\Delta\varepsilon_\theta = (\Delta\varepsilon_\theta)_1 + (\Delta\varepsilon_\theta)_2$$

In going from the initial state (with radius of curvature a) to the final state (with radius R) the strain increment $(\Delta\varepsilon_\theta)_1$ will be specified completely. That is, a, R, and $\rho(r,z)$ will all be specified input items that are known. The only unknown will be $\Delta u(r,z)$, and that will be determined by the finite element method.

Once $\Delta u(r,z)$ is known, $\Delta\varepsilon_\theta$ can be computed and then the stress increment, $\Delta\sigma_{\theta\theta}$, can be calculated from the stress-strain relations. Finally, it is possible to determine the corresponding moment increment, $\Delta\vec{M}_z$, from the integral

$$\Delta\vec{M}_z = \iint \Delta\sigma_{\theta\theta} r\,dr\,dz$$

Thus it appears possible to generate a plot of $\vec{M}_z$ vs. $\frac{1}{R}$ (moment vs. curvature) for the double-fold problem. In addition, the total displacements u and w can be used to give the primary radius of curvature, $R_p$ at each value of $\frac{1}{R}$. In this manner, the desired result of $\frac{1}{R}$ vs $R_p$ will be obtained.

## IV.1.2. Alternate Axisymmetric Finite Element Formulation

In this section, an alternate formulation is presented in which no simplifying assumption concerning the hoop strain distribution is made. Results using this element can then be compared with those using the element of the previous section in order to estimate the magnitude of the errors introduced by the assumptions of Section IV.1.1.

Figure 4-9 shows the coordinate system for the six nodal circle triangular torus element. The displacements are taken as

$$u(r,z) = A_1 + A_2 r + A_3 z + A_4 r^2 + A_5 rz + A_6 z^2$$

$$w(r,z) = A_7 + A_8 r + A_9 z + A_{10} r^2 + A_{11} rz + A_{12} z^2 \tag{4.20}$$

If Eq. (4.20) is evaluated for both u and w at the six nodal points, the result can be written as

$$\left\{ \begin{array}{c} u_i \\ \hline w_i \end{array} \right\} = \left[ \begin{array}{c|c} [m] & [0] \\ \hline [0] & [m] \end{array} \right] \{A\} \tag{4.21a}$$

or

$$\{v_i\} = [M]\{A\} \tag{4.21b}$$

where

$$\{v_i\}^T = \left\{ \begin{array}{c} u_i \\ \hline w_i \end{array} \right\}^T = \left\{ u_1 \ u_2 \ u_3 \ u_4 \ u_5 \ u_6 \mid w_1 \ w_2 \ w_3 \ w_4 \ w_5 \ w_6 \right\}$$

$$\{A\}^T = \left\{ A_1 \ A_2 \ A_3 \ A_4 \ A_5 \ A_6 \mid A_7 \ A_8 \ A_9 \ A_{10} \ A_{11} \ A_{12} \right\} \tag{4.21c}$$

and $u_i$ and $w_i$ are the displacements of node i.

Inverting Eq. (4.21b) gives

$$\{A\} = \left[ \begin{array}{c|c} [m]^{-1} & [0] \\ \hline [0] & [m]^{-1} \end{array} \right] \left\{ \begin{array}{c} u_i \\ \hline w_i \end{array} \right\} = [M]^{-1}\{v_i\} \tag{4.22a}$$
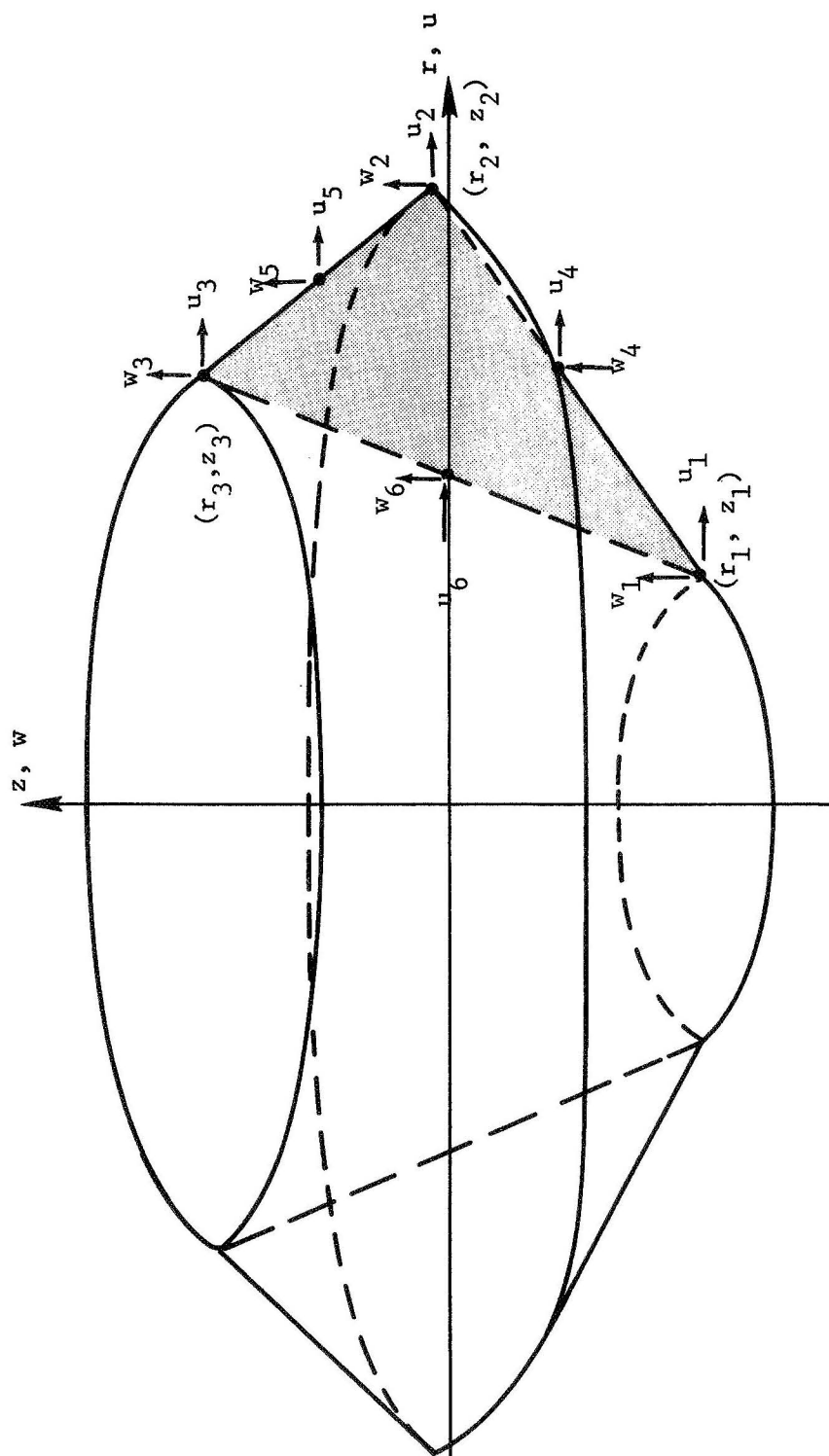
Figure 4-9 – Triangular Torus Element

4-22

where

$$4A^2[m]^{-1} =$$

$$
\begin{bmatrix}
4A_{23}(2A_{23}-A) & 4A_{31}(2A_{31}-A) & 4A_{12}(2A_{12}-A) & 16A_{23}A_{31} & 16A_{31}A_{12} & 16A_{23}A_{12} \\
2b_1(4A_{23}-A) & 2b_2(4A_{31}-A) & 2b_3(4A_{12}-A) & 8(A_{31}b_1+A_{23}b_2) & 8(A_{12}b_2+A_{31}b_3) & 8(A_{12}b_1+A_{23}b_3) \\
2a_1(4A_{23}-A) & 2a_2(4A_{31}-A) & 2a_3(4A_{12}-A) & 8(A_{31}a_1+A_{23}a_2) & 8(A_{12}a_2+A_{31}a_3) & 8(A_{12}a_1+A_{23}a_3) \\
2b_1^2 & 2b_2^2 & 2a_3^2 & 4b_1b_2 & 4b_2b_3 & 4b_1b_3 \\
4b_1a_1 & 4b_2a_2 & 4b_3a_3 & 4(b_2a_1+b_1a_2) & 4(b_3a_2+b_2a_3) & 4(b_3a_1+b_1a_3) \\
2a_1^2 & 2a_2^2 & 2a_3^2 & 4a_1a_2 & 4a_2a_3 & 4a_1a_3
\end{bmatrix}
$$

(4.22b)

and

$$2A_{12}=r_1z_2-r_2z_1 \qquad 2A_{23}=r_2z_3-r_3z_2 \qquad 2A_{31}=r_3z_1-r_1z_3$$

$$b_1=z_2-z_3 \qquad b_2=z_3-z_1 \qquad b_3=z_1-z_2$$

$$a_1=r_3-r_2 \qquad a_2=r_1-r_3 \qquad a_3=r_2-r_1$$

(4.22c)

$$2A = 2A_{12} + 2A_{23} + 2A_{31} = a_2b_1 - a_1b_2$$

In the above expressions, $r_i$ and $z_i$ are the coordinates of node i, and A is the cross sectional area of the torus.

The linear strain-displacement equations for axisymmetric analysis are

$$e_r = \frac{\partial u}{\partial r} \qquad e_z = \frac{\partial w}{\partial z}$$

$$e_\theta = \frac{u}{r} \qquad \gamma_{rz} = \frac{\partial u}{\partial z} + \frac{\partial w}{\partial r}$$

(4.23)

4-23

Computing the strains by using Eq. (4.20) in Eq. (4.23) yields

$$
\left\{
\begin{array}{c}
e_r \\
e_z \\
e_\theta \\
\gamma_{rz}
\end{array}
\right\}
=
\left[
\begin{array}{cccccc|cccccc}
0 & 1 & 0 & 2r & z & 0 & 0 & 0 & 0 & 0 & 0 & 0 \\
0 & 0 & 0 & 0 & 0 & 0 & 0 & 0 & 1 & 0 & r & 2z \\
\frac{1}{r} & 1 & \frac{z}{r} & r & z & \frac{z^2}{r} & 0 & 0 & 0 & 0 & 0 & 0 \\
0 & 0 & 1 & 0 & r & 2z & 0 & 1 & 0 & 2r & z & 0
\end{array}
\right]
\{A\}
\qquad (4.24a)
$$

or
$$\{e(r,z)\} = [N(r,z)]\{A\} \qquad (4.24b)$$

For an elastic isotropic material, the stress-strain relations are

$$
\left\{
\begin{array}{c}
\sigma_r \\
\sigma_z \\
\sigma_\theta \\
\sigma_{rz}
\end{array}
\right\}
=
\frac{E}{(1+\mu)(1-2\mu)}
\left[
\begin{array}{cccc}
(1-\mu) & \mu & \mu & 0 \\
\mu & (1-\mu) & \mu & 0 \\
\mu & \mu & (1-\mu) & 0 \\
0 & 0 & 0 & (\frac{1}{2}-\mu)
\end{array}
\right]
\left\{
\begin{array}{c}
e_r \\
e_z \\
e_\theta \\
\gamma_{r2}
\end{array}
\right\}
\qquad (4.25a)
$$

or symbolically

$$\{\sigma(r,z)\} = [E]\{e(r,z)\} \qquad (4.25b)$$

Where E is Young's Modulus and $\mu$ is Poisson's Ratio.

The stiffness matrix can be derived from potential energy to give

$$[k] = ([M]^{-1})^T [K][M]^{-1} \qquad (4.26)$$

and

$$[K] = \int_{vol.} [N(r,z)]^T [E][N(r,z)]\, r\, dr\, dz\, d\theta \qquad (4.27)$$

can be considered as the elemental stiffness matrix in {A} coordinates.

4-24

After carrying out the matrix multiplication indicated in Eq. (4.27) several integrations must be performed. These integrals are listed below for completeness.

$$A = \int drdz = \frac{1}{2} (r_1 z_2 - r_2 z_1 + r_2 z_3 - r_3 z_2 + r_3 z_1 - r_1 z_3)$$

$$\lambda_1 = \int r drdz = \frac{A}{3} (r_1 + r_2 + r_3)$$

$$\lambda_3 = \int r^2 drdz = \frac{A}{6} (r_1^2 + r_2^2 + r_3^2 + r_1 r_2 + r_1 r_3 + r_2 r_3)$$

$$\lambda_5 = \int r z drdz = \frac{A}{12} (2 r_1 z_1 + r_2 z_1 + r_3 z_1 + r_1 z_2 + 2 r_2 z_2$$

$$+ r_3 z_2 + r_1 z_3 + r_2 z_3 + 2 r_3 z_3)$$

$$\lambda_6 = \int r^3 drdz = \frac{A}{10} (r_1^3 + r_1 r_2^2 + r_1 r_3^2 + r_1^2 r_2 + r_1^2 r_3 \qquad (4.28)$$

$$+ r_1 r_2 r_3 + r_2^3 + r_2 r_3^2 + r_2^2 r_3 + r_3^3)$$

$$\lambda_7 = \int r^2 z drdz = \frac{A}{30} (3 r_1^2 z_1 + r_2^2 z_1 + r_3^2 z_1 + 2 r_1 r_2 z_1 + 2 r_1 r_3 z_1$$

$$+ r_2 r_3 z_1 + 2 r_1 r_2 z_2 + r_1^2 z_2 + r_1 r_3 z_2 + 3 r_2^2 z_2 + r_3^2 z_2$$

$$+ 2 r_2 r_3 z_2 + 2 r_1 r_3 z_3 + r_1^2 z_3 + r_1 r_2 z_3 + 2 r_2 r_3 z_3 + r_2^2 z_3 + 3 r_3^2 z_3)$$

The quantities $\lambda_2 = \int z drdz$, $\lambda_4 = \int z^2 drdz$, $\lambda_8 = \int r z^2 drdz$, and $\lambda_9 = \int z^3 drdz$ can be derived from the corresponding expressions in Eq. (4.28) by substituting z for r, and $z_i$ for $r_i$.

By defining the following variables, the remaining integrations can be carried out,

$$c_1 = - \frac{2A_{12}}{a_3} \qquad\qquad s_1 = - \frac{b_3}{a_3}$$

$$c_2 = - \frac{2A_{23}}{a_1} \qquad\qquad s_2 = - \frac{b_1}{a_1} \qquad (4.29)$$

$$c_3 = - \frac{2A_{31}}{a_2} \qquad\qquad s_3 = - \frac{b_2}{a_2}$$

where Eqs. (4.22c) gives the $a_i$, $b_i$, and $A_{ij}$. Note that when $r_i = r_j$, for either $i = 3$, $j = 2$, or $i = 1$, $j = 3$, or $i = 2$, $j = 1$, some of the quantities in Eqs. (4.29) become indeterminant. From physical reasoning, the terms can be set to zero. For example, when $a_3 = r_2 - r_1 = 0$, then $c_1 = s_1 = 0$. The integrals are

$$\lambda_{10} = \int \frac{1}{r}\, drdz = -\left[ c_1 \ln \frac{r_2}{r_1} + s_1 a_3 \right]$$

$$-\left[ c_2 \ln \frac{r_3}{r_2} + s_2 a_1 \right] - \left[ c_3 \ln \frac{r_1}{r_3} + s_3 a_2 \right]$$

$$\lambda_{11} = \int \frac{z}{r}\, drdz = -\left[ \frac{1}{2} c_1^2 \ln \frac{r_2}{r_1} - c_1 b_3 - \frac{1}{4} s_1 b_3 (r_2 + r_1) \right]$$

$$-\left[ \frac{1}{2} c_2^2 \ln \frac{r_3}{r_2} - c_2 b_1 - \frac{1}{4} s_2 b_1 (r_3 + r_2) \right]$$

$$-\left[ \frac{1}{2} c_3^2 \ln \frac{r_1}{r_3} - c_3 b_2 - \frac{1}{4} s_3 b_2 (r_1 + r_3) \right]$$

$$\lambda_{12} = \int \frac{z^2}{r}\, drdz = -\left[ \frac{1}{3} c_1^3 \ln \frac{r_2}{r_1} - c_1^2 b_3 - \frac{1}{2} c_1 s_1 b_3 (r_1 + r_2) \right.$$

$$\left. - \frac{1}{9} s_1^2 b_1 (r_3^2 + r_3 r_2 + r_2^2) \right] + \frac{1}{9} s_1^2 b_3 (r_1^2 + r_1 r_2 \qquad + r_2^2) - \frac{1}{3} c_2^3 \ln \frac{r_3}{r_2}$$

$$-\left[ \frac{1}{3} c_3^3 \ln \frac{r_1}{r_3} - c_3^2 b_2 - \frac{1}{2} c_3 s_3 b_2 (r_1 + r_3) \right.$$

$$\left. - \frac{1}{9} s_3^2 b_2 (r_1^2 + r_1 r_3 + r_3^2) \right] + c_2^2 b_1 + \frac{1}{2} c_2 s_2 b_1 (r_2 + r_3)$$

$$\lambda_{13} = \int \frac{z^3}{r}\,drdz =$$

$$-\frac{1}{4}c_1^{\,4}\ln\frac{r_2}{r_1} + b_3\left[c_1^{\,3} + \frac{3}{4}c_1^{\,2}s_1(r + r_2) + \frac{1}{3}c_1 s_1^{\,2}(r_2^{\,2} + r_2 r_1 + r_1^{\,2})\right.$$

$$\left. + \frac{1}{16}s_1^{\,3}(r_1 + r_2)(r_1^{\,2} + r_2^{\,2})\right] - \frac{1}{4}c_2^{\,4}\ln\frac{r_3}{r_2}$$

$$+ b_1\left[c_2^{\,3} + \frac{3}{4}c_2^{\,2}s_2(r_3 + r_2) + \frac{1}{3}c_2 s_2^{\,2}(r_3^{\,2} + r_3 r_2 + r_2^{\,2})\right.$$

$$\left. + \frac{1}{16}s_2^{\,3}(r_2 + r_3)(r_2^{\,2} + r_3^{\,2})\right] - \frac{1}{4}c_3^{\,4}\ln\frac{r_1}{r_3}$$

$$+ b_2\left[c_3^{\,3} + \frac{3}{4}c_3^{\,2}s_3(r_1 + r_3) + \frac{1}{3}c_3 s_3^{\,2}(r_1^{\,2} + r_1 r_3 + r_3^{\,2})\right.$$

$$\left. + \frac{1}{16}s_3^{\,3}(r_1 + r_3)(r_1^{\,2} + r_3^{\,2})\right]$$

$$\lambda_{14} = \int \frac{z^4}{r}\,drdz = -\frac{1}{5}\left(c_1^{\,5}\ln\frac{r_2}{r_1} + c_2^{\,5}\ln\frac{r_3}{r_2} + c_3^{\,5}\ln\frac{r_1}{r_3}\right)$$

$$+ (c_1^{\,4}b_3 + c_2^{\,4}b_1 + c_3^{\,4}b_2)$$

$$- \left[c_1^{\,3}s_1^{\,2}(r_2^{\,2} - r_1^{\,2}) + c_2^{\,3}s_2^{\,2}(r_3^{\,2} - r_2^{\,2}) + c_3^{\,3}s_3^{\,2}(r_1^{\,2} - r_3^{\,2})\right]$$

$$- \frac{2}{3}\left[c_1^{\,2}s_1^{\,3}(r_2^{\,3} - r_1^{\,3}) + c_2^{\,2}s_2^{\,3}(r_3^{\,3} - r_2^{\,3}) + c_3^{\,2}s_3^{\,3}(r_1^{\,3} - r_3^{\,3})\right]$$

$$- \frac{1}{4}\left[c_1 s_1^{\,4}(r_2^{\,4} - r_1^{\,4}) + c_2 s_2^{\,4}(r_3^{\,4} - r_2^{\,4}) + c_3 s_3^{\,4}(r_1^{\,4} - r_3^{\,4})\right]$$

$$- \frac{1}{25}\left[s_1^{\,5}(r_2^{\,5} - r_1^{\,5}) + s_2^{\,5}(r_3^{\,5} - r_2^{\,5}) + s_3^{\,5}(r_1^{\,5} - r_3^{\,5})\right] \tag{4.30}$$

In a similar manner, the load vector consistent with Eq. (4.26) e.g. for a constant normal pressure, can be derived. Letting $P_i$ be the pressure normal to the side opposite corner node i (positive in compression), the components of the force vector $\{F\}$ become

$$F_1 = \frac{2\pi r_1}{6} (P_2 b_2 + P_3 b_3)$$

$$F_2 = \frac{2\pi r_2}{6} (P_1 b_1 + P_3 b_3)$$

$$F_3 = \frac{2\pi r_3}{6} (P_1 b_1 + P_2 b_2)$$

$$F_4 = \frac{2\pi}{3} (r_1 + r_2) P_3 b_3 \qquad\qquad (4.31)$$

$$F_5 = \frac{2\pi}{3} (r_1 + r_3) P_1 b_1$$

$$F_6 = \frac{2\pi}{3} (r_2 + r_3) P_2 b_2$$

Components 7 through 12 of $\{F\}$ can be derived from components 1 through 6, respectively, by replacing the $b_i$ by $a_i$.

## IV.1.3  Comparison of Formulations

In this section, numerical results from the two formulations of Section IV.1.1 (Linear and Quadratic Hoop Strains) and the formulation of IV.1.2 are compared.

The example problems were all thick cylinders loaded by an internal pressure. The number of elements used to represent a cross section of the cylinder was varied from 24 elements, 12 elements, and 6 elements. The layout of the elements is shown in Figure 4-10. Nodes 1, 2, and 3 lie on the inner surface, and their displacements (which should be identical) can be used as a measure of accuracy. Table 4-1 shows some typical results of this study. Note that for course meshes, the variation of displacements at nodes 1, 2, and 3 is considerable, and the average displacement is also slightly in error. Note also that the quadratic hoop strain assumption did not improve the accuracy of the solution as expected.

```
                                    z                          Cylinder
                                    ↑
                                    |        r = .16"
Constrained                         |        r = .25"
from moving                         |
in the z            P = 365 PSI
direction.          Internal Pressure                              r

         E = 20,000,000 PSI            μ = .49
```
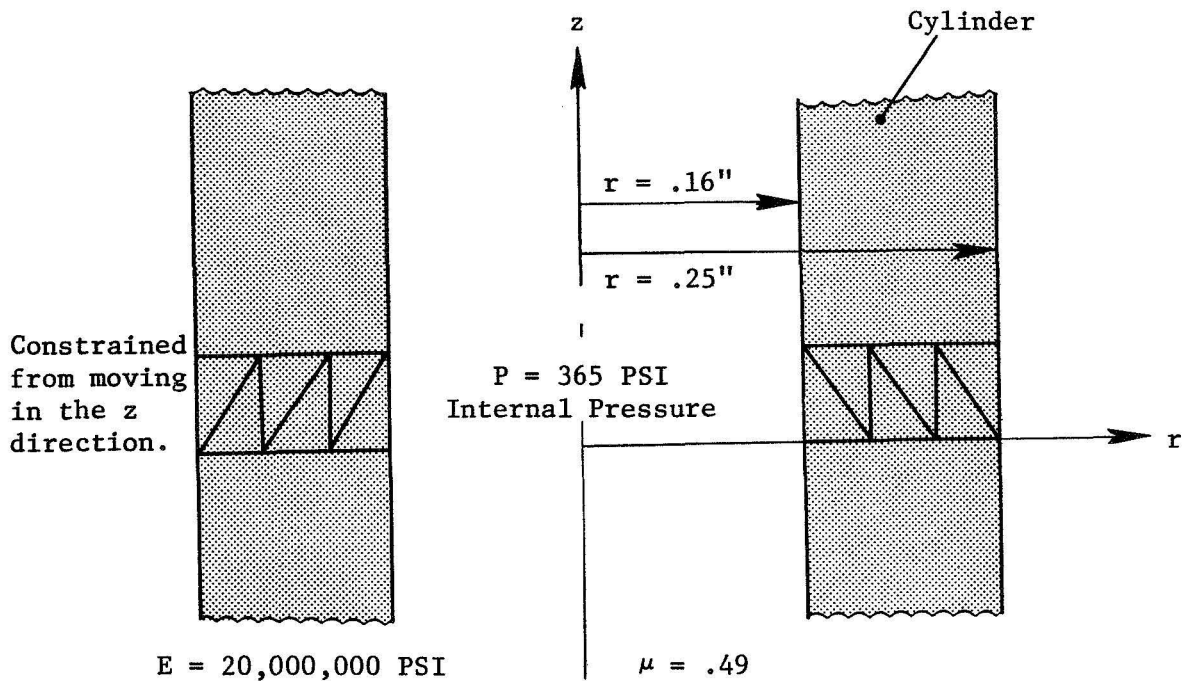
Figure 4-10 - Cylinder Problem - 6 Element Mesh

Table 4-1 - Example Problem

| Model | Linear Hoop Strain Element (IV.1.1) | | | | Quadratic Hoop Strain Element (IV.1.1) | | | |
|---|---|---|---|---|---|---|---|---|
| Number of Elements | Radial Displ. (in.) x $10^{-6}$ | | | | Radial Displ., (in.) x $10^{-6}$ | | | |
| | Node 1 | Node 2 | Node 3 | Ave. | Node 1 | Node 2 | Node 3 | Ave. |
| 24 | 7.4170 | 7.4270 | 7.4229 | 7.4223 | 7.4168 | 7.4268 | 7.4227 | 7.4221 |
| 12 | 7.3809 | 7.4204 | 7.4047 | 7.4020 | 7.3807 | 7.4202 | 7.4045 | 7.4018 |
| 6 | | | | | 7.3413 | 7.3900 | 7.2446 | 7.3253 |
| Closed Form Solution | | | | 7.429 | | | | 7.429 |

| | Alternate Formulation (IV.1.2) | | | |
|---|---|---|---|---|
| 6 | 7.4287 | 7.4293 | 7.4209 | 7.4263 |
| 8 | 7.4294 | 7.4297 | 7.4257 | 7.4283 |

Due to the simplicity of the linear hoop strain derivation, this formulation will be used for all bladder folding studies. Errors introduced by this formulation are not significant, as can be seen from Table 4-1.

## IV.1.3  Axisymmetric Finite Element-Numerical Examples

In order to check-out the coding for the axisymmetric finite element program, a variety of example problems were considered during the course of the contract.  These problems exhibited a wide range of nonlinear behavior, including plastic response, large deflections, large strains, and a combination of material and geometric nonlinearities.  An example double fold was also simulated.

### IV.1.3.1  Elasto-Plastic Cylinder

To verify the theory presented herein for problems in which the nonlinear behavior is due to plasticity, a long cylinder subjected to internal pressure was considered.  This example was used by Ref. 49 in a finite element solution.  The cylinder had the following characteristics:

| | |
|---|---|
| Inner Radius | $a = 1.0"$ |
| Outer Radius | $b = 2.0"$ |
| Elastic Modulus | $E = 10,000$ ksi |
| Poisson's Ratio | $\mu = 0.3$ |
| Yield Stress in Tension | $\sigma_y = 20$ ksi |
| Post Yield Modulus | $E_p = 0$ |

where $\sigma_y$ is the uniaxial yield stress.

A slice between two $z$ = constant planes was modeled with 24 of the new axisymmetric finite elements.  The condition of zero strain in the axial direction was satisfied by constraining boundary nodes from moving in that direction.  A total internal pressure load of 15 ksi was applied in 5 equal increments, with the corrective iteration mentioned above applied after each step.

Some typical results are shown in Figures 4-11a and 4-11b.  Figure 4-11a is a load-deflection curve, and it shows the nonlinear nature of the problem.  The solid line is from Ref. 55 for the Von Mises yield criterion, the Prandtl-Reuss flow law, zero axial strain, and elastic and plastic compressibility (Curve A of Ref. 55).  The finite element solution simulates all these conditions, and is shown in Figures 4-11 as solid dots.  Figure 4-11b gives the radial stress distribution through the thickness of the
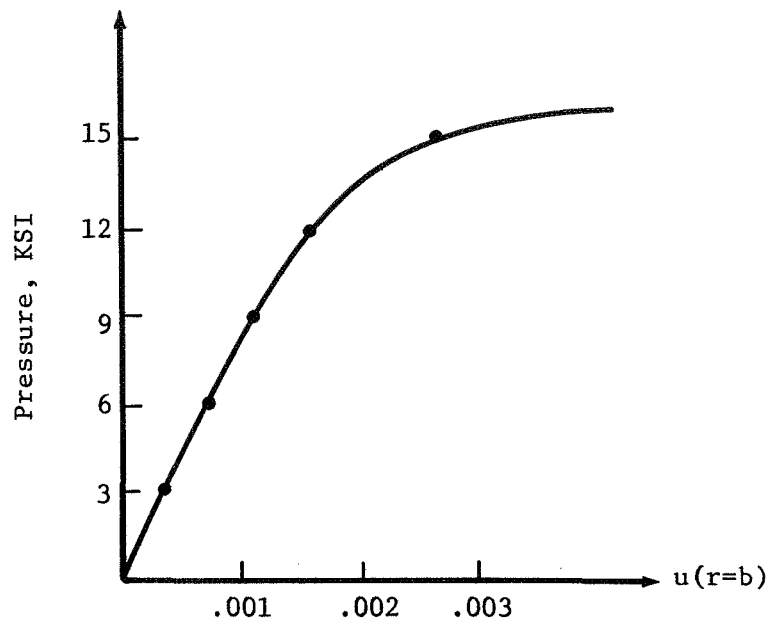
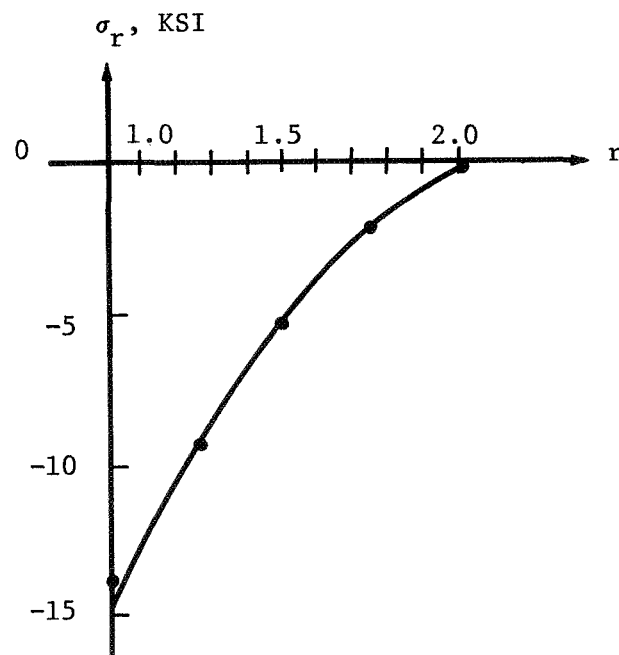Figure 4-11a  — Radial Deflection at r=b vs. Load



Figure 4-11b  — Radial Stress vs. Radius at a Load of 15 KSI

cylinder for a load of 15 ksi. Both of these figures show excellent agreement between the solution of Ref. 55 and the finite element theory presented herein.

IV.1.3.2 Large Deflection Circular Plate

A circular plate h = .5" thick and having a radius a = 10" was used to investigate the application of the new element and theory to large deflection-moderate strain problems. Only elastic behavior was allowed, with

$$E = 30,000 \text{ ksi}$$
$$\mu = 0.3.$$

Thirty-two axisymmetric elements were employed to model the simple-supported plate. A total uniform pressure of q = 1.25 ksi was applied in 10 equal increments, with corrective cycling after each load step.

Figure 4-12 shows a load versus center-line deflection curve for this problem, with the solid lines from Ref. 31, and the dots from the finite element solution. The straight line represents the linear small deflection solution, while the curved line is for the large deflection solution. As can be seen from this figure, the finite element results closely follow the "exact" solution of Ref. 31.

IV.1.3.3 Large Strain Sheet Bending

Hill (Ref. 30) presents a problem, under the general theory of sheet bending, which can be used to check the capability of the theory and element presented herein to analyze situations in which large plastic strains occur. The problem is that of plastic bending of a wide sheet into a cylindrical surface by couples applied along opposite edges.

By assuming that (1) plane sections remain plane during bending, (2) elastic deformation can be neglected, (3) the material is perfectly plastic, and (4) the Tresca yield criterion holds, Section III.1 gives a closed-form expression for the plastic hoop strain in the sheet as a function of folding radius of curvature. This same problem was solved by the finite element procedure by modeling the sheet with 24 elements through its
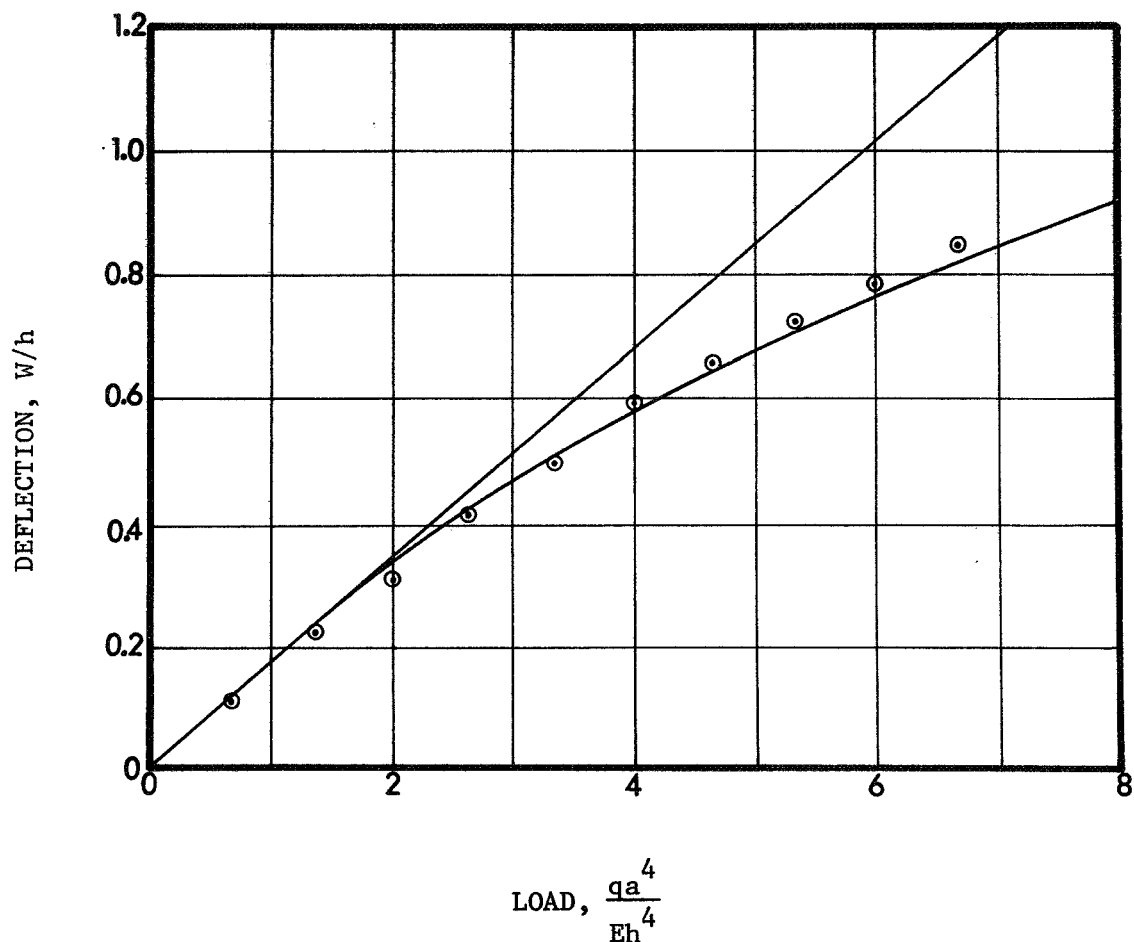
Figure 4-12 - Load Versus Deflection for Circular Plate

its thickness. The finite element model was "loaded" by specifying the
change in the radius of curvature. An arbitrarily large inner radius of
100" was used to start the computations. This radius was then decreased
until yielding first occurred in the sheet. The sheet was then "loaded"
further by reducing the radius from its value at first yield to essentially
zero in nine equal increments. The physical constants for the problem
were

$$E = 10,000 \text{ ksi}$$

$$\mu = 0.33$$

$$\sigma_y = 6 \text{ ksi}$$

$$E_p = 0$$

$$t(\text{sheet thickness}) = 0.02"$$

The plastic hoop strains computed at the inner radius of the sheet by both methods are shown in Table 4-2. Considering the various differences between the finite element solution and the analytical solution, the results agree very well over a wide range of radii of curvature. Note that strains on the order of 15% developed during the solution.

Table 4-2 - Plastic Hoop Strains Computed for Various Inner Radii

| Inner Radius (inches) | Percent Plastic Hoop Strain | |
|---|---|---|
| | Finite Element | Closed Form |
| 13.38 | 0.0 | 0.0 |
| (radius to first yield) | | |
| 11.90 | -0.00944 | -0.00929 |
| 10.42 | -0.0217 | -0.0212 |
| 8.94 | -0.0380 | -0.0371 |
| 7.46 | -0.0608 | -0.0593 |
| 5.98 | -0.0945 | -0.0924 |
| 4.50 | -0.1498 | -0.1473 |
| 3.02 | -0.2586 | -0.2559 |
| 1.54 | -0.5757 | -0.5725 |
| 0.0587 | -13.910 | -15.66 |

Note that the axisymmetric solution to the single folding problem given above yields results closer to those of the analytical model of Section III.1 than does the plane strain solution of Section III.5.10.2. This is due to the fact that the axisymmetric model simulated the analytical solution better than the plane strain model in that plane sections remain plane in the axisymmetric model, whereas planes are distorted in the solution of Section III.5.10.2. The very close agreement between the analytical solution and the numerical solution shown in Table 4-2 give added confidence in both approaches.

IV.1.3.4  Torus Problem

In order to check out the capability of the axisymmetric finite element program to simulate double folds, a simple torus problem was considered. The torus had a major radius $R_s$, a minor radius $R_p$, and a wall thickness

of t. The torus was loaded by couples applied to its section, as shown in Figure 4-13a.

The torus problem was considered by Reissner (Ref. 58) for the case in which the response is elastic, and $(R_p/R_s) << 1$. Table 4-3 tabulates the moment M for various changes in $R_s$ for the case in which E = 10,000 KSI, $\mu = .3$, $R_s$ = 100" (initially), $R_p$ = 10" (initially), and t = 1".

<div align="center">

Table 4-3

Moment vs. Radius

</div>

| $R_s$ (inches) 100 | M (K-in.) (Reissner) | M (K-in.) (Finite Element) |
|---|---|---|
| 99 | 1941 | 2056 |
| 98 | 3961 | 4115 |
| 97 | 6003 | 6177 |
| 96 | 8088 | 8241 |
| 95 | 10216 | 10307 |
| 94 | 12389 | 12374 |
| 93 | 14610 | 14442 |
| 92 | 16878 | 16511 |
| 91 | 19197 | 18579 |
| 90 | 21567 | 20647 |

Note that Reissner's solution predicts that the cross-section of the torus deforms as shown by the dotted lines in Fig. 4-13b. Thus the double fold problem is very similar to the torus problem, in which $R_p$ is the first fold (primary) radius, and $R_s$ is the second fold (secondary) radius. The flattening of the torus is also similar to the way a double fold would deform as $R_s$ is decreased. However, for a true double fold, the cross section would not necessarily be symmetric about B-B (Fig. 4-13b).

One-half of the torus cross-section was modeled with 72 triangular finite elements (only half was considered due to the symmetry about B-B). The boundaries of the model were constrained to slide along B-B. The finite element mesh involved 370 degrees-of-freedom. The model was "loaded" by specifying $\Delta R_s$, and the moment M to cause this radius change was computed by integrating the stresses over the cross section. In this solution, $R_s$
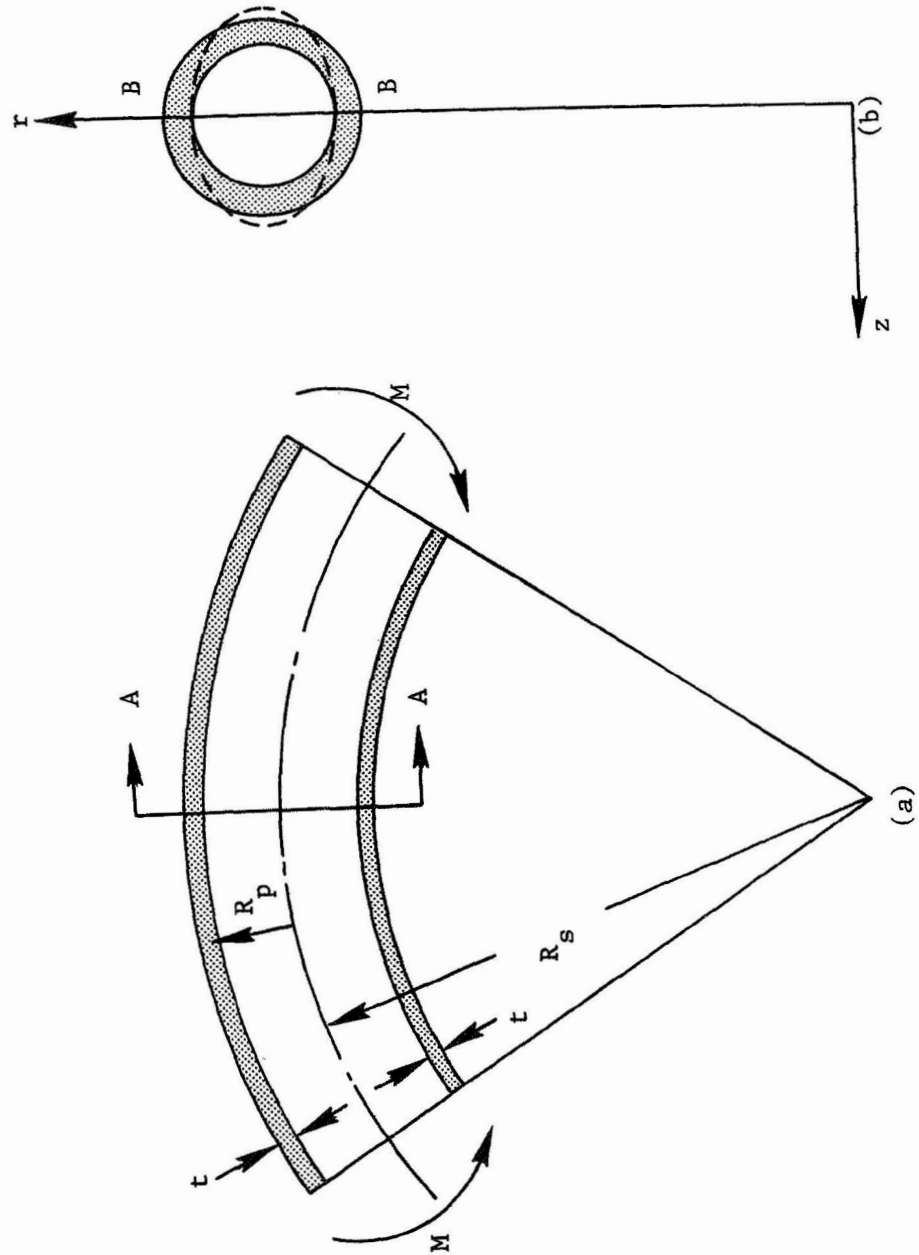
Figure 4-13 – Torus Shell

was reduced from 100" to 90" in 10 equal steps, and strains and the total moment M were computed at each step. Table 4-3 shows the finite element results for M at each $R_s$ value considered. Very good agreement was obtained between the analytical results and the finite element solution, as can be seen from Table 4-3. The cross-section flattened in the finite element solution approximately one inch.

IV.1.3.5   Double Fold Model

To demonstrate how the torus of the above section can be used to simulate a double fold, this same model was loaded by changing the secondary radius from 100" to 10". Two cases were considered:   (a) torus completely elastic, and (b) torus elasto-plastic with x = 0.008 and $\sigma_y$ = 74 KSI.

The moment-curvature curve for the elastic solution is shown in Fig. 4-14. It reaches a maximum at a secondary radius of 20" and corresponding moment of 302,602 in-k. This type of behavior indicates that some kind of structural instability, such as buckling, has occurred. The final shape of the torus cross-section is shown in Figure 4-15, in whick the secondary radius is about 10". Note that the original semi-circular section has been flattened out considerable, simulating the behavior of a double fold.

In Fig. 4-16 is shown the moment vs. curvature relation computed for the elasto-plastic torus. Note that this curve peaks at a moment of 14,000 of secondary radii of 80" to 40". Thus the instability occurred at a much lower moment and smaller curvature, due to the ability of the torus material to go plastic. The final cross-sectional shape for this problem was similar to that of the elastic problem, Fig. 4-15.

These results show that the axisymmetric finite element model proposed herein is capable of simulating the behavior of a double fold.
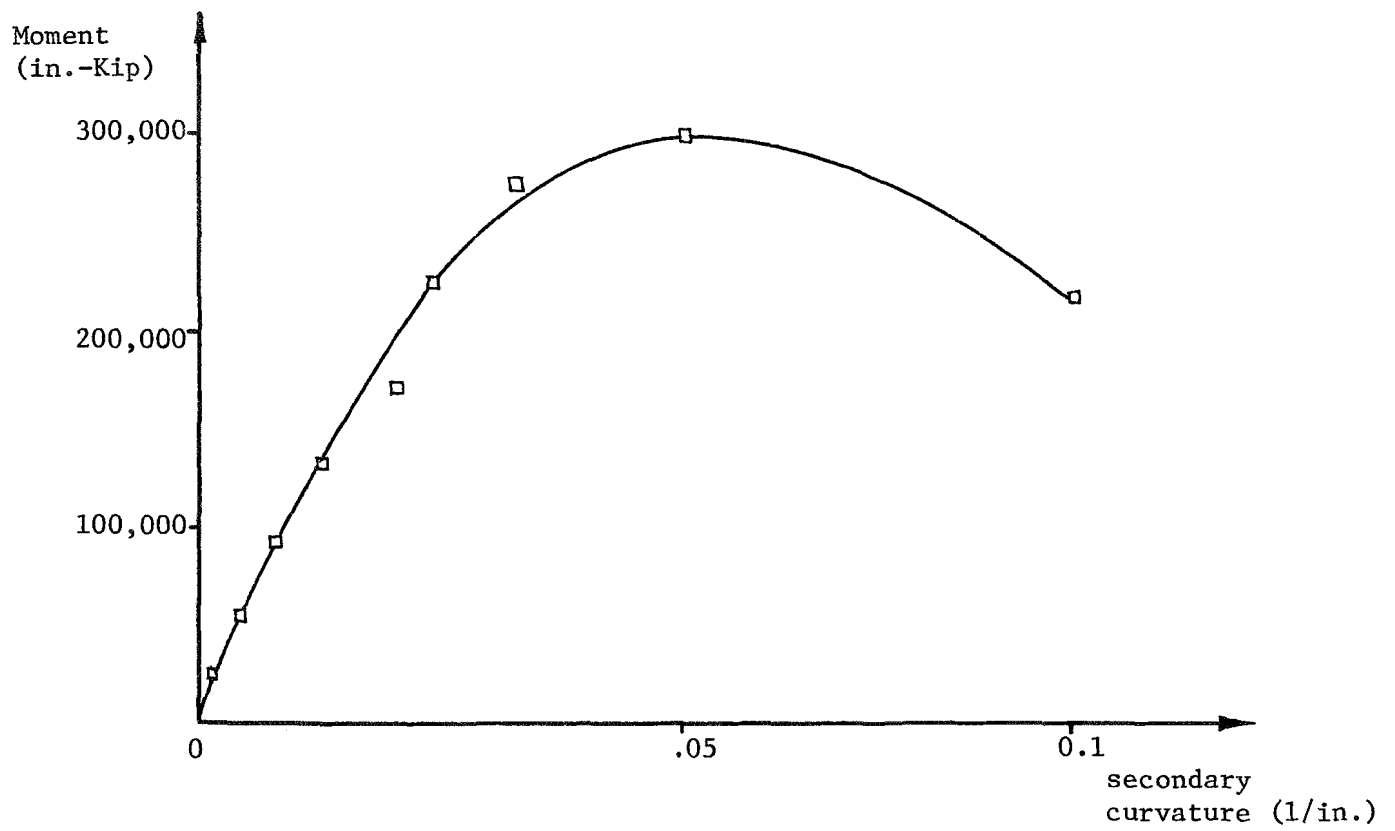
Figure 4-14 —  Moment-Curvature for Elastic Torus
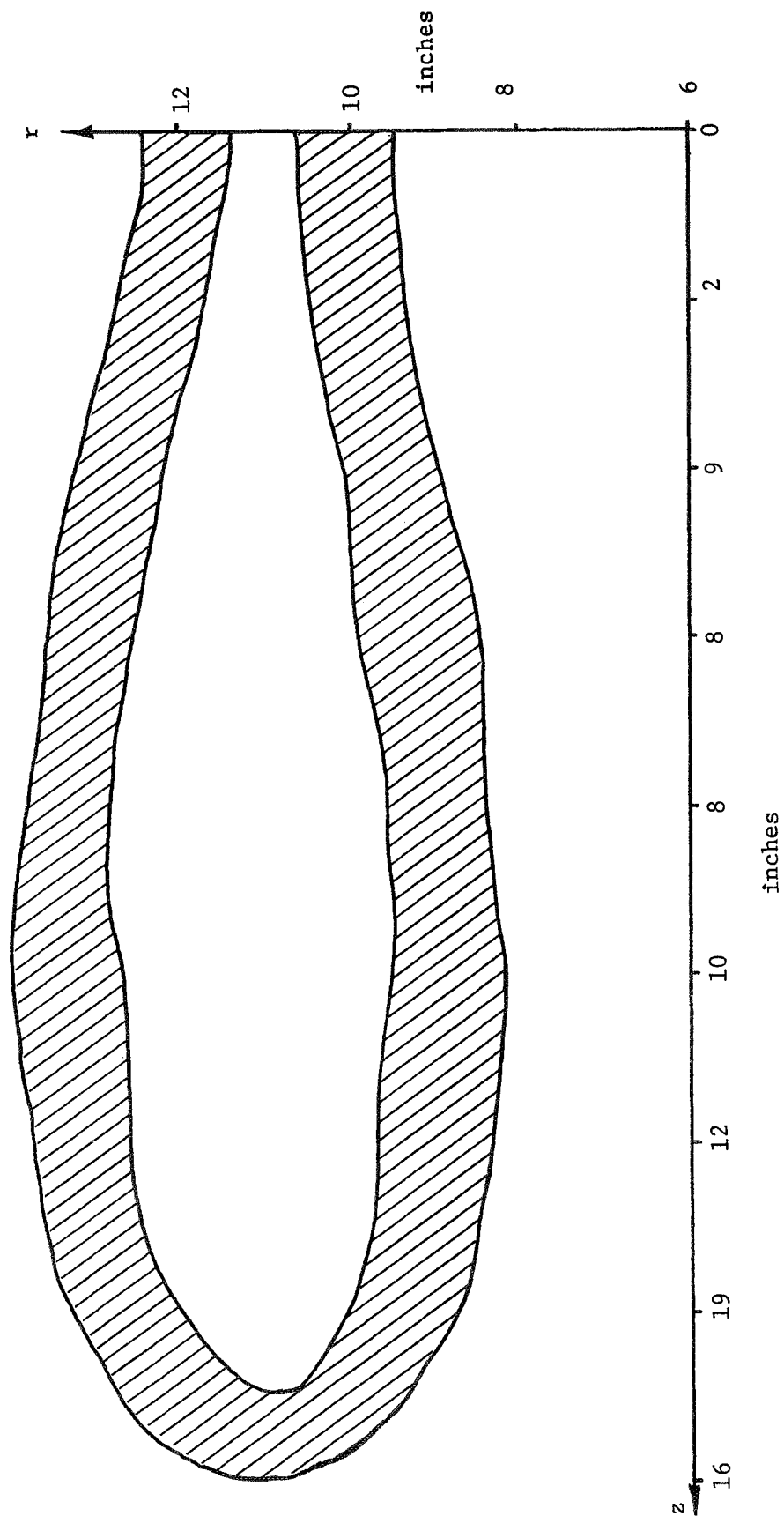
Figure 4-15 - Final Cross-Sectional Shape of Torus
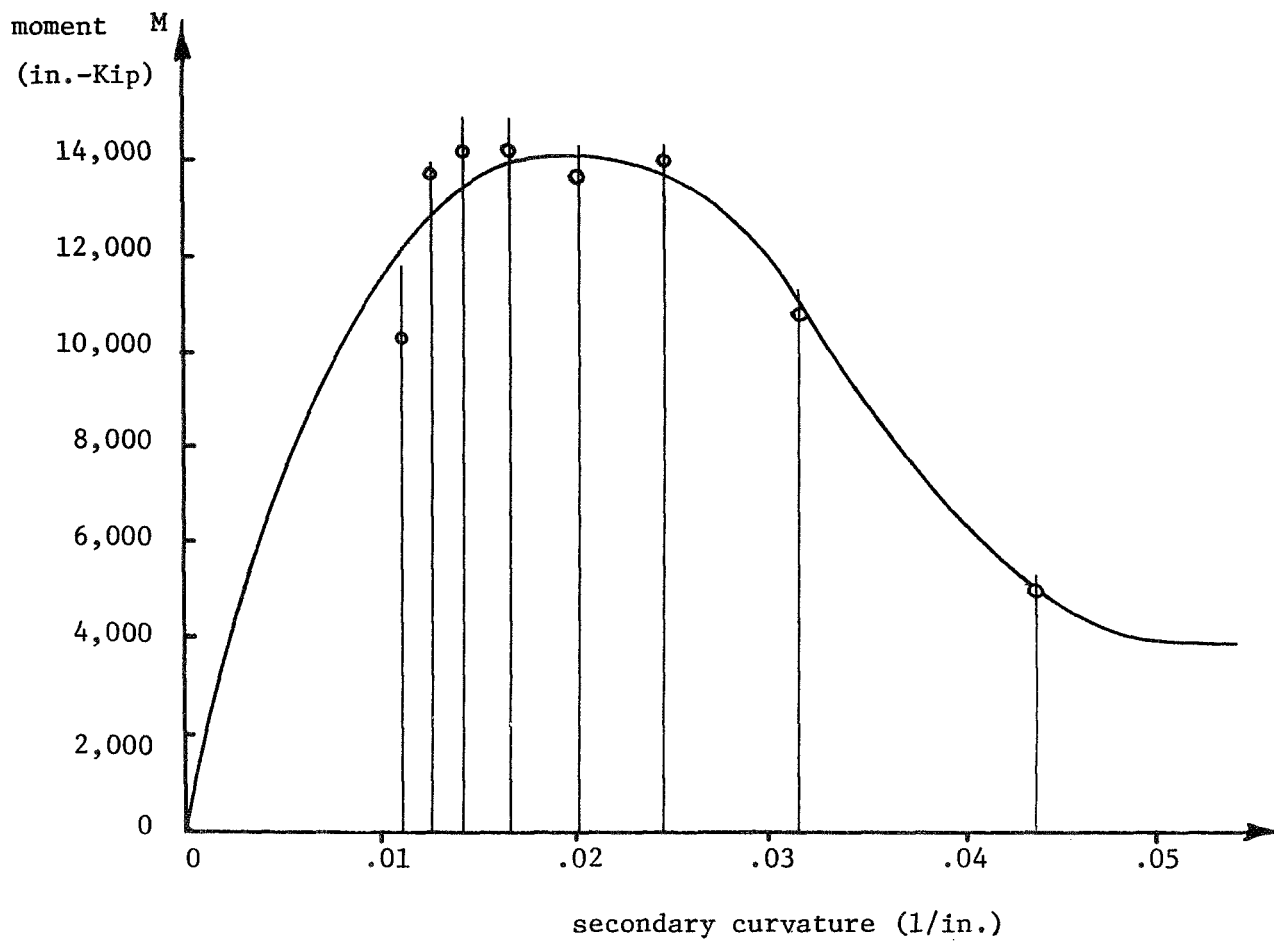
Figure 4-16 – Moment-Curvature for Elasto-Plastic Torus

## IV.1.3.6  Final Double Fold Model

The finite element analysis for stresses and strains in a double fold follows from the torus problem presented above.  For the static double fold analysis, the same information as needed for the single fold must be input by the user.  (See Section III.5.10.4)  In addition, unless otherwise entered, the program will choose the nominal values $R_p$ = 10t, where

$$R_p = \text{Primary Folding Radius}$$

$$R_s = \text{Secondary Folding Radius}$$

$$t = \text{Total Bladder Thickness.}$$

Each layer will consist of axisymmetric finite element arrays as shown in Figure 4-17.  The model will be loaded by incrementally decreasing $R_s$ to a
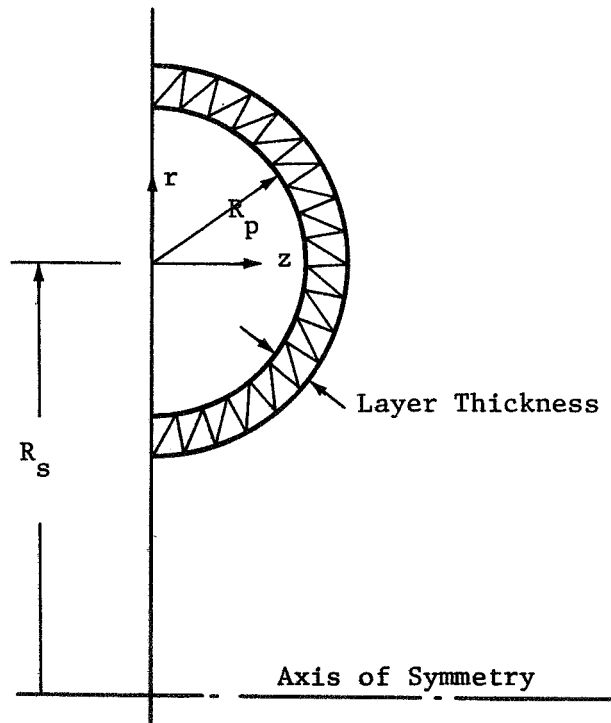


Figure 4-17- Finite Element Layer:  Double Fold

final value of $R_f$, to be input by the user.  At each load increment, the maximum equivalent plastic strain will be computed and used in fatigue life predictions as outlined for the single fold.

IV.2    <u>Double Fold Tests</u>:  Task 3.2

IV.2.1  <u>Casting a Double Fold</u>

Some simple qualitative experiments were performed in order to gain some insight into the nature of the double fold. These experiments consisted of casting a doubly folded sheet of 1/8" thick polyethylene or teflon in epoxy potting resin. After curing, the resulting specimen was cut in order to expose the inside primary radius of the double fold. In some specimens, the doubly folded sheet was coated with a mold release compound. Then the sheet was cut away from the epoxy and the epoxy casting, showing the curvatures inside the double fold, was saved. In all such samples, the inside primary radius was driven down to nearly zero. Photographs of some of the examples are shown below.
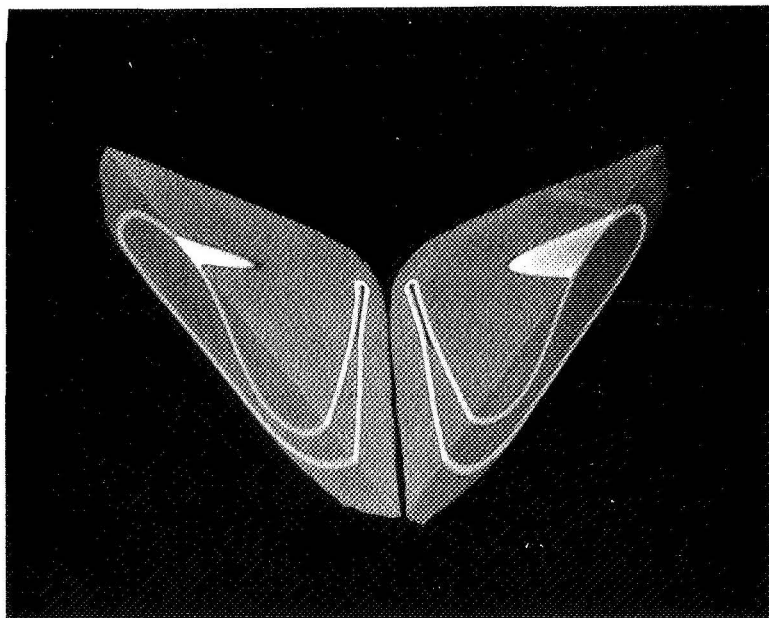


Figure 4-18 - Cast Double fold

Figure 4-18 shows a polyethylene sheet which was etched before casting in order to make the sheet adhere to the epoxy casting resin. The <u>inside</u> (primary) radius was exposed by slicing the casting in the region where the <u>outside</u> (secondary) radius was very small. As can be seen in the photograph, the inside radius is essentially zero.
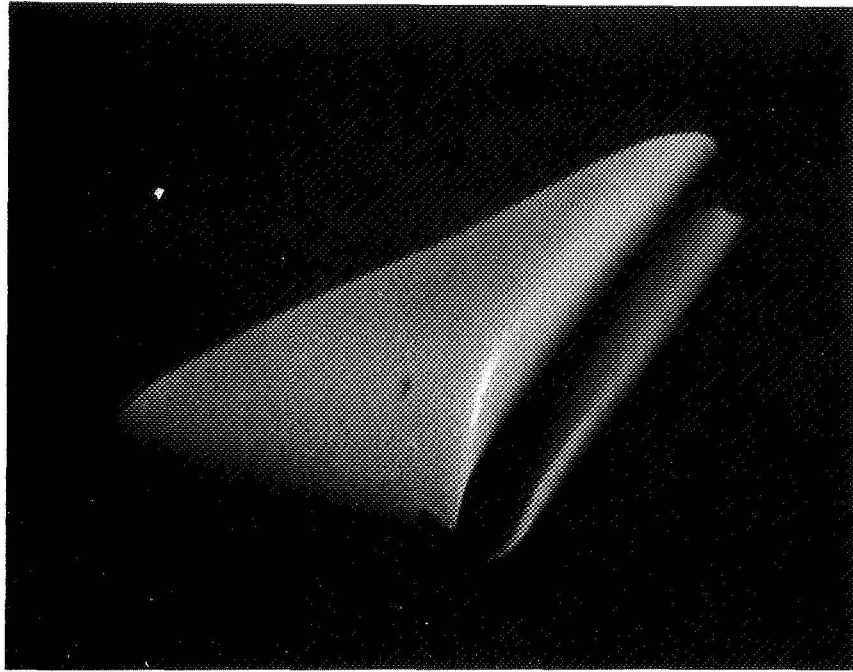
Figure 4-19 -  Casting of Inside of Double Fold

Figure 4-19 shows the solid epoxy casting of the inside portion of the double fold.  A teflon sheet coated with mold release was used to obtain this casting.  The sheet was cut away after the epoxy had cured, revealing the inside radius.  This radius was so small that the casting resin did not flow into this region, as can be seen in Figure 4-19.

## IV.2.2 Double Fold Fatigue Tester

A device for repeatedly folding and unfolding a double fold was designed by Mr. J. P. O'Neill. However, the device was never actually constructed. In this section, some of the details of the double folder are presented, in case future studies indicate a renewed interest in obtaining fatigue life of double folds by test.

The sequence of forming a double fold, if it is to be repeatable at the same torture point on the sheet, is as follows:

a.  Form a single fold and hold the center point of the two edges in a repeatable juxtaposition (or close separation to allow for clamping fixtures);

b.  A blade is extended along the line of the inside of the double fold but should be kept away from the sharp double fold torture point;

c.  Bend the single fold around the blade by means of hinged plates that rotate until parallel with each other and separated by various amounts greater than 4t.

Although the minimum spacing for parallel jaws compressing a double fold is 4t, this compression is probably more severe than that encountered in expulsion systems. Also, it is noted that the strain at a double fold increases rapidly on starting the second fold, and increasing amounts of compression thereafter does not significantly change the maximum strain. Compression to about 8t is expected to be sufficient, as this will allow the blade to remain inside the fold.

The double fold, low cycle fatigue machine requires a structure as shown in Figures 4-20 and 4-21, and requires power for a sequence of operations.

Blade for First Fold

Rotation Center

Connection to Outboard
Bearings About Rotation
Center for First Fold

Folding Plate for
Second Fold
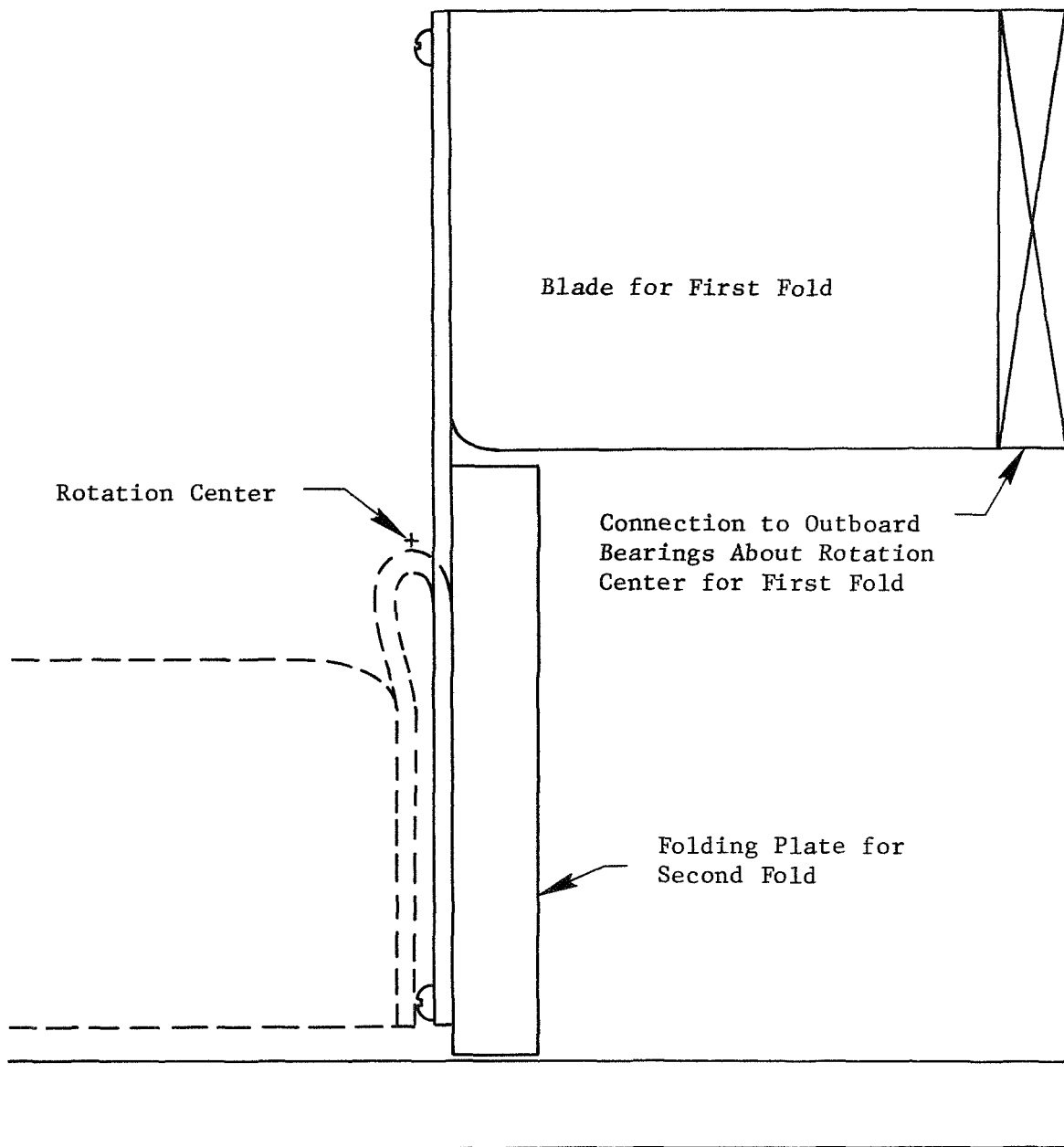
Figure 4-20:   Double Fold Fatigue Machine
(Flat Specimen Position)

Each Plate Folds 90° Towards
the Blade About Center of
Rotation

Blade

Rotation Center for
First Fold

Yoke for
Rotation of Blade
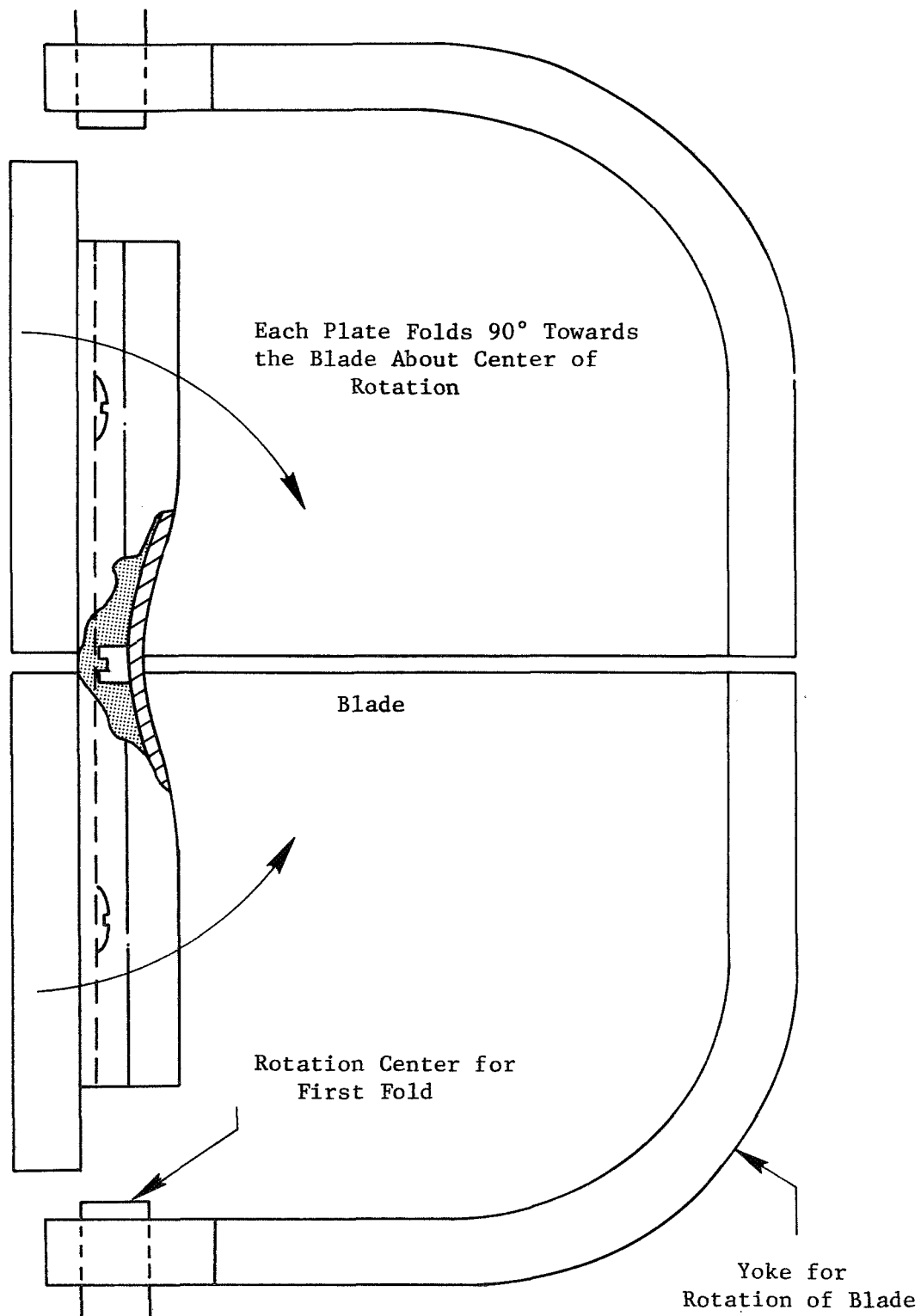
Figure 4-21:   Double Fold Fatigue Machine
(First Fold Position)

## IV.3 TASK 3.3: Compare Theory and Experiments

The simple experiments described in Sections IV.0 and IV.2.2 did point out some weaknesses in the analytical approach to the double fold. The formation of a single fold is characterized by a relatively smooth load-deflection behavior. However, the second fold of the double fold exhibits a buckling behavior as the bending load is increased. Furthermore, this buckling is not axisymmetric in nature, and would not, therefore, be detected by the axisymmetric finite element model. Given sufficient time, the axisymmetric model could be modified by expanding all unknowns in a power series in $\theta$, adding greatly to the complexity and magnitude of the analysis. Since such an analytical effort was beyond the scope of this project, and since the double fold model of Section IV.1.3.5 is capable of simulating very small inner radii accurately, the double fold analysis as presented in Section IV.1.3.5 will be used herein.

IV.4   TASK 3.4:   Traveling Double Fold

The rolling double fold represents the most severe situation analyzed
in this project.   The analysis is quasi-static in nature, that is, the fold
is formed and rolled slowly so that inertia effects need not be included
in the analysis.   The complete double fold is formed first using the
axisymmetric finite element model and reducing the secondary fold radius
to a small value.   The computer program then interrupted and the resulting
information is stored on tape or disk.   The double fold is then "rolled"
by moving one free edge relative to the other, as shown in Fig. 3-27.

The following finite element double fold model was selected to inves-
tigate the feasibility of a rolling double fold analysis.   One layer of
finite elements were arranged as shown in Fig. 4-17, and a total of twenty-
four elements were used.   The model thus had one hundred fifth degrees-of-
freedom.   Other input quantities were:

$$R_p = 0.2"$$

$$R_s = 1.0" \text{ (initially)}$$

$$R_s = 0.1" \text{ (final)}$$

$$t = 0.02"$$

$$E = 200 \text{ KSI}$$

$$E_p = 33 \text{ KSI}$$

$$\sigma_y = 10 \text{ KSI}$$

$$M = 0.9159$$

$$Z = 0.5147 \quad \text{(for fatigue life)}$$

$$\mu = 0.33$$

The model was loaded by changing the secondary radius from 1.0" to 0.117"
(close to the 0.1" desired) in twenty steps.   At this time, the maximum
equivalent plastic strain was 87.39%, giving a fatigue life of only one
cycle!   At this point, a data dump was taken, and this information was
stored on disc.   The program was next restarted, and a total load of 20
KSI was applied to the outer edge, in the negative Z direction, in ten equal

increments. After this "rolling" simulation, the maximum equivalent plastic strain has risen to 93.5%. Thus a considerable increase in straining was achieved by rolling the double fold. The cross-sectional shapes after twenty load steps and thirty steps are shown in Fig. 4-22. This problem consumed slightly over three minutes of CDC 6500 computer time.

The above example demonstrates that the computer program developed during the course of this investigation is capable of modeling rolling double folds. This is a very difficult mathematical problem, due to the following types of nonlinearities: large deflections and strains; plasticity; loading; boundary conditions.
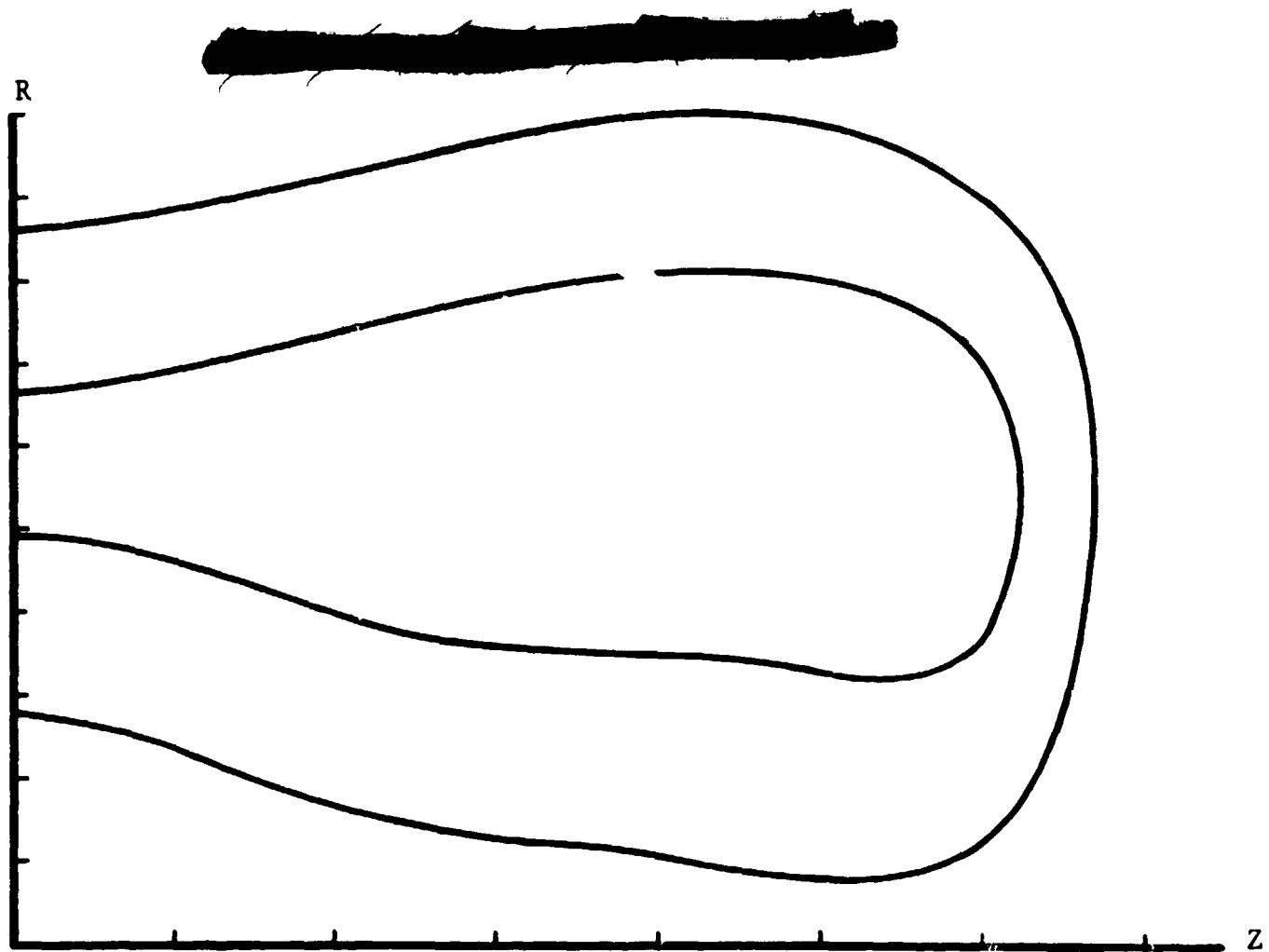
(a) Double Fold After 2C Steps
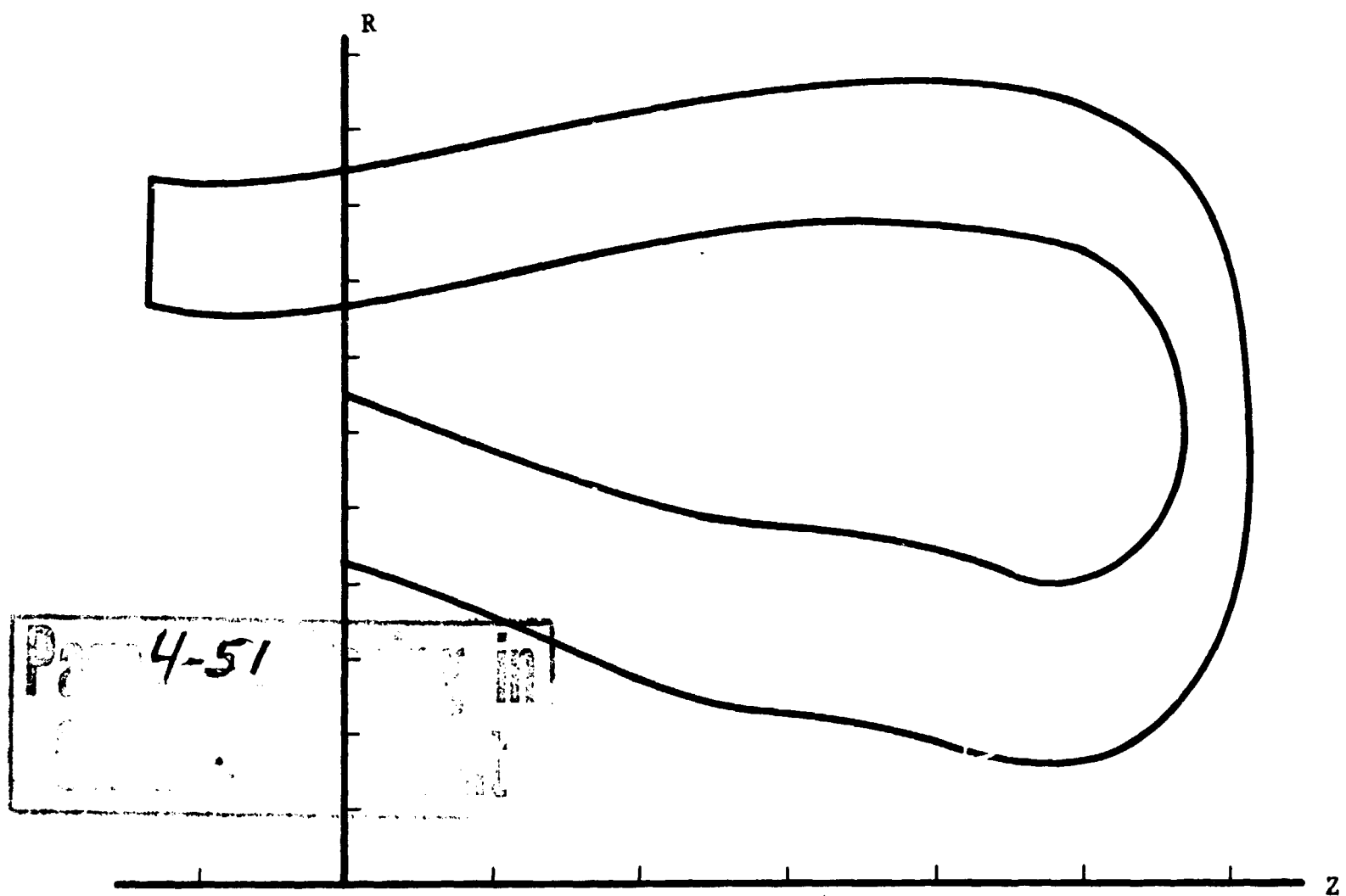


(b) Rolled Double Fold (30 steps)

Figure 4-22: Rolling Double Fold

IV.5    TASK 3.5:    Fatigue Life of Double Folds

A number of different double fold geometries were considered in order to identify that configuration which best simulated the double fold behavior. The desirable behavior is that the largest plastic strains should occur at the region near the center of the fold. However, if the ratio $R_s/t$ was selected as being large (100, e.g.) then the inner and outer sections of the model away from the sharp crease were highest strained, since these surfaces were furthermost from the neutral surface. Also, the flattening pressure, $P_v$ of Fig. 4-1, did not develop due to the large value of $R_s$. Likewise, a small $R_p/t$ ratio (1, e.g.) did not simulate the geometry accurately. The best model developed was one in which $R_s/t = 50$ and $R_p/t = 10$.

In order to illustrate the use of the analysis to predict plastic strains in double folds, two example problems were solved. One model was constructed of teflon, with fatigue properties given in Table 3-5, and for which $E = 7$ KSI, $\mu = 0.35$, $Ep = 0$, and $\sigma y = 2$ KSI. The bladder thickness was taken as $t = 0.02''$, and the model was loaded by changing the secondary radius of curvature/thickness ratio from 50 to 6.1 in twenty steps. At this point, an equivalent plastic strain of only 18.89% had developed, giving a very large fatigue life. The computer analysis consumed 143 seconds.

The second example was an aluminum bladder having the same geometry as the above example, but with $E = 200$ KSI, $\mu = 0.33$, $Ep = 33$ KSI, $\sigma y = 10$ KSI. The fatigue data is given in Table 3-5. Loading changed $R_s/t$ from 50 to 5.9 in 20 steps. The maximum equivalent plastic strain was 87.39%, giving a fatigue life of only one cycle. The run took 142 seconds.

The two examples presented above exhibited widely different behavior, in that one failed in the first cycle (aluminum), whereas the teflon bladder essentially did not fail. Composite bladders could likewise be investigated in order to maximize fatigue life while satisfying other system constraints.

It should be noted herein that the iterative correction does not work efficiently for the double fold analysis. For this reason, small

step sizes should be taken to preserve solution accuracy. In the above examples, twenty equal steps were taken to change the secondary radius from $R_s = 1.0"$ to $R_s = 0.1"$.

## V.0 CONCLUSIONS, RECOMMENDATIONS AND REFERENCES

A computer program has been prepared which will predict plastic folding strains in single and double folds of laminated expulsion bladders. From these strains and uniaxial fatigue data, the expected fatigue life of such bladders can be computed. The strains are calculated using a finite element model (plane strain for single fold and axisymmetric for double fold) which employs a six nodal point triangular element as the basic building block. In addition, a time-share computer program has been coded which performs a simplified strain analysis of single folds. Fatigue information on bladder materials has been compiled for use with the strain analysis. Finally, experiments have been used to verify the predictions of the programs and also to guide the analysis.

Future work to update the finite element code would include the following: allow the sides of the elements to curve as discussed in Section III.5.8.3; include higher order terms in the basic incremental variational principle, Section III.5.2; introduce cos $n\theta$ variation into the axisymmetric finite element model of the double fold, Section IV.1; obtain a more representative constitutive law for large plastic strains; include a Ramsberg-Osgood type stress-strain approximation as well as the bi-linear approximation; include higher order terms in the stress transformation of Section III.5.2; devise an efficient equilibrium check and iteration for the double fold model.

## V.1 References

1.  E. W. Evans, "Effect of Interrupted Loading on Mechanical Properties of Metals," The Engineer (London), Vol. 203, No. 5274, pp. 292-359, and Vol. 203, No. 5275, pp. 325-327 (1957).

2.  J. T. P. Yao and W. H. Munse, "Low-Cycle Fatigue of Metals - Literature Review," Welding Journal Research Supplement, (April, 1962), pp. 182s - 192s.

3.  L. F. Coffin, Jr. and J. F. Tavernelli, "The Cyclic Straining and Fatigue of Metals," Trans. Metallurgical Society of AIME, Vol. 215 (Oct. 1959), pp. 794-807.

4.  D. E. Martin, "An Energy Criterion for Low-Cycle Fatigue," Journal of Basic Engineering, Trans. ASME, Series D, Vol. 83 (Dec. 1961), pp. 565-571.

5.  H. N. Chu, W. Unterberg and J. C. Lee, "Final Report, Improvement of Efficiency and Life of Expulsion Bladders," prepared under Contract NAS 7-506 for NASA Western Operations Office by Rocketdyne (Feb. 1968).

6.  S. S. Manson, Thermal Stress and Low-Cycle Fatigue, McGraw-Hill Book Co., N. Y. (1966).

7.  J. F. Tavernelli and L. F. Coffin, Jr., "Experimental Support for Generalized Equation Predicting Low Cycle Fatigue," J. Basic Eng., Vol. 84, No. 4 (Dec. 1962).

8.  J. F. Tavernelli and L. F. Coffin, Jr., "A Compilation and Interpretation of Cyclic Strain Fatigue Tests on Metals," Trans. ASME, Vol. 51, (1959), pp. 438-453.

9.  T. S. DeSisto and L. C. Carr, "Low Temperature Mechanical Properties of 300 Series Stainless Steel and Titanium," Advances in Cryogenic Engineering, Vol. 6, (1961) Plenum Press, New York, pp. 577-586.

10. S. S. Manson and M. H. Hirschberg, "Fatigue Behavior in Strain Cycling in the Low- and Intermediate- Cycle Range," Proceedings of the 10th Sagamore Army Material Research Conference, Syracuse University Press (Edited by J. J. Burka, N. L. Reed and V. Weiss) (1964), pp. 133-173.

11. E. B. Kula and T. S. DeSisto, "Plastic Behavior of Metals at Cryogenic Temperatures," ASTM STP 387 (1966), pp. 3-31.

12. J. L. Christian and J. F. Watson, "Mechanical Properties of Several 2000 and 6000 Series Aluminum Alloys," Advances in Cryogenic Engineering, Vol. 10, Section A-L, Plenum Press, New York (1965), pp. 63-76.

13. R. W. Smith, M. H. Hirschberg and S. S. Manson, "Fatigue Behavior of Materials Under Strain Cycling in Low and Intermediate Life Range," NASA Tech. Note, D-1574 (April, 1963).

14. "Mechanical Design Data-Teflon," E. I. duPont de Nemours and Co., Wilmington, Delaware, 19898.

15. L. R. G. Treloar, The Physics of Rubber Elasticity, Second Edi., Oxford at the Clarendon Press (1958).

16. R. S. Rivlin and A. G. Thomas, "Rupture of Rubber. I. Characteristic Energy for Tearing," Journal of Polymer Science, Vol. 10 (1953), pp. 291-318.

17. A. G. Thomas, "Rupture of Rubber II. The Strain Concentration at an Incision," Journal of Polymer Science, Vol. 18 (1955), pp. 177-188.

18. H. W. Greensmith and A. G. Thomas, "Rupture of Rubber. III. Determination of Tear Properties," Journal of Polymer Science, Vol. 18 (1955), pp. 189-200.

19. A. G. Thomas, "Rupture of Rubber. V. Cut Growth in Natural Rubber Vulcanizates," Journal of Polymer Science, Vol. 31 (1958), pp. 467-480.

20. H. W. Greensmith, "Rupture of Rubber. X. The Change in Stored Energy on Making a Small Cut in a Test Piece Held in Simple Tension," Journal of Applied Polymer Science, Vol. 7 (1963), pp. 993-1002.

21. A. N. Gent, "Some Chemical Effects in Fatigue Cracking of Vulcanized Rubbers," Journal of Applied Polymer Science, Vol. 6 (1962), pp. 497-502.

22. G. J. Lake and P. B. Lindley, "Role of Ozone in Dynamic Cut Growth of Rubber," Journal of Applied Polymer Science, Vol. 9 (1965), pp. 2031-2045.

23. A. N. Gent, P. B. Lindley and A. G. Thomas, "Cut Growth and Fatigue of Rubbers. I. The Relationship between Cut Growth and Fatigue," Journal of Applied Polymer Science, Vol. 8 (1964), pp. 455-466.

24. G. J. Lake and P. B. Lindley, "Cut Growth and Fatigue of Rubbers. II. Experiments on a Noncrystallizing Rubber," Journal of Applied Polymer Science, Vol. 8 (1964), pp. 707-721.

25. G. J. Lake and P. B. Lindley, "Fatigue of Rubber at Low Strains," Journal of Applied Polymer Science, Vol. 10, (1966), pp. 343-351.

26. G. J. Lake and P. B. Lindley, "Ozone Cracking, Flex Cracking and Fatigue of Rubber. Part One," Rubber Journal, Vol. 146 (1964), pp. 24-30 and p. 79.

27. J. N. Krusos, R. G. Higgins and W. H. Dukes, "Design Criteria and Quality Control Studies for Teflon Expulsion Bladders," Bell Report No. 8460-933012, (Prepared under Contract No. NASw-1317) Bell Aerosystems Company, Buffalo, N.Y. (March 1967).

28. D. W. Chamberlain, B. R. Lloyd and R. L. Tennent, "Determination of the Performance of Plastic Laminates at Cryogenic Temperatures," Technical Documentary Report No. ASD-TDR-62-794, Part II, Narmco Research and Development, San Diego, Calif. (March, 1964).

29. D. W. Chamberlain, "Mechanical Properties Testing of Plastic Laminate Materials Down ot 20K," Advances in Cryogenic Engineering, Vol. 10, (1965), Plenum Press, New York, pp. 117-125.

30. Hill, R., The Mathematical Theory of Plasticity, Oxford Univ. Press, 1956.

31. Timoshenko, S. P., and Woinowsky-Krieger, S., Theory of Plates and Shells, McGraw-Hill, 1959.

32. Timoshenko, S. P., Strength of Materials, 3D Ed.) Vol. 2, D. Van Nostrand Co., Inc., Princeton, N.J., 1956.

33. Turner, M. J., Dill, E. H., Martin, H. C., and Tapp, L. J., "Stiffness and Deflection Analysis of Complex Structures," Journal of Aero Science, Vol. 23, No. 9, September 1956, pp. 805-825.

34. Mallett, R. H., and Marcal, P. V., "Finite Element Analysis of Non-Linear Structures," Journal of the Structures Division, ASCE.

35. Brebbia, C. and Connor, J., Jr., "Analysis of Geometrically Non-linear Plates and Shells by the Finite Element Method," _Dept. of Civil Engrg._, M.I.T., Feb. 1968.

36. Murray, D. W., and Wilson, E. L., "Large Deflection Plate Analysis by Finite Element," _Journal of Structures Div._, ASCE.

37. Mallett, R. H., and Schmit, L. A., "Nonlinear Structural Analysis by Energy Search," _Journal of the Structures Div._, ASCE, Vol. 93, No. ST3, June 1967.

38. Oden, J. T., "Numerical Formulation of Nonlinear Elasticity Problems," _Journal of the Structures Div._, ASCE, Vol. 93, No. ST3, June 1967.

39. Felippa, C. A., "Refined Finite Element Analysis of Linear and Non-linear Two-Dimensional Structures," Ph.D. Thesis, _Univ. of Calif., Berkeley_, Oct. 1966.

40. Argyris, J. H., "Recent Advances in Matrix Methods of Structural Analysis," _Aeronautical Sciences_, Vol. 4, Oxford, London, New York, Paris, 1963.

41. Argyris, J. H., Kelsey, S. and Kamel, H., "Matrix Methods of Structural Analysis," AGARDograph No. 72, Pergammon Press, N.Y., 1964.

42. "Developments in Discrete Element Finite Deflection Structural Analysis by Functional Minimization," AFFDL-TR-68-126, Air Force Flight Dynamics Laboratory, Wright-Patterson Air Force Base, Ohio, September 1968.

43. Schmit, J. A., Jr., Bogner, F. K., and Fox, R. L., "Finite Deflection Structural Analysis Using Plate and Cylindrical Shell Discrete Elements," Proceedings of the AIAA/ASME 8th Structural Dynamics, and Materials Conference, Palm Springs, California, March 1967, pp. 197-211.

44. Wissman, J. W., "Nonlinear Structural Analysis: Tensor Formulation," Proceedings of Conference on Matrix Methods in Structural Mechanics, Wright-Patterson Air Force Base, Ohio, Oct. 1965.

45. Gallagher, R. H., Padlog, J., and Bijlaard, P. P., "Stress Analysis of Heated Complex Shapes," J. Am. Rocket Soc., 32, May 1962, pp. 700-707.

46. Argyris, J. H., "Elasto-Plastic Matrix Displacement Analysis of Three-Dimensional Continua," J. Roy. Aero. Soc., 69, 1965, pp. 633-635.

47. Swedlow, J. L. and Yang, W. H., "Stiffness Analysis of Elastic-Plastic Plates," Graduate Aeronautical Lab., Calif. Inst. of Tech., SM 65-10, 1965.

48. Pope, G., "A Discrete Element Method for Analysis of Plane Elastic-Plastic Stress Problems," R.A.E., T. R. 65028, 1968.

49. Marcal, P. V., and King, J. P., "Elastic-Plastic Analysis of Two-Dimensional Stress Systems by the Finite Element Method," Int. J. Mech. Sci., Vol. 9, 1967, pp. 142-155.

50. Marcal, P. V., "Large Deflection Analysis of Elasto-Plastic Shells of Revolution," Proceedings of the AIAA/ASMC 10th Conference, New Orleans, 1969.

51. Marcal, P. V., "A Comparative Study of Numerical Methods of Elastic-Plastic Analysis," AIAA/ASME, Palm Springs Conference, April, 1967.

52. Armen, H., Pifro, A., and Levine, H. S., "A Finite Element Method for the Plastic Bending Analysis of Structures," Proc. 2nd Conf. on Matrix Methods in Structural Mechanics, Wright-Patterson AFB, Ohio, October 1968.

53. Washizu, K., Variational Methods in Elasticity and Plasticity, Pergamon Press, 1968.

54. Fung, Y. C., Foundations of Solid Mechanics, Prentice-Hall, 1965.

55. Oden, J. T., "Finite Element Applications in Nonlinear Structural Analysis," Conf. on Applications of Finite Element Methods in Civil Engineering, Vanderbilt Univ., Nashville, Tenn., Nov. 13, 14, 1969.

56.  Zudans, Z., "Finite Element Incremental Elastic-Plastic Analysis of Pressure Vessels," Paper No. 69-WA/PVP-1, ASME Winter Annual Mtg. L.A., Cal., Nov. 1969.

57.  Greenbaum, G. A., "Analytical Program for Creep in Axisymmetric Bodies (CRAB)," TRW Systems Report No. STL-517-0049, Oct. 1966.

58.  Reissner, E., "On Finite Bending of Pressurized Tubes," Trans. ASME, Sept. 1959.

Report is to be sent directly to the "Recipients" marked with an (X) under the column headed "Designee" (first section only). In following sections, the report should be sent to the technical librarian of the "Recipient" with a carbon copy of the letter of transmittal to the attention of the person named under the column "Designee". The letter of transmittal should contain the contract number and complete title of the final report.

The distribution list should be included in the final report as an appendix.

## Distribution List for Final Report
### Contract NAS 7-682

| Copies | Recipient | Designee |
|---|---|---|
| 1 | NASA Headquarters<br>Washington, D.C. 20546<br>    Contracting Officer | X |
| 1 | NASA LEWIS RESEARCH CENTER<br>21000 Brookpark Rd.<br>Cleveland, Ohio 44135<br>    Office of Technical Information | X |
| 1 | NASA Manned Spacecraft Center<br>Houston, Texas 77001<br>    Office of Technical Information | X |
| 2 | NASA Marshall Space Flight Center<br>Huntsville, Alabama 35812<br>    Office of Technical Information, MS-IP | X |
| 1 | 	Technical Library | X |
| 1 | 	Dale Burrows   S&E - ASTN - PJ | X |
| 2 | Jet Propulsion Laboratory<br>4800 Oak Grove Dr.<br>Pasadena, California 91103<br>    R. S. Weiner | X |
| 3 | Chief, Liquid Propulsion Technology RPL<br>Office of Advanced Research and Technology<br>NASA Headquarters<br>Washington, D. C., 20546 | X |
| 1 | Director, Technology Utilization Division<br>Office of Technology Utilization<br>NASA Headquarters<br>Washington, D. C. 20546 | X |
| 25 | NASA Scientific and Technical Information Facility<br>P.O. Box 33<br>College Park, Maryland 20740 | X |

| Copies | Recipient | Designee |
|--------|-----------|----------|
| 1 | Director, Launch Vehicles and Propulsion, SV<br>Office of Space Science and Applications<br>NASA Headquarters<br>Washington, D. C. 20546 | X |
| 1 | Director, Advanced Manned Missions, MT<br>Office of Manned Space Flight<br>NASA Headquarters<br>Washington, D. C. 20546 | X |

### NASA Field Centers

| Copies | Recipient | Designee |
|--------|-----------|----------|
| 1 | Ames Research Center<br>Moffett Field, California 94035 | Hans M. Mark |
| 1 | Goddard Space Flight Center<br>Greenbelt, Maryland 20771 | Merland L. Moseson<br>Code 620 |
| 2 | Jet Propulsion Laboratory<br>California Institute of Technology<br>4800 Oak Grove Drive<br>Pasadena, California 91103 | Henry Burlage, Jr.<br>Propulsion Div. 38 |
| 1 | Langley Research Center<br>Langley Station<br>Hampton, Virginia 23365 | Ed Cortwright<br>Director |
| 1 | Lewis Research Center<br>21000 Brookpark Road<br>Cleveland, Ohio 44135 | Director |
| 1 | Marshall Space Flight Center<br>Huntsville, Alabama 35812 | Hans G. Paul<br>Code R-P & VED |
| 2 | Manned Spacecraft Center<br>Houston, Texas 77001 | J. G. Thibodaux, Jr.<br>Chief, Prop. & Power Div. |
| 1 | John F. Kennedy Space Center, NASA<br>Cocoa Beach, Florida 32931 | Dr. Kurt H. Debus |

### Government Installations

| Copies | Recipient | Designee |
|--------|-----------|----------|
| 1 | Aeronautical Systems Division<br>Air Force Systems Command<br>Wright-Patterson Air Force Base<br>Dayton, Ohio 45433 | D. L. Schmidt<br>Code ASRCNC-2 |
| 1 | Air Force Missile Development Center<br>Holloman Air Force Base<br>New Mexico 88330 | Maj. R. E. Bracken |

| Copies | Recipient | Designee |
|---|---|---|
| 1 | Air Force Missile Test Center<br>Patrick Air Force Base, Florida | L. J. Ullian |
| 1 | Space and Missile Systems Organization<br>Air Force Unit Post Office<br>Los Angeles 45, California 90045 | Col. Clark<br>Technical Data Center |
| 1 | Arnold Engineering Development Center<br>Arnold Air Force Station<br>Tullahoma, Tennessee 37388 | Dr. H. K. Doetsch |
| 1 | Bureau of Naval Weapons<br>Department of the Navy<br>Washington, D. C. 20546 | J. Kay<br>RTMS-41 |
| 1 | Defense Documentation Center Headquarters<br>Cameron Station, Building 5<br>5010 Duke Street<br>Alexandria, Virginia 22314<br>ATTN: TISIA | |
| 1 | Headquarters, U. S. Air Force<br>Washington 25, D. C. 20546 | Col. C. K. Stambaugh<br>AFRST |
| 1 | Picatinny Arsenal<br>Dover, New Jersey 07801 | T. Forsten, Chief<br>Liquid Propulsion<br>Laboratory |
| 2 | Air Force Rocket Propulsion Laboratory<br>Research and Technology Divison<br>Air Force Systems Command<br>Edwards, California 93523 | RPRPD/Mr. H. Main |
| 1 | U. S. Army Missile Command<br>Redstone Arsenal<br>Alabama 35809 | Mr. Walter Wharton |
| 1 | U. S. Naval Ordnance Test Station<br>China Lake<br>California 93557 | CODE 4562<br>Chief, Missile Propulsion<br>Div. |

CPIA

| | | |
|---|---|---|
| 1 | Chemical Propulsion Information Agency<br>Applied Physics Laboratory<br>8621 Georgia Avenue<br>Silver Spring, Maryland 20910 | Tom Reedy |

INDUSTRY CONTRACTORS

| Copies | Recipient | Designee |
|---|---|---|
| 1 | Aerojet-General Corporation<br>P. O. Box 296<br>Azusa, California  91703 | W. L. Rogers |
| 1 | Aerojet-General Corporation<br>P. O. Box 1947<br>Technical Library, Bldg. 2015, Dept. 2410<br>Sacramento, California  95809 | R. Stiff |
| 1 | Space Division<br>Aerojet-General Corporation<br>9200 East Flair Dr.<br>El Monte, California | S. Machlawski |
| 1 | Aerospace Corporation<br>2400 East El Segundo Blvd.<br>P. O. Box 95085<br>Los Angeles, California  90045 | John G. Wilder<br>MS-2293 |
| 1 | Atlantic Research Company<br>Edsall Road and Shirley Highway<br>Alexandria, Virginia 22314 | Dr. Ray Friedman |
| 1 | Avco Systems Division<br>Wilmington, Massachusetts | Howard B. Winkler |
| 1 | Beech Aircraft Corporation<br>Boulder Division<br>Box 631<br>Boulder, Colorado | J. H. Rodgers |
| 1 | Bell Aerosystems Company<br>P. O. Box 1<br>Buffalo, New York  14240 | W. M. Smith |
| 1 | Bellcomm<br>955 L'Enfant Plaza, S. W.<br>Washington, D. C. | H. S. London |
| 1 | Bendix Systems Division<br>Bendix Corporation<br>3300 Plymouth Road<br>Ann Arbor, Michigan  48105 | John M. Brueger |
| 1<br>1 | Boeing Company<br>P. O. Box 3707<br>Seattle, Washington 98124 | J. D. Alexander<br>W. W. Kann |
| 1 | Boeing Company<br>1625 K Street, N. W.<br>Washington, D. C.  20006 | Library |

| Copies | Recipient | Designee |
|---|---|---|
| 1 | Missile Division<br>Chrysler Corporation<br>P. O. Box 2628<br>Detroit, Michigan  48231 | Mr. John Gates |
| 1 | Wright Aeronautical Division<br>Curtiss-Wright Corporation<br>Woodridge, New Jersey  07075 | G. Kelley |
| 1 | Research Center<br>Fairchild Hiller Corporation<br>Germantown, Maryland | Ralph Hall |
| 1 | Republic Aviation Corporation<br>Fairchild Hiller Corporation<br>Farmingdale, Long Island, New York | Library |
| 1 | General Dynamics, Convair Division<br>Library & Information Services (128-00)<br>P. O. Box 1128 | Frank Dore |
| 1 | Missile and Space Systems Center<br>General Electric Company<br>Valley Forge Space Technology Center<br>P. O. Box 8555<br>Philadelphia, Pa. | F. Mezger<br>F. E. Schultz |
| 1 | Grumman Aircraft Engineering Corp.<br>Bethpage, Long Island<br>New York  11714 | Joseph Gavin |
| 1 | Honeywell, Inc.<br>Aerospace Division<br>2600 Ridgway Rd.<br>Minneapolis, Minn. | Mr. Gordon Harms |
| 1 | Hughes Aircraft Co.<br>Aerospace Group<br>Centinela and Teale Streets<br>Culver City, Calif.  90230 | F. H. Meter<br>V.P. and Div. Mgr.<br>Research & Dev. Div. |
| 1 | Walter Kidde and Company, Inc.<br>Aerospace Operations<br>567 Main Street<br>Belleville, New Jersey | R. J. Hanville<br>Dir. of Research Engr. |
| 1 | Ling-Temco-Vought Corporation<br>P. O. Box 5907<br>Dallas, Texas  75222 | Warren G. Trent |
| 1 | Arthur D. Little, Inc.<br>20 Acorn Park<br>Cambridge, Massachusetts  02140 | Library |
| 1 | Lockheed Missiles and Space Co.<br>ATTN: Technical Information Center<br>P. O. Box 504<br>Sunnyvale, California  94088 | J. Guill |

| Copies | Recipient | Designee |
|---|---|---|
| 1 | Lockheed Propulsion Company<br>P. O. Box 111<br>Redlands, California 92374 | Library |
| 1 | The Marquardt Corporation<br>16555 Saticoy Street<br>Van Nuys, Calif. 91409 | Library |
| 1 | Baltimore Division<br>Martin Marietta Corporation<br>Baltimore, Maryland 21203 | Mr. John Calathes (3214) |
| 1 | Denver Division<br>Martin Marietta Corporation<br>P. O. Box 179<br>Denver, Colorado 80201 | Dr. Morganthaler<br>A. J. Kullas |
| 1 | Astropower Laboratory<br>McDonnell-Douglas Aircraft Company<br>2121 Paularino<br>Newport Beach, California 92663 | Dr. George Moc<br>Director, Research |
| 1 | McDonnel-Douglas Aircraft Corp.<br>P. O. Box 516<br>Municipal Airport<br>St. Louis, Missouri 63166 | R. A. Herzmark |
| 1 | Missile and Space Systems Division<br>McDonnell-Douglas Aircraft Company<br>3000 Ocean Park Boulevard<br>Santa Monica, Calif. 90406 | Mr. R. W. Hallet<br>Chief Engineer<br>Adv. Space Tech. |
| 1 | Space & Information Systems Division<br>North American Rockwell<br>12214 Lakewood Boulevard<br>Downey, California 90241 | Library |
| 1 | Rocketdyne (Library 586-306)<br>6633 Canoga Ave.<br>Canoga Park, Calif. 91304 | Dr. R. J. Thompson<br>S. F. Iacobellis |
| 1 | Northrop Space Laboratories<br>3401 West Broadway<br>Hawthorne, California 90250 | Dr. William Howard |
| 1 | Aeronutronic Division<br>Philco Corporation<br>Ford Road<br>Newport Beach, California 92663 | D. A. Garrison |
| 1 | Astro-Electronics Division<br>Radio Corporation of America<br>Princeton, New Jersey 08540 | Y. Brill |

| Copies | Recipient | Designee |
|---|---|---|
| 1 | Rocket Research Corporation<br>520 South Portland Street<br>Seattle, Washington  98108 | Foy McCullough, Jr. |
| 1 | Sunstrand Aviation<br>2421 11th Street<br>Rockford, Illinois  61101 | R. W. Reynolds |
| 1 | Stanford Research Institute<br>333 Ravenswood Avenue<br>Menlo Park, California  94025 | Dr. Gerald Marksman |
| 1 | Pressure Systems, Inc.<br>2017 Camfield Avenue<br>Los Angeles, California | D. Estes |
| 1 | Tapco Division<br>TRW Incorporated<br>23555 Euclid Avenue<br>Cleveland, Ohio  44117 | P. T. Angell |
| 1 | Thiokol Chemical Corporation<br>Aerospace Services<br>Elkton Division<br>Bristol, Pennsylvania | Library |
| 1 | Research Laboratories<br>United Aircraft Corp.<br>400 Main St.<br>East Hartford, Conn.  06108 | Erle Martin |
| 1 | Hamilton Standard Division<br>United Aircraft Corp.<br>Windsor Locks, Conn.  06096 | Mr. R. Hatch |
| 1 | United Technology Center<br>587 Methilda Avenue<br>P. O. Box 358<br>Sunnyvale, California  94088 | Dr. David Altman |
| 1 | Florida Research and Development<br>Pratt and Whitney Aircraft<br>United Aircraft Corporation<br>P. O. Box 2691<br>West Palm Beach, Florida  33402 | R. J. Coar |
| 1 | Vickers, Inc.<br>Box 302<br>Troy, Michigan | Library |

| Copies | Recipient | Designee |
|---|---|---|
| 1 | Calmec Manufacturing Corporation<br>5825 District Blvd.<br>Los Angeles, California  90022 | Library |
| 1 | Carleton Controls Corporation<br>East Aurora, New York  14052 | Library |
| 1 | Dilectrix Corporation<br>69 Allen Boulevard<br>Farmingdale, L. I., New York 11735 | J. Petriello |
| 1 | Shambam, Incorporated<br>Fort Wayne, Indiana | Library |
| 1 | M. C. Manufacturing Company<br>P. O. Box 126<br>Lake Orion, Michigan  90501 | Library |
| 1 | Moog Servocontrols, Inc.<br>Proner Airport<br>East Aurora, New York  14052 | Library |
| 1 | National Waterlift Company<br>2200 Palmer Avenue<br>Kalamazoo, Michigan  49001 | Library |
| 1 | Parker Aircraft<br>5827 W. Century Boulevard<br>Los Angeles, California  90009 | Library |
| 1 | Joclin Manufacturing Company<br>Wallingford, Connecticut | Library |
| 1 | Pyronetics, Inc.<br>10025 Shoemaker Avenue<br>Santa Fe Springs, California  90670 | Library |
| 1 | Stratos Western<br>Division of Fairchild-Hiller Corporation<br>1800 Rosecrans Boulevard<br>Manhattan Beach, California | Library |
| 1 | Solar Division of International Harvester Co.<br>2200 Pacific Avenue<br>San Diego, California | Library |